The Dissertation Committee for Alex Joseph Sitzman Certifies that this is the approved version of the following dissertation:

Investigation on Cutting Metals using Induced Currents

Committee:

Michael F. Becker, Supervisor

David L. Bourell, Co-Supervisor

Surya I. Santoso

Ross Baldick

Francis Stefani

INVESTIGATION ON CUTTING METALS USING INDUCED CURRENTS

by

Alex Joseph Sitzman, B.S.E.E.; M.S.E.

Dissertation

Presented to the Faculty of the Graduate School of
The University of Texas at Austin
in Partial Fulfillment
of the Requirements
for the Degree of

Doctor of Philosophy

The University of Texas at Austin
December, 2014

Acknowledgements

I would like to give special thanks to my brother Justin for breaking the family’s TV before I was born and to my dad for not getting another one; without those events, this never would have happened.

More recently, I am indebted to my co-advisors Dr. Bourell and Dr. Becker for their support and guidance over last few years.

Dr. Stefani’s help with experimental methods and writing technique as well as his street-wise advice was critical. Also, I'd like to thank Dr. Santoso and Dr. Baldick for their help with this dissertation.

I thank Michael Pachuilo for bearing with me in our basement-lab home over the past two years.

Finally, I’d like to thank my parents and all my siblings—Darius, Justin, and Eva—for their encouragement over my full nine-year college career.

This work was supported by the National Science Foundation, under grant CMMI-1232458.

Investigation on Cutting Metals using Induced Currents

Alex Joseph Sitzman, PhD

The University of Texas at Austin, 2014

Supervisor: Michael Becker; Co-Supervisor: David Bourell

Abstract: Non-contact magnetic cutting (NCMC) is a recently developed metal-cutting technology that uses pulsed magnetic fields to advance and steer fine cuts in metal sheet. With this process, a coil is used to induce currents in a workpiece that has a starter feature such as a notch or slit. The induced currents are forced to bend tightly around the starter feature, which enhances the current and magnetic field density. Under the right conditions, resistive heating and large $\boldsymbol{J} \times \boldsymbol{B}$ forces cause localized melting and ejection of material. Each cut is only a fraction of a millimeter long; however, the process can be repeated and the coil can be moved to cut arbitrary lengths and shapes. While some promising results have been obtained, the operating space for making controlled cuts appears to be narrow. Furthermore, the process by which cutting occurs is not well understood. The objective of this dissertation is to provide the scientific underpinnings of NCMC by experimentally assessing the conditions for controlled cutting, developing a method for predicting conditions for optimal cutting, and identifying a path to reduce NCMC to practice.

Table of Contents

List of Tables

List of Figures

CHAPTER 1. INTRODUCTION

1.1 Overview

The magnetic saw effect is an instability that is sometimes observed in pulsed magnets, high-current bus bars, and railguns. When a high current must make a sharp bend, a fine cut can form or extend due to the enhancement of the current and magnetic field density at the cut tip. Though this phenomenon has been known since the 1950s [1], relatively little systematic work has been done to understand it. Recently, it has been proposed that the magnetic saw effect could be used as part of a manufacturing process [2, 3]. This dissertation focuses on a technology called non-contact magnetic cutting (NCMC), which combines a digital manufacturing philosophy with the magnetic saw effect. NCMC splits up the cutting process into very small, discrete elements and allows for precise macroscopic control despite the fact that the underlying physics may not be well controlled at finer resolutions. This is similar to some 3D printing technologies, but subtractive rather than additive. Material hardness should not affect the NCMC process, which suggests that it may have a niche in cutting hard but conductive materials such as molybdenum and tungsten.

Figure 1.1 shows the components that make up an NCMC system.

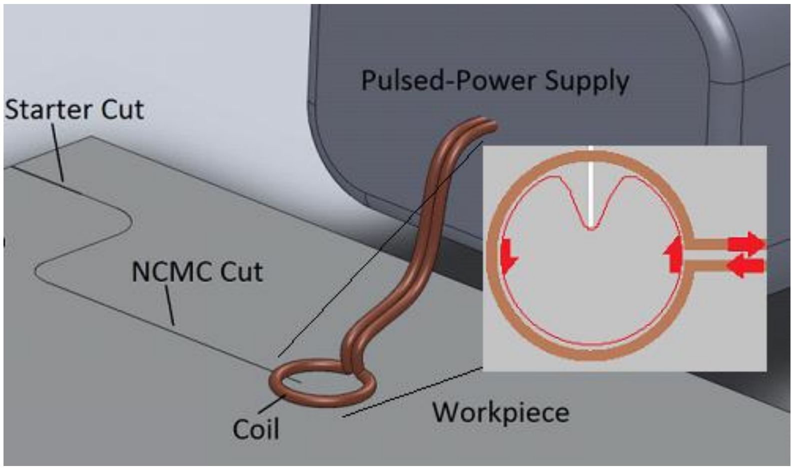

Figure 1.1. Parts of a non-contact magnetic cutting (NCMC) system.

Supporting structures are not shown for clarity in Figure 1.1. The inset portion of Figure 1.1 illustrates how the current in the sample mirrors the coil current except for where it is interrupted by the cut; this interruption forces the current in the sample to make a tight turn at the cut tip, which causes the magnetic saw effect. The operation of the system shown above begins with the coil being placed over some initial cut in the workpiece; this starter cut is needed to create the enhancement point that the NCMC process needs to work. When the pulsed-power supply is triggered, a transient current of about 30 kA-turns flows through the coil, which induces a mirror current in the workpiece. Unlike the coil current, the mirror current is forced to make a sharp bend around the starter cut, as seen in Figure 1.1. At the tip of the starter cut, the current density and magnetic field level are enhanced, and a fine cut extends a fraction of a millimeter. Subsequent pulses continue to extend the cut, and the position of the coil relative to the workpiece can be changed to direct the cut (as shown in Figure 1.2).

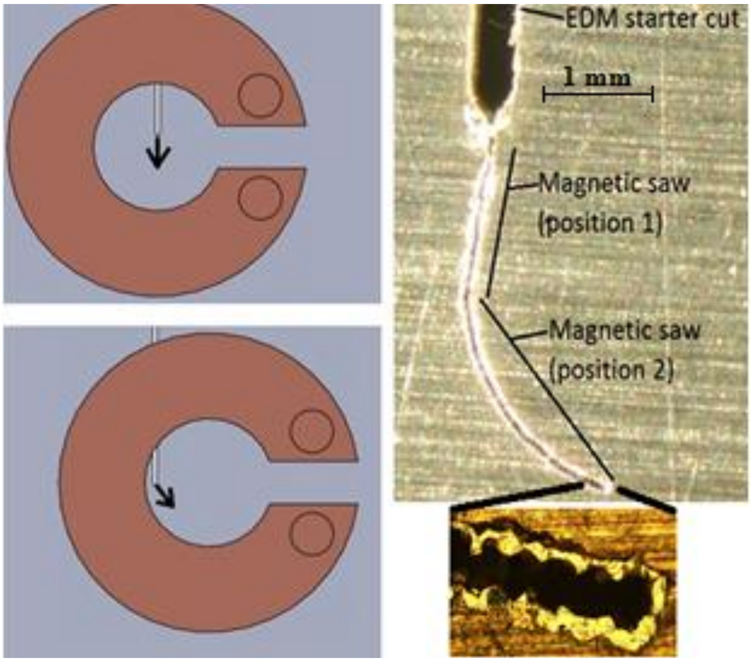

Figure 1.2. The top left figure shows the position used for the first series of pulses, and the bottom left figure shows the position used for the second series of pulses. The electric discharge machine (EDM) starter cut has a kerf of about 0.33 mm; the kerf of the magnetic saw cut is about 0.07 mm.

Whereas Figure 1.2 shows a magnetic cut that is on par with the best observed, Figure 1.3 shows some of the undesirable features that arise when conditions are outside the ideal range for magnetic cutting. Fine cuts, blowholes, bifurcations, liquation cracking, and solidified ejecta have been observed in magnetic saw cuts.

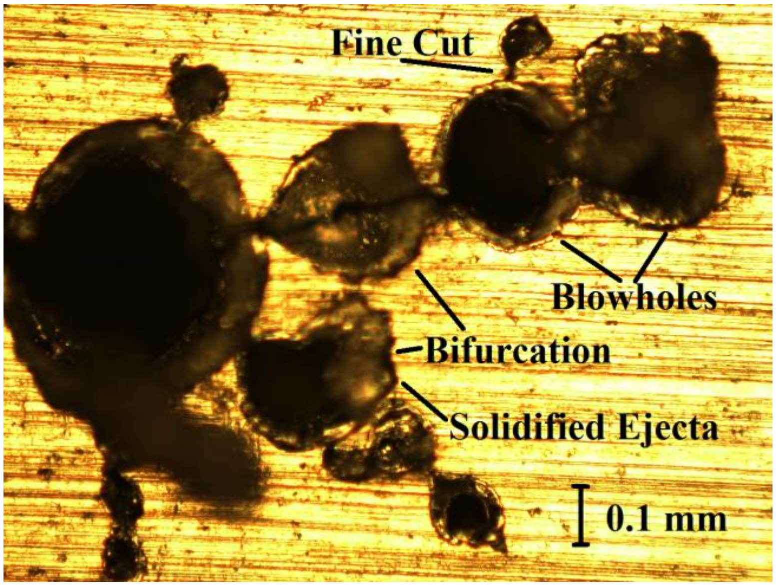

Figure 1.3. Morphology of repeated magnetic saw cuts in 6061 aluminum alloy.

Typical features observed in repeated magnetic saw cutting include a combination of fine cuts, blowholes, bifurcations, and ejecta. Liquation cracking—melting at the boundaries between grains—is also evident on the far right of Figure 1.3. The solidified ejecta that is noted in Figure 1.3 is not in the focal plane; it extends several tenths of a millimeter above the surface of the sample. The shadow coming off the largest blowhole is from a second tower of solidified ejecta. The cuts were made on 0.79 mm thick 6061 aluminum plate at currents that exceeded those known to produce controlled cuts. As seen in Figure 1.3, there appear to be several ways that magnetic saw cuts can extend; however, experiments have shown the relatively round "blowhole" type cuts seen in Figure 1.4 to be the most regular. These cuts generally have a kerf—the width of the cut—of about 0.07 mm, but kerfs as fine as 0.012 have been produced.

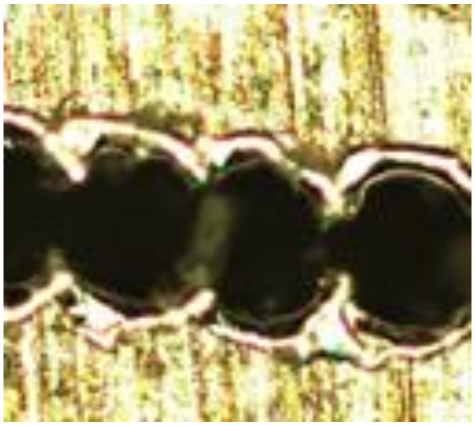

Figure 1.4. This figure shows a close-up of a section of highly regular magnetic saw cuts. The diameter of each cut is about 0.07 mm.

This dissertation will focus on these relatively round holes because they appear to be the most applicable cutting mode for a manufacturing process.

1.2 Scope of Dissertation

This dissertation focuses on understanding the conditions required to cut material with the NCMC process and is intended to provide the foundation for subsequent research toward a viable manufacturing process. There are three primary goals:

1) Experimentally identify the conditions necessary to produce controlled fine cuts in metals using induced currents.

2) Develop a method for predicting the onset of cutting in terms of physics and material science based on data from experiments and simulations.

3) Define additional development needed to realize a manufacturing process.

This dissertation is divided into six chapters. This chapter introduces the NCMC concept and provides a summary of previous, related work. The second chapter details a working theory and development of an analytical model for the onset of cutting. The analytical model is then reformulated as a numerical model to predict cutting distances for arbitrary waveforms. The second chapter concludes with a description of modeling using Maxwell 3D to analyze experiments. The third chapter details the experimental work. This includes experimental setups, experiments using aluminum and copper plate to determine conditions for the onset and propagation of cutting, and additional experiments using printed circuit boards. The fourth chapter contains the results from these experiments, including quantities that had to be obtained indirectly, through simulations. In the fifth chapter, the results of the experiments and simulations are interpreted and explanations for the onset of cutting and for the formation of bifurcations provided. The sixth and final chapter is a summary of the work and conclusions on this project.

1.3 Background

In the years after it was identified, there have only been sporadic publications on the magnetic saw effect. This is probably because it is not a major problem for any application or field of study; generally, if the magnetic saw effect is observed, it is eliminated by engineering solutions such as thickening buswork to reduce peak current density or increasing bend radii to reduce geometric enhancement. It should be noted that all the magnetic saw experiments described in this section used currents that are directly applied to the samples rather than induced by a magnet as in the NCMC process.

1.3.1 FURTH DESCRIBES EFFECT

The magnetic saw effect was first described in the literature by Furth [1] in 1957. Furth proposed that the instability responsible for magnetic sawing is a complex fluid-solid instability, distinct from the more straightforward Kruskal-Schwarzschild instability (the magnetic analog of the Rayleigh-Taylor instability [4]), which he also observed in high-field pulsed magnets.

1.3.2 RAILGUNS

The community that is probably most affected by the magnetic saw effect is the railgun community, due to inherent size constraints for many railgun applications. Railgun conductors, operating at megampere current levels for several milliseconds, can develop magnetic saw cuts due to bends or joints that are not always easily modified [5]. Watt et al. performed a systematic inquiry into damage mechanisms in the primary radius of a railgun armature [6]. As the current level was increased, liquation cracking was observed and, at still higher current levels, magnetic saw cuts were produced. Watt et al. followed up their inquiry of armature damage mechanisms with microscopy on the actual damage [7]. Melting and decohesion at grain boundaries was clearly visible, and the sharpness of the resolidification regions seemed to support the theory that heating was very localized, enhanced by microscopic defects rather than evenly distributed along the radius.

An earlier railgun armature paper also identifies liquation cracking in the major radius as a damage mechanism [5]. While this paper makes no mention of the magnetic saw effect, it shows a photograph that suggests the effect may have been present. Several aluminum alloys were tested and only Al 1100 (commercially pure aluminum) did not show any signs of current-induced damage.

1.3.3 MECHANICAL CRACKS

Many engineering alloys are prone to developing microscopic cracks. Stress enhancements resulting from these cracks can cause premature failure of components due to fatigue or fast fracture. Several papers have been published that study the use of electrical current to mitigate mechanical cracking. It should be noted that these papers use samples with true cracks in them—where material is split apart—as opposed to cuts, where material is removed in the cut region. Material in the crack region may be in contact unless it is being opened by the addition of mechanical force. One paper investigates the use of electrical currents to enhance fracture toughness finds a maximum improvement in fracture toughness of about 14% [8]. Fu et al. blunted cracks in various materials such as carbon steel and some nonferrous metals using pulsed currents [9]. They found that the pulsed currents could be used to significantly increase the radius of the crack tip, thereby lowering the stress concentration. Another group investigated healing cracks in medium carbon steel using pulsed electrical currents [10]. They found some evidence of crack healing, though the work was too preliminary to draw definite conclusions. Liu performed coupled electromechanical simulations, with temperature-dependent material properties, on precracked steel samples that were being mechanically opened [11]. He found that the current distribution around the crack tip creates a circular region of intense heating that can melt and blunt the crack if it is of sufficient magnitude.

Though interesting, this literature is not directly applicable to this project as its goals, approaches, and devices are quite different.

1.3.4 SUPPORTING RESEARCH

Melt-wave erosion is a process that the railgun community has investigated extensively whereby material is melted and removed from a sliding contact. Though this is quite different from the magnetic saw effect described by Furth, the material-removal process and subsequent current commutation are probably similar. Merrill et al. developed a 1D (planar) analytical model of melt-wave erosion and extended the model to include the effect of current commutation out of material that has been removed [12]. They found that the contribution of current commutation did not become significant until magnetic field levels reached about 50–60 T, which is substantially higher than what is present in the NCMC process as it has been used thus far, even considering the enhancement of the magnetic field due to very fine features.

1.3.5 APPLICATIONS

There have been several investigations involving the magnetic saw effect or similar phenomena for possible applications. One such effort studied the use of brittle fracture as an opening switch and found that the addition of current attenuated the speed of brittle fracture from kilometers per second to just a few hundred meters per second [13]. While this opening-switch concept did not directly use the magnetic saw effect, its results suggest that brittle fracture may not contribute to the extension of magnetic saw cuts.

More recently, a group from Washington State presented results that seem to show that a cut could be directed by pulling on samples of lead foil as well as steel plate at various angles [2]. Though the steel-plate experiments mentioned in [2] were performed using laboratory facilities at the University of Texas at Austin (UT), the UT researchers involved abandoned that approach and focused on NCMC. In the steel experiments, the force required to turn the cut only about 22 degrees was nearly enough to break the sample. NCMC seems to hold more promise for manufacturing, because it eliminates the complexity of adding high, rapidly repositionable mechanical forces.

1.3.6 DIRECT MAGNETIC SAW EFFECT RESEARCH

A few researchers have investigated the magnetic saw effect itself, rather than experiencing it in the study of some other phenomenon [14, 15, 16]. In these studies, custom fixtures and samples were built for studying the magnetic saw effect independent of other experiments.

Satapathy et al. used current pulses of tens of kiloamperes to over one hundred kiloamperes and durations of a few milliseconds to produce and extend magnetic saw cuts in 7075 aluminum samples [14]. These samples were notched using an electric discharge machine (EDM) and were a few millimeters thick. Fine cuts, blowholes, and bifurcations were observed as the current levels were increased. The experimental conditions were analyzed with two electromagnetic codes that did not have temperature-dependent material properties. These simulations showed that the material at the cut tip was probably hot enough to melt without the need for additional enhancement from smaller features than the EDM cut radius (such as defects at grain boundaries). Pressures and stresses were also calculated for a specific set of conditions.

Melton et al. performed two experiments that studied the effect of electrical action on damage produced by the magnetic saw effect [15]. These experiments produced what appear to be magnetic saw cuts in aluminum alloy bar measuring 15.9 mm × 44.5 mm in cross section. Damage increased with electrical action, as one would suspect. Only two tests were performed; however, each test had several joints that had enhancement features. Given the limited number of experiments and the fact that the geometric enhancement point was formed by a contact between two different materials, it is difficult to draw conclusions from this paper.

Gallo et al. examined the growth of cuts in Al 6061 and Cu 102 samples that were mechanically loaded while transient currents were applied [16]. A high-speed camera was used to record the time history of the cuts so that the progression of each cut could be compared to current data that were collected simultaneously. An analysis based on linear elastic fracture mechanics and electromagnetics was developed and compared to the results of finite element analysis (FEA) simulations and experiments. The experiments showed a very weak correlation between increased mechanical sample loading and the onset of cutting. The emphasis of the modeling section of the paper is largely on melting at the cut tip due to high current densities, without considering possible fracture effects.

1.4 Summary of Proposed Mechanisms

The body of research on the magnetic saw effect is quite fragmented. Even when combined, it does not show a coherent picture of the magnetic saw effect, but rather a collection of research on damage observed when pulsed currents were forced to bend around slits with fine length scales. For example, Figure 1.5 shows reconstructions of the specimens and pulse shapes used by three of the researchers.

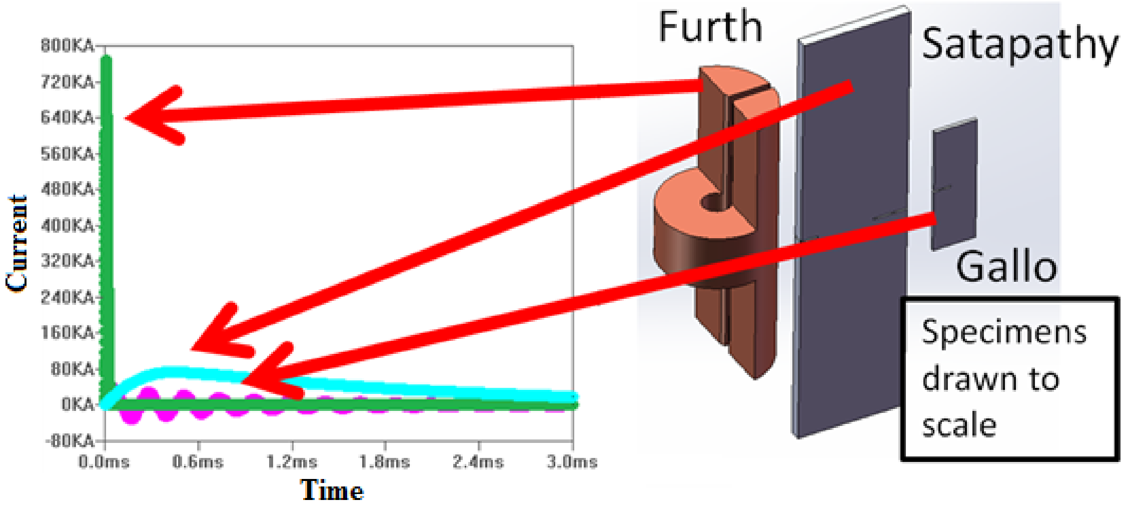

Figure 1.5. This figure shows some of the variation between conditions where the magnetic saw effect has been observed. Note the vast difference in feature sizes and pulse shapes.

The studies seem to be in disagreement on the mechanisms that produce this damage—though, as seen in Figure 1.5, the conditions they employed are sufficiently different that there could be multiple mechanisms. The following section reviews the primary mechanisms that have been proposed in the literature.

Two principal mechanisms have been proposed to explain magnetic cutting: (1) melting, then ejection; and (2) fracture. A third possible mechanism, liquation cracking, is often observed at current levels lower than those known to produce magnetic saw cuts.

1.4.1 Melting and Ejection

As current heats the cut tip, some surface irregularity melts and is ejected before its neighbors. This process of melt and ejection is repeated. Gallo proposes both fracture (see section 1.4.2) and melting as important mechanisms. He approached crack-tip melting from a perspective that is analogous to how stress concentration in cracks is treated in solid mechanics. He reasons that as the cut-tip radius approaches zero, current density increases to infinity; however, there must be a maximum current density beyond which melting occurs. When he exercised his model against his experimental results, he found good agreement when he assumed the maximum current density to be 4.7×10^9 A/m^2. This formulation only considers the instantaneous current density and does not take into account the accumulation of energy in the cut region.

1.4.2 FRACTURE

Satapathy and Gallo each proposed fracture as a contributing factor to extending cuts. Gallo's experiments showed that fracture only mattered when very large external forces were applied to the cracks. He developed a linear elastic model for fracture. However, he focused on the maximum-current-density model described in the previous section. Satapathy's calculations include the effect of $\boldsymbol{J} \times \boldsymbol{B}$ forces. However, he does not document the relative importance of fracture versus melting. Bowden et al., as well as the work discussed in the section on mechanical cracks, suggest that pulsed currents mitigate or attenuate the process of brittle fracture or cracks produced by brittle fracture. The bulk of the literature appears to associate the magnetic saw effect with the opposition of brittle fracture rather than suggesting that brittle fracture is a mechanism of the magnetic saw effect. However, one cannot rule out fracture as a mechanism based on previous work.

1.4.3 LIQUATION CRACKING

Liquation cracking has also been observed before the onset of the magnetic saw effect [5–7]. Though none of the researchers champion liquation cracking as a mechanism, it is associated with the phenomenon, and it is possible that for some materials it plays a major role.

CHAPTER 2. THEORY AND MODELING

This chapter focuses on modeling NCMC. The models described herein fall into one of two categories. The first involves explaining the cutting phenomena. Mechanisms are selected and a model formulated to explain some observed results. The second category of modeling involves using a commercial code to compute quantities that are not directly measureable; this is a form of data reduction. The chapter begins with the development of a melt-only 1D model that can be used to explain the formation of the round holes often observed in NCMC. This model is developed in the context of an experiment performed in 2011 where high-speed images of the cutting process were captured. Subsequent sections describe the simulation approaches taken to analyze various experiments.

2.1 Analytical and Numerical Models for Cutting

Figure 2.1 shows images produced by a high-speed framing camera during a 2011 experiment where the formation of a round blowhole was observed.

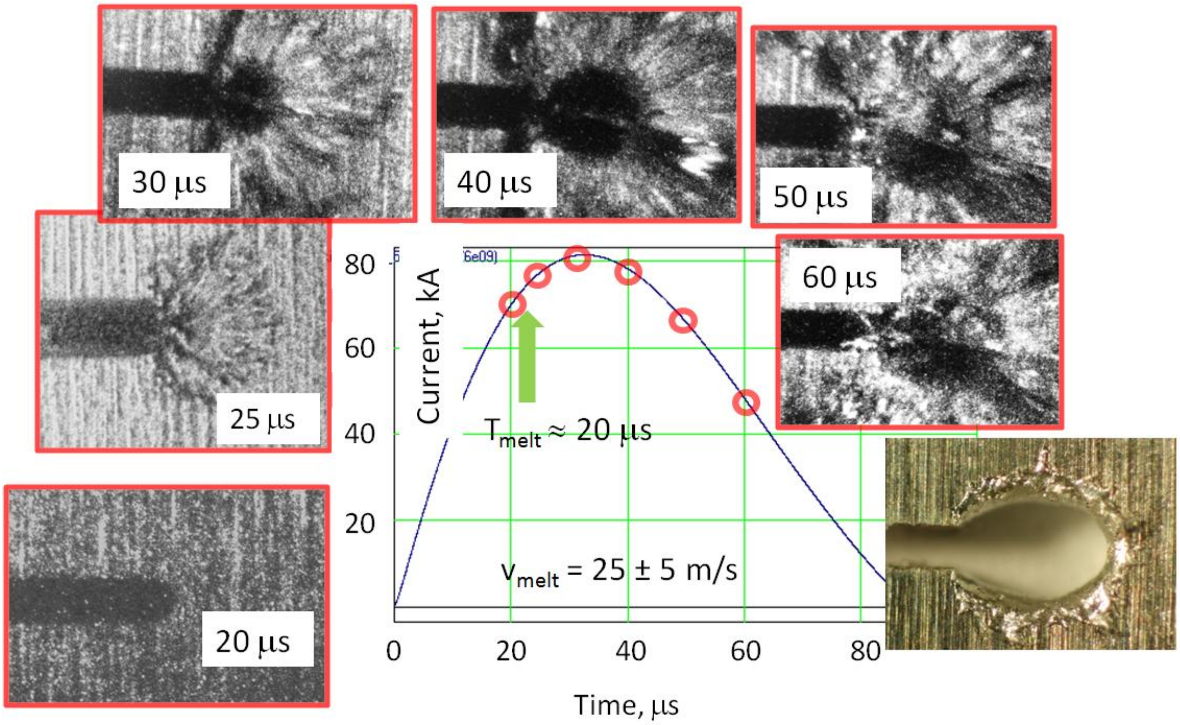

Figure 2.1. This figure shows the result of an experiment conducted in 2011. Comparing the high-speed images, the cutting appears to propagate at about 25 m/s.

Figure 2.1 suggests that melting and subsequent ejection of molten material is the dominant mechanism that produced the cut. The simplest model for the formation of these round holes is a progressive melting model, which assumes material around the cut tip is adiabatically heated to the point of melting and subsequently ejected by magnetic pressure. Calculations show that heat transfer away from the cut through radiation and convection is small compared to the Joule heating that drives the cut. Thermal conduction is not considered in this model, though it can be important—especially at small length scales.

2.1.1 DEVELOPMENT OF THE 1D ANALYTICAL MODEL

The 1D analytical melt-only model is loosely analogous to heating and melting a sequence of fuses in parallel, as shown in Figure 2.2.

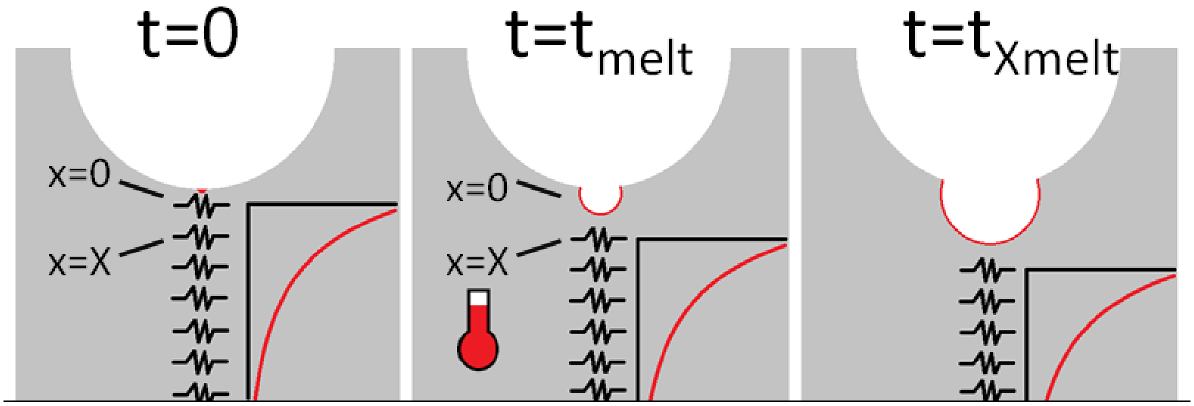

Figure 2.2. This figure illustrates the progressive melting model.

At a point during the current pulse, the first fuse melts; we will call this time t_{melt}. After t_{melt}, current flowing in the first fuse is forced into the remaining fuses. This occurs in part because the resistivity of liquid aluminum is three times higher than that of solid aluminum, but mostly because the magnetic pressure—which is on the order of hundreds of megapascals (tens of kilopounds per square inch)—ejects the molten aluminum. At time $t_{\text{melt}} + \Delta t$, another bit of material is removed and this process repeats.

More complicated models can be formulated—for example, including the effects of commutating the magnetic energy of the ejected material—however, previous work has shown that this effect is not important at the relatively low magnetic fields (less than 20 T) of interest to NCMC [15]. Furthermore an analytical, 1D implementation of progressive melting provides reasonable agreement with the 2011 experiment, as described below.

2.1.2 APPLYING THE 1D MELT-ONLY MODEL TO THE 2011 EXPERIMENT

The 1D melt-only model requires a current distribution as an input. This can be computed for a given geometry and excitation using a commercial electromagnetic code such as Maxwell 3D. Figure 2.3 shows current density plotted along three lines that are 45 degrees apart and begin at the same point on the tip of the starter notch, where the highest current density appears.

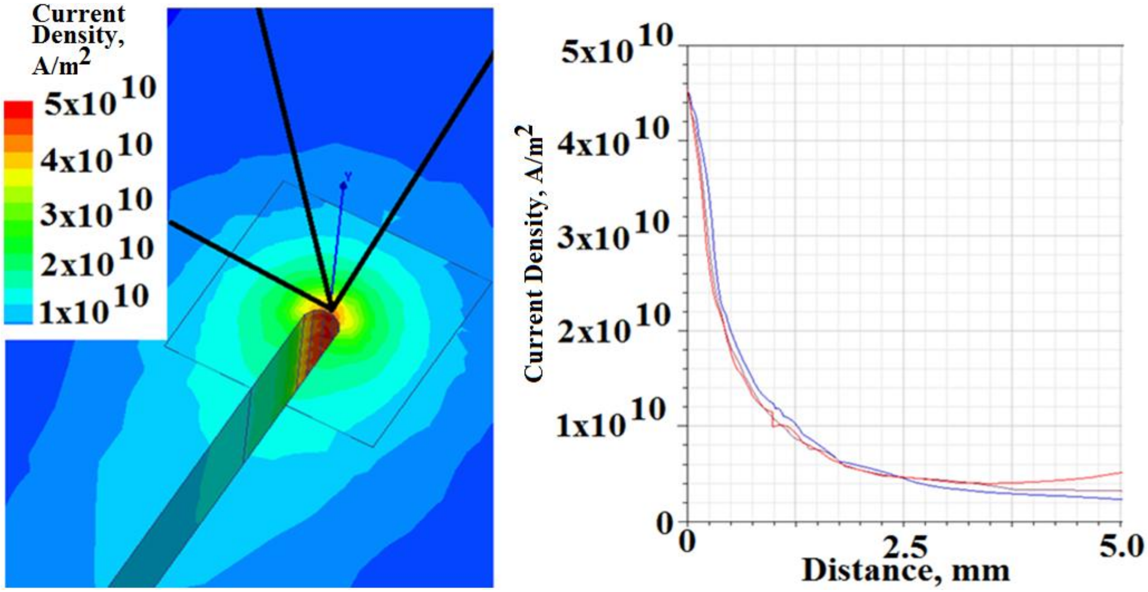

Figure 2.3 On the left, this figure shows the current density plotted on the surface of the sample as well as three lines 45 degrees apart. On the right, the current densities on these lines are plotted for the time step 24 µs into the pulse.

The current densities at most of the time steps throughout the pulse are very similar for the 0, 45, and 90 degree lines. This suggests that the radial symmetry assumption of the 1D model is valid. A similar analysis was performed comparing the current density at the surface and in the center; this analysis showed that the current density in the center is fairly close to that on the surface for samples about 1 mm thick.

It is possible to calculate an approximate speed of propagation for this event, given material properties, initial current distribution, and current pulse. The results for the calculations for a dc case are shown in Figure 2.4 and the derivation is shown in Appendix A.

$\rho_e = resistivity(\Omega * m)$ $\quad E_{melt} = melt\ energy(J/m^3)$

Current density approximated by: $j(x) = j_0 e^{-\alpha x}$

$$Melt\ velocity = \frac{\rho_e * {j_0}^2}{2 * \alpha * E_{melt}}$$

Figure 2.4. This figure shows an analytical expression for melt velocity and defines the variables.

Exercising the expression in Figure 2.4 with values approximating the experiment shown in Figure 2.1 predicts a velocity of about 20 m/s, which is close to the 25 m/s measured in the high-speed images. The values used are shown in Appendix A. This is an older experiment that differs from subsequent ones in that the sample was directly driven by a pulsed-power supply rather than magnetic induction.

The foregoing discussion is presented to propose progressive melting as the most straightforward explanation of what happens in the process of making the round holes:

1) High-speed images show significant melting but no cracking.

2) A simple mathematical model of progressive melting is reasonably accurate in predicting the onset of melt and melt speed seen in high-speed images.

Other effects, such as transient magnetic diffusion and the effect of commutating magnetic energy from ejected aluminum, turn out not to be important. The effect of transient magnetic diffusion is negligible because the samples are so thin that magnetic diffusion occurs more rapidly than current is changing. Figure 2.5 shows that the distribution of current in the thin magnetic saw sample used in the (Figure 1.2) experiments is approximately the same for frequencies between 50 Hz and 5 kHz. Likewise, previous work on melt-wave erosion in railguns has shown that the magnetic energy of the ejected material is not important at the relatively low magnetic fields (less than 20 T) of these experiments [12].

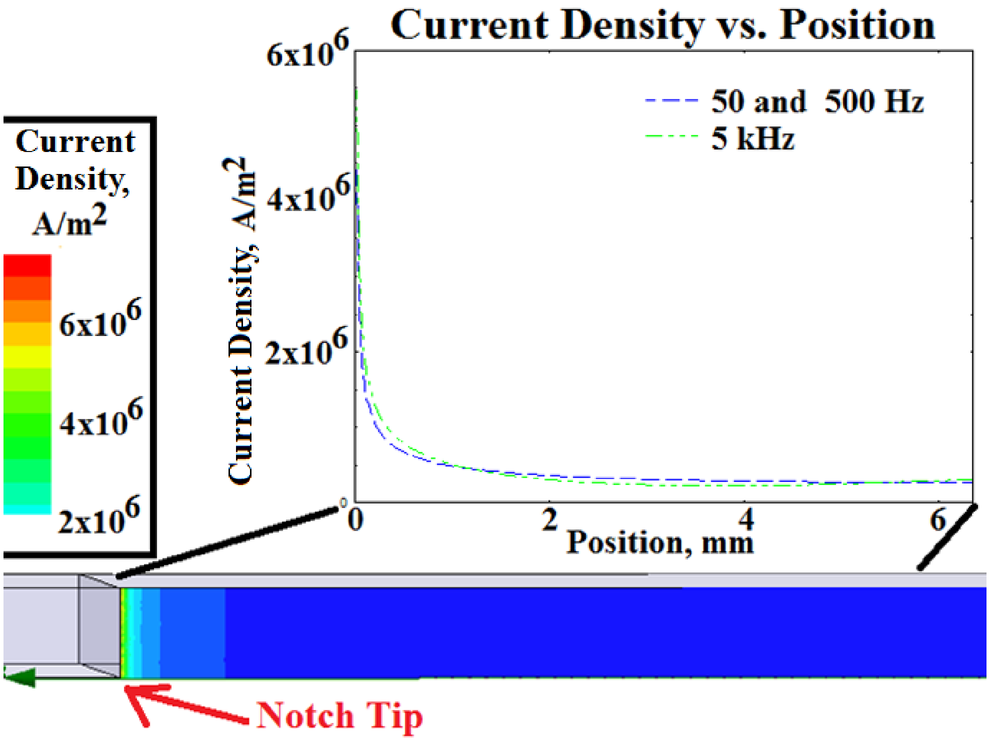

Figure 2.5. A cross section of a 3D model's current density around a notch is shown on the bottom. Above, a graph showing the current density along a line on the top surface of this model at 50 Hz, 500 Hz, and 5 kHz are shown.

A better model would include higher dimensionality and an approximation for temperature-dependent resistivity; however, there would still be a large uncertainty in how much enthalpy is required to remove material, a question that would require significantly more physics to address. The point of the model presented thus far is to show that it is plausible that melting and ejection of material are the dominant mechanisms in the production of blowholes.

2.1.3 1D NUMERICAL MELT-ONLY MODEL

The analytical model described at the beginning of this chapter was extended to a 1D numerical model that uses the current-density outputs from the Maxwell 3D as inputs. The numerical melt-only model is best explained by illustration. Figure 2.6 shows six of the line-current curves, surrounding a plot of the total current through the workpiece.

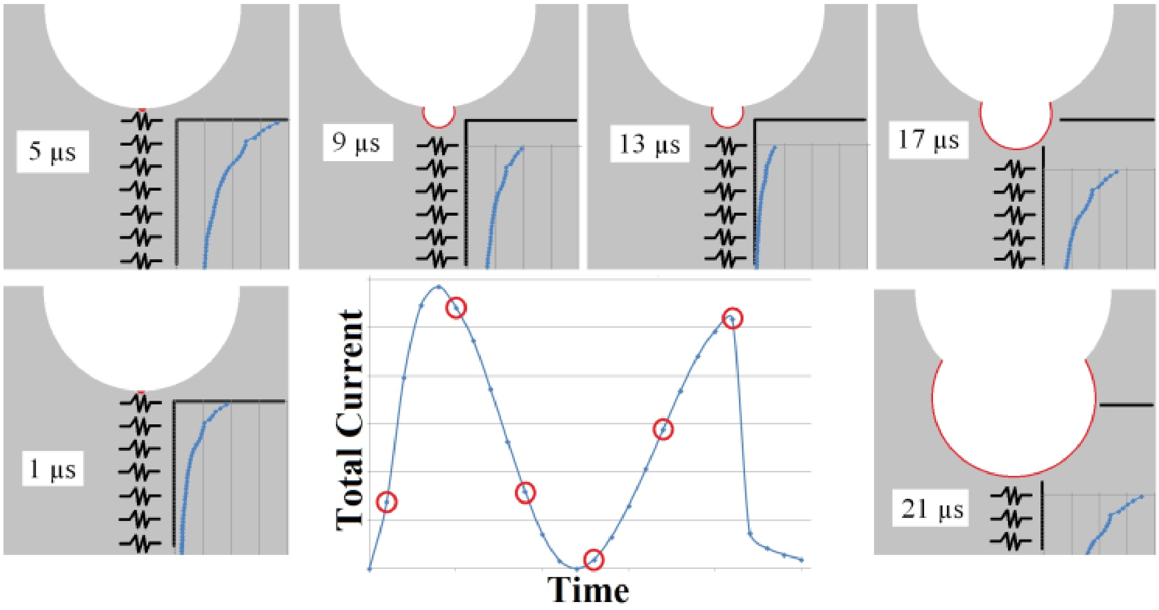

Figure 2.6. The graph in the center shows the total current induced in the printed circuit board (PCB) sample with respect to time as determined by the 3-D FEA code. On the outside, the cut material is modeled as a series of fuses. The current density on a line extending from the 10-µm cube was plotted for each time step; however, only six time steps are shown.

As in the analytical model, the workpiece is approximated by a series of fuses. The current densities computed by FEA code are applied to the fuses, and the thermal energy at each time step is computed. Once a fuse reaches the energy required to melt, any remaining energy beyond the melt energy is applied to the subsequent fuse, and the current is shifted past all melted fuses in the next time step.

This model predicts the cut distances for a given set of conditions. These results can be compared to experiments by photographing the samples, under magnification, before and after a current pulse is applied and calculating the cut distance.

2.1.4 NUMERICAL THERMAL CONDUCTION MODEL

The numerical melt-only model was extended to include thermal effects. This model was used to analyze onset conditions where material was not removed. The results of that analysis are given in Chapter 5. Figure 2.7 shows a simplified solid model and equivalent circuit model for electrical heating and thermal diffusion.

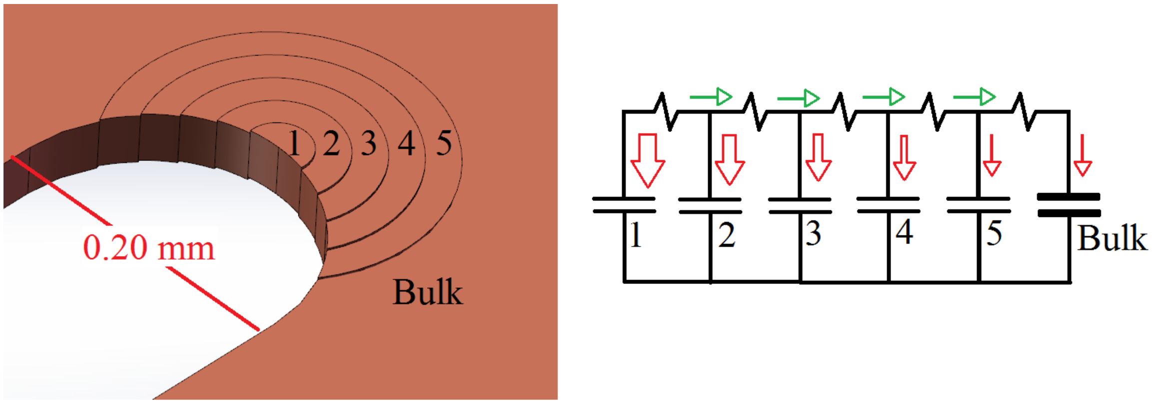

Figure 2.7. A solid model of the 0.20 mm kerf PCB sample and an equivalent circuit model for electrical heating and thermal diffusion. The concentric rings in the solid model have been slightly offset to make them clearer.

The five rings shown on the left side of Figure 2.7 correspond to the five capacitors shown on the right. The red arrows represent the Joule heating produced by the current flowing around the cut tip at a given time. The green arrows represent heat flux flowing from areas of higher temperature to areas of lower temperature. This model was implemented using a finite difference method for cylindrical geometries [17]. The equation implemented is shown in Figure 2.8.

$$\frac{T_{i,j+1}}{\Delta t} = \alpha \frac{r_{i+1/2}\left(\frac{T_{i+1,j+1} - T_{i,j+1}}{\Delta r}\right) - r_{i-1/2}\left(\frac{T_{i+1,j+1} - T_{i+1,j}}{\Delta r}\right)}{r_i \Delta r}$$

Figure 2.8. The finite difference equation used to extend the numerical melt model to include thermal diffusion effects, where *T* is the temperature at a specific node and time step; *j* is the time step, and *i* is a point in the array of nodes. The distance along the radius is given by *r*.

Including thermal conduction added considerable complexity to the code because the time steps must be short enough relative to mesh size to keep the solution from becoming unstable. This is a characteristic of the explicit finite difference method shown in Figure 2.8. Sub-time steps were used to keep the solution stable while allowing the FEA simulations to use typical time steps. Typically, a 1 μs time step was used for the line currents with a 1 ns sub-time step.

2.2 Maxwell 3D Simulations

The short time duration and small scale of the magnetic saw effect makes direct measurement of many important quantities difficult; the length scale of a typical magnetic saw cut is about 0.07 mm, and the pulse duration is about 25 μs. To get around this limitation, the geometry and excitation current are measured and the commercial code Maxwell 3D is used to compute transient quantities of interest such as current density, magnetic flux density, power, energy, and pressure.

It is important to note that there are two main length scales in these simulations: the coil length scale (~2 cm) and the cut length scale (~0.1 mm). Figure 2.9 shows both of these length scales.

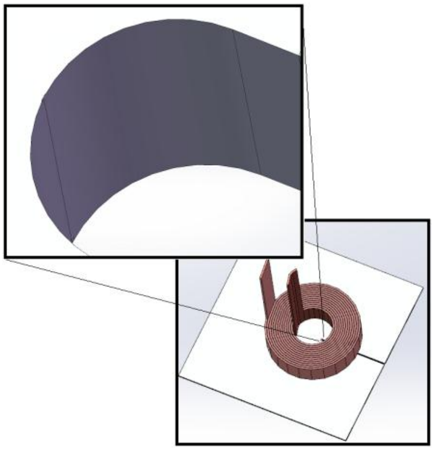

Figure 2.9. The coil's outer diameter is about 2 cm, whereas the cut tip's kerf is about 0.3 mm.

The different length scales shown in Figure 2.9 require special attention to the simulations' meshes to obtain accurate results within reasonable computation times.

2.2.1 CENTERLINE SIMULATIONS

Early experiments showed that under some conditions highly regular cuts could be produced. However, the conditions for this cutting were not understood, nor were the ways in which changes in the experiment would impact cutting. The position of the cut within the coil, the sample thickness, and the pulse duration all impacted the presence or size of the cut. Sixty-three simulations were run in attempt to map out how the heating and pressure at the cut tip change as these parameters are varied. These simulations only considered aluminum samples and geometries where the cut was positioned in the coil's centerline. The centerline simulations all use the same sample geometry, which is detailed in Figure 2.10 and Table 2.1.

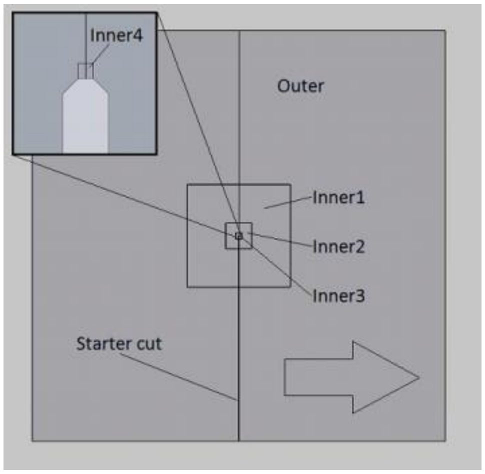

Figure 2.10. This is the geometry of the sample used in the centerline simulations.

Table 2.1. The dimensions of the elements seen in Figure 2.10.

	X (mm)	Y (mm)
Outer	25.4	50.5
Inner1	6.35	12.7
Inner2	1.59	3.18
Inner3	0.381	0.762
Inner4	.0127	.0254

A solid model of the standard sample with the coil that was used to apply the magnetic field is shown in Figure 2.11.

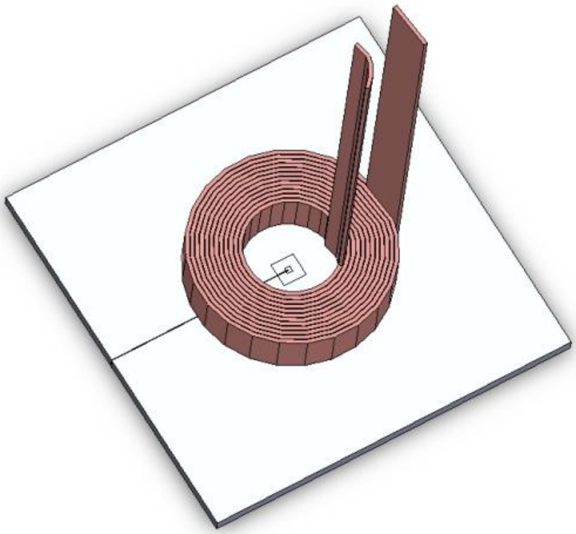

Figure 2.11. The simulated coil is shown with the standard sample in the centered positions. The coil has fourteen turns, an outer diameter of 25.4 mm, an inner diameter of 12.2 inches, and a height of 6.4 mm.

The three current waveforms used in the simulations are shown in Figure 2.12.

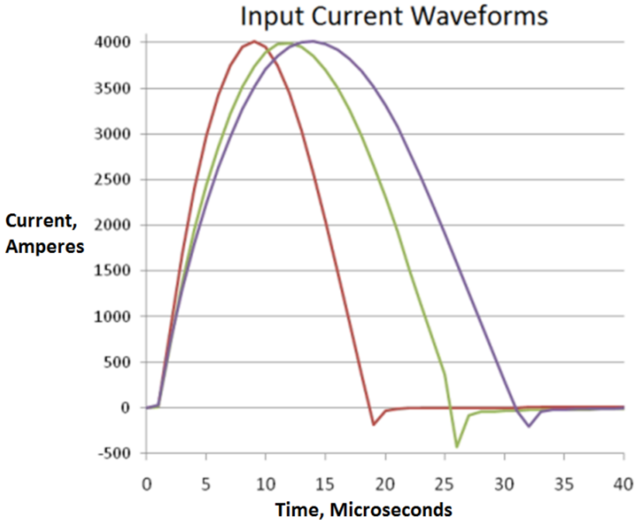

Figure 2.12. This figure shows the three waveforms used in the simulations. The waveforms are experimental data that were normalized to a peak current of 4 kA.

Each of the three pulse widths corresponds to a distinct configuration of the experimental power supply. The currents were normalized to 4 kA so as to hold the peak current constant. The heating and pressure on the element Inner4 were computed for each simulation. The outputs of these simulations are compared in the results section.

2.2.2 ONSET KEYSTONE SIMULATIONS

The onset keystone simulations were intended to provide a more detailed view of the heating and pressure at the cut tip for specific cases, as opposed to the high-level view of the centerline simulations. Figure 2.13 shows an example of the geometry used in this simulation series.

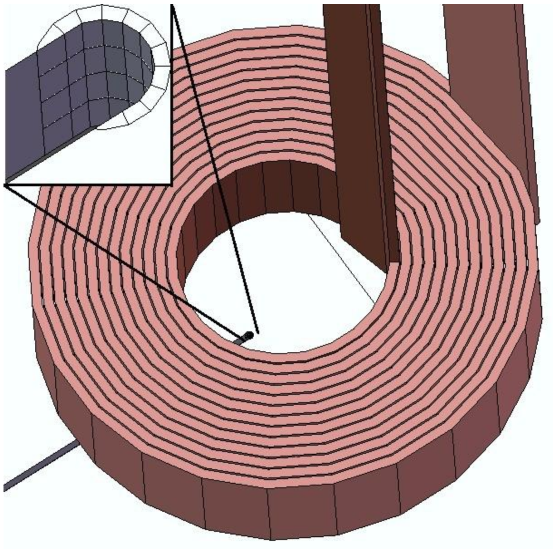

Figure 2.13. The cut tip has been divided into discrete elements to facilitate calculations of the energy accumulating in various locations on the cut tip during the pulse.

The approach shown in Figure 2.13 was used to compare the heating and pressure down the thickness of the sample, as well as radially along the cut tip, in the case of the threshold conditions. This was done for both the EDM cut feature size (0.33 mm kerf) and the feature size of steady-state magnetic saw cutting produced experimentally (0.091 mm kerf). Figure 2.14 compares the cut-tip geometries for these cases.

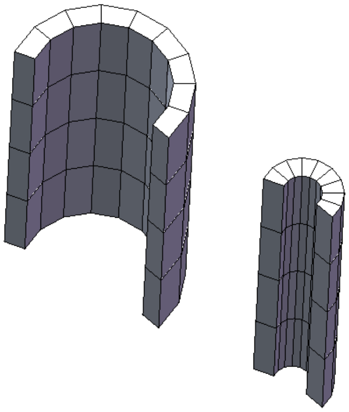

Figure 2.14. The solid models of the cut tip for the EDM and steady-state magnetic saw cutting cases are compared.

2.2.3 ONSET WITH CENTER-ELEMENT AND LINE-CURRENT SIMULATIONS

This set of simulations was used to determine the onset conditions as well as provide the input current densities to a numerical melt model. Figure 2.15 shows the geometry used in one of these simulations.

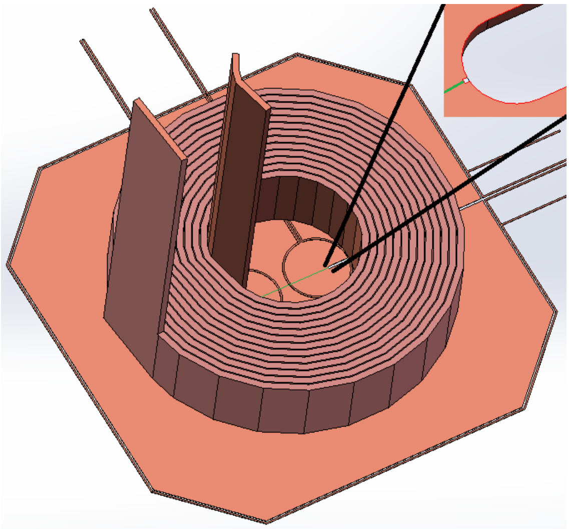

Figure 2.15. The coil and sample geometry with (inset) the small element used for analyzing the onset of cutting and the line used to compute current densities.

A small element where the peak heating occurs was used to analyze the Joule heating and pressure at the onset of cutting. The current density on a line extending from this element was saved at each timestamp. These sets of current densities along a line were used as inputs to a model that extends the analytical model presented previously to a numerical model capable of computing the melt distance for arbitrary input waveforms. For analyzing the plate experiments, identical elements and lines were positioned on the coil-side and non-coil-side surfaces. When printed circuit board (PCB) samples were analyzed, only a single element was used because the conductor was very thin. This center-element and line-current approach was used to analyze the majority of the experiments; these results are presented in Chapter 4.

2.2.4 EJECTA SIMULATION

In experiments, the presence of solidified ejecta near the cut tip appears to alter the cut direction. A simulation was run to determine whether the presence of ejecta alters the point of peak current density. Figure 2.16 shows the result of this simulation.

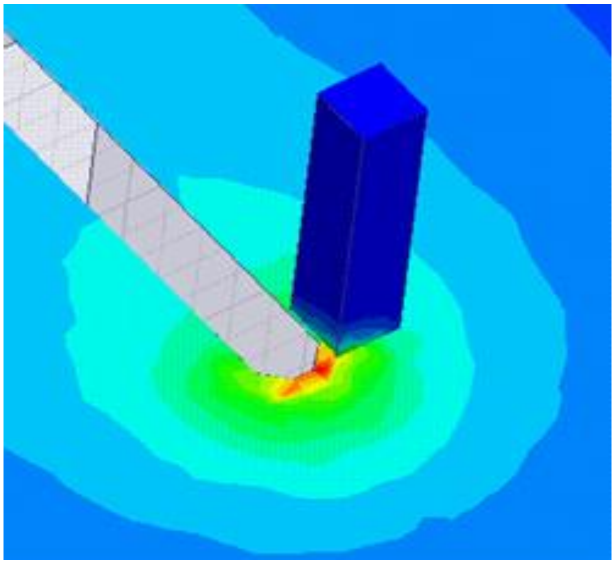

Figure 2.16. The peak current density on the surface of an NCMC simulation of the type described in section 2.2.1, but with the addition of a column of aluminum that represents solidified ejecta.

The column of aluminum appeared to cause the point of highest current density to be biased toward the column. Because of the variability in the solidified ejecta, no systematic simulations or experiments were performed after this result was obtained.

CHAPTER 3. EXPERIMENTS

3.1 First-Generation System Overview

Two apparatuses were constructed for magnetic saw experiments, one in 2011 and the other in 2012–2013. The first-generation system was intended to directly drive magnetic saw experiments with output currents of 30–100 kA. A solid model of this system is shown in Figure 3.1.

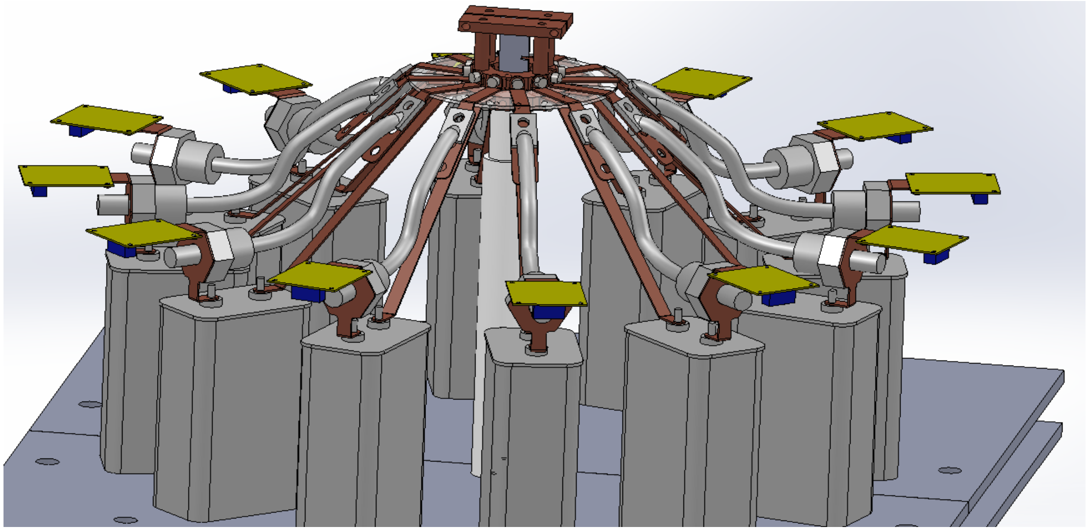

Figure 3.1. A solid model of the first-generation apparatus used to study magnetic sawing. A mounted sample can be seen in the top center.

The first-generation system consisted of a parallel array of capacitor-switch modules connected to a single output section. The system was configured to have a low equivalent inductance so that samples could be tested with high *di/dt*. As shown in Figure 3.1, the sample is mounted above the capacitor modules so that it can be easily seen from all sides. This apparatus was used for a series of imaging experiments and then modified for the NCMC experiments. Figure 3.2 shows a schematic of the original configuration.

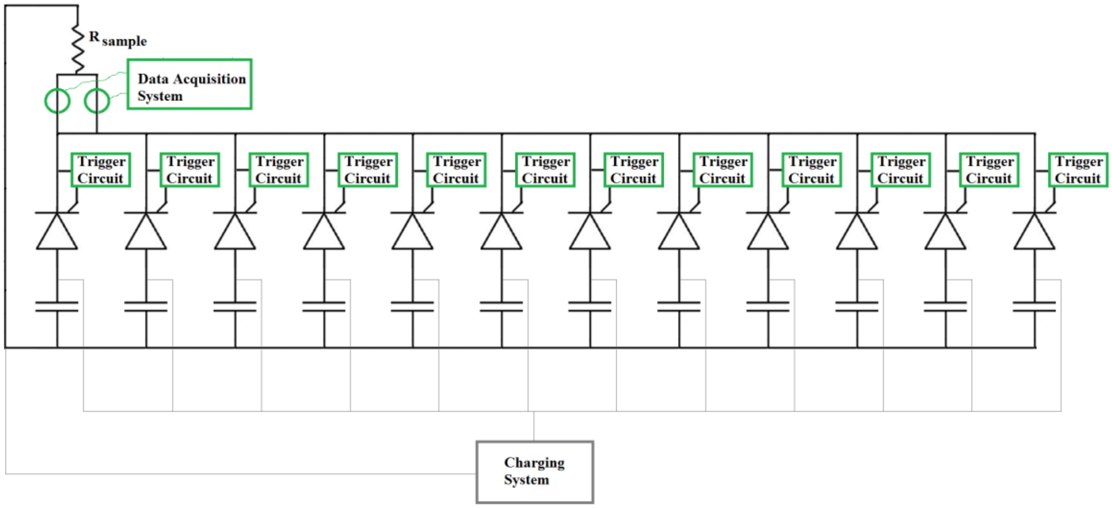

Figure 3.2. Simplified schematic of the original configuration of the first-generation apparatus.

The device was designed to use several different model capacitors; however, only 1 mF, 2 kV pulse-discharge capacitors were ever used for experiments. The charge voltage was limited to 1.6 kV by the thyristor switches. Typically, it was operated between 300 V and 600 V. Output currents were measured through two Rogowski coils, which were recorded on a National Instruments 12-bit digitizer. A sample output current for a 300 V charge is shown in Figure 3.3.

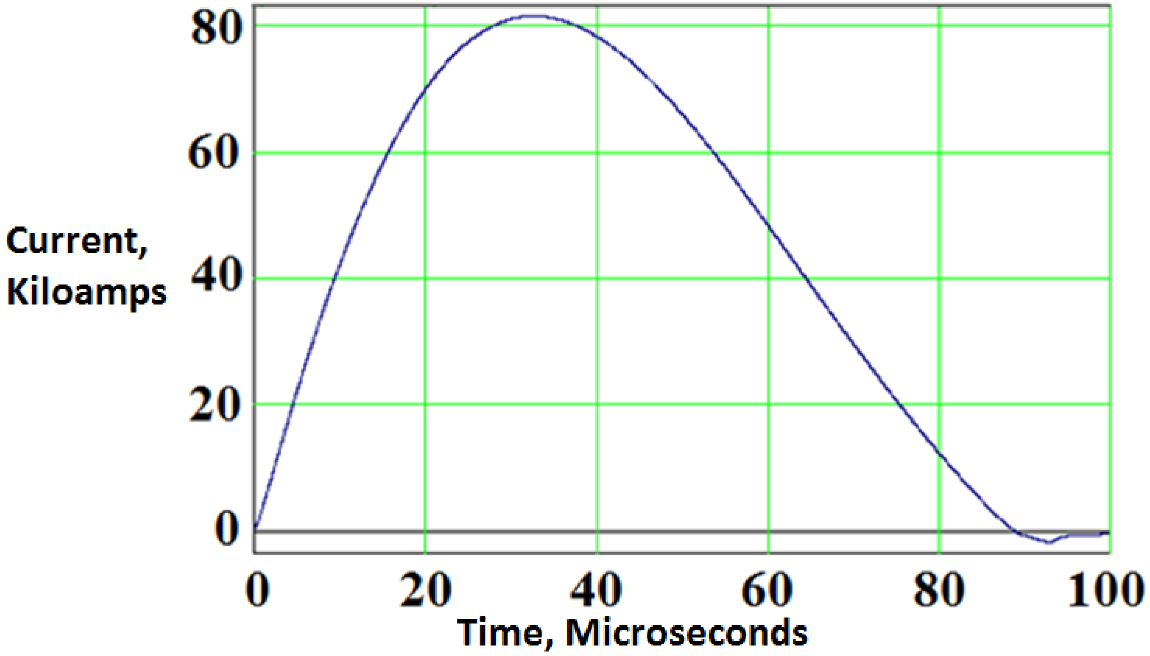

Figure 3.3. The measured current output from a 300 V experiment using the first-generation direct-drive system.

3.2 Inductive-Output Modification to the First-Generation System

The system described above was modified so that it would drive a two-turn coil that was magnetically coupled to a sample. Figure 3.4 shows a photograph of the system after this addition.

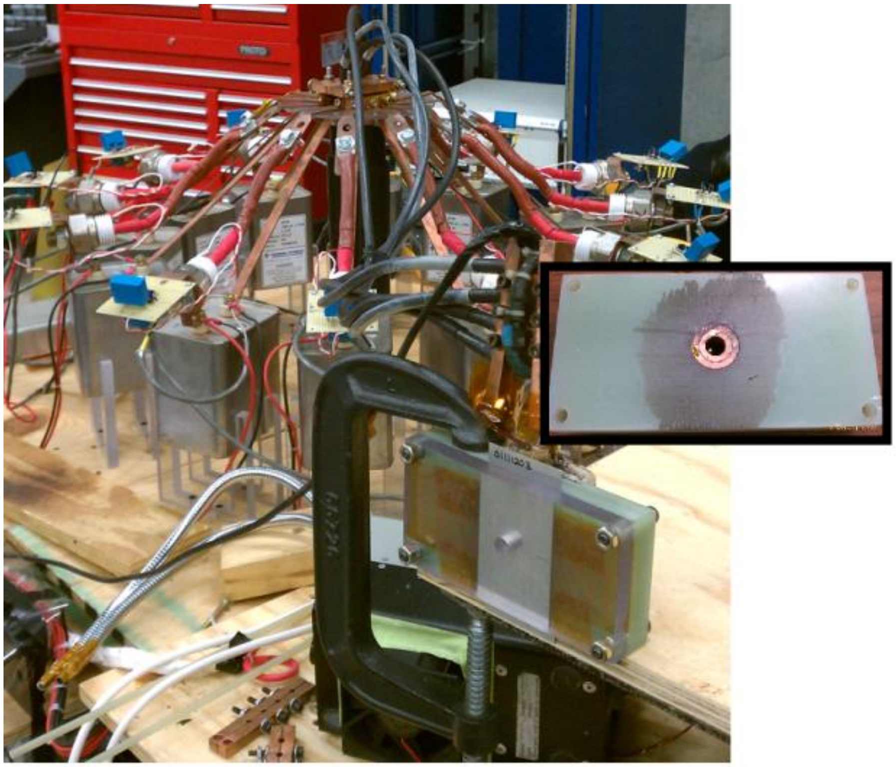

Figure 3.4. The modified pulsed-power supply is shown in the background, and the inductive-output section appears in the foreground. The inset picture shows the two-turn coil.

The system could use a single coil, as seen in Figure 3.4, or it could be configured to use two coils; the coils would be positioned directly across from each other with the sample pressed between them. The control system was also modified for automated operation. A typical experiment using the automated operation consisted of 50 pulses at a rate of one pulse every 7 s. Figure 3.5 shows an electrical schematic of the system after these modifications.

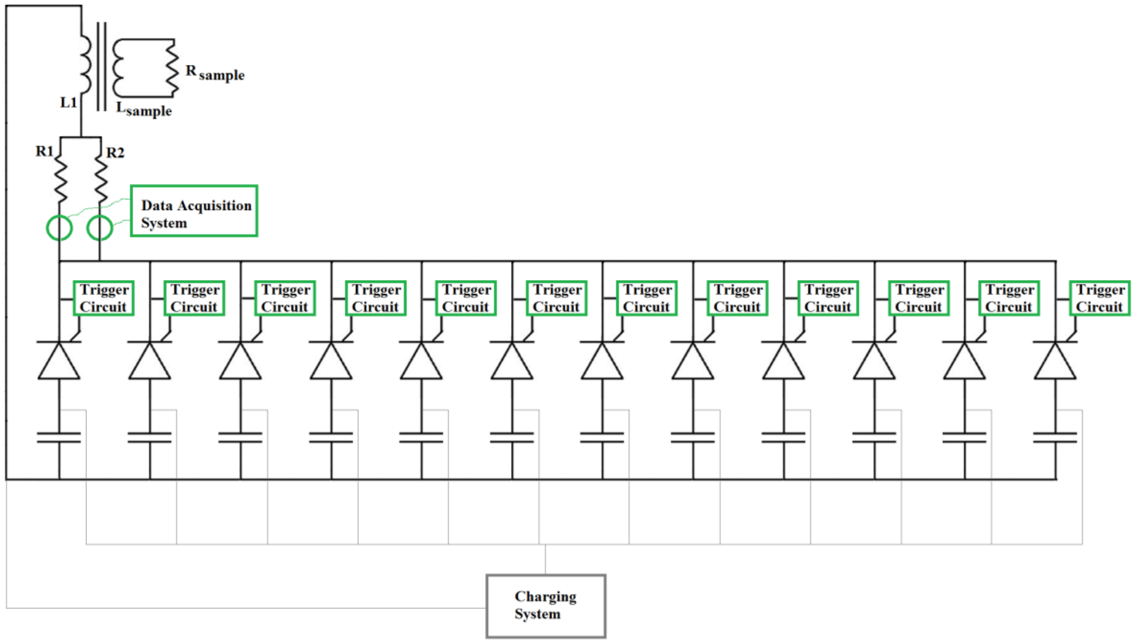

Figure 3.5. Electrical schematic of the first-generation system after the output section was modified for inductive operation.

The resistors R1 and R2 in Figure 3.5 represent the added resistance of the coax cables. Each coax cable had a resistance of about 20 mΩ, so about 5 mΩ was added into the primary discharge loop if four cables were used. An output current waveform after this addition is shown in Figure 3.6.

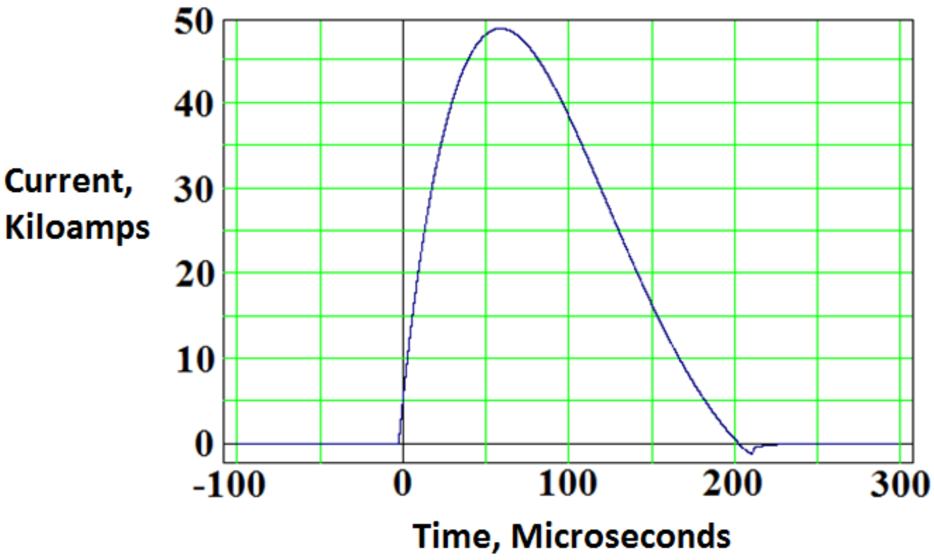

Figure 3.6. Output current for a 425 V experiment using the first-generation apparatus after it was modified for inductive operation.

The pulse duration was approximately doubled for single-coil operation and increased by about 60% for double-coil operation as the second coil and two additional coax cables decreased the effective loop resistance.

3.3 Second-Generation System Overview

The second-generation system was built with funding from the National Science Foundation (NSF). A solid model and a photo of the realized system are shown in Figure 3.7. Figure 3.8 shows the corresponding electrical schematic for this system.

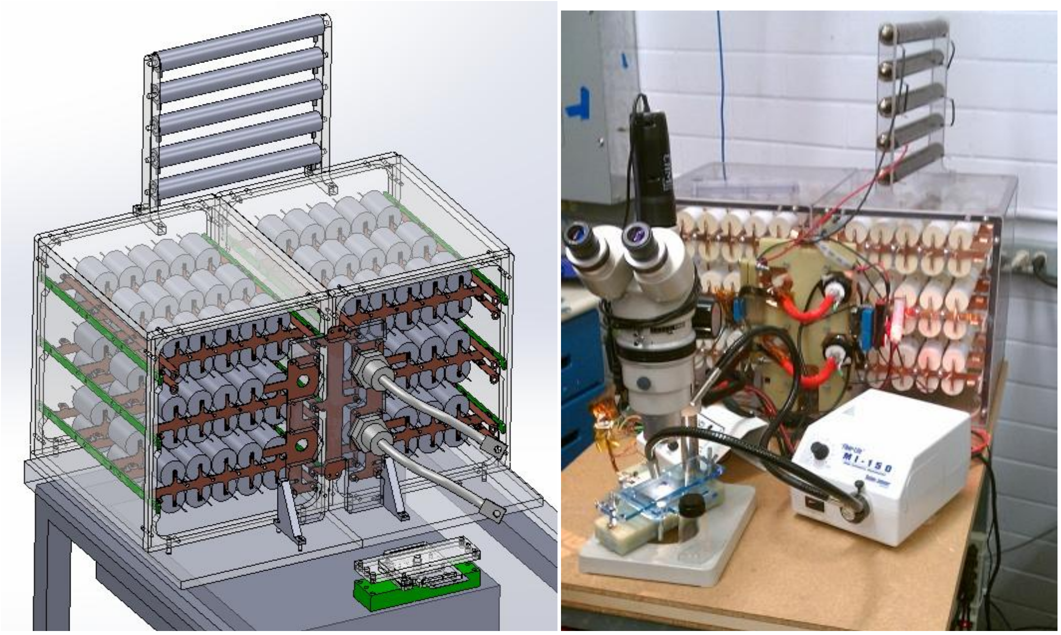

Figure 3.7. This figure shows the solid model (left) and the final second-generation test apparatus.

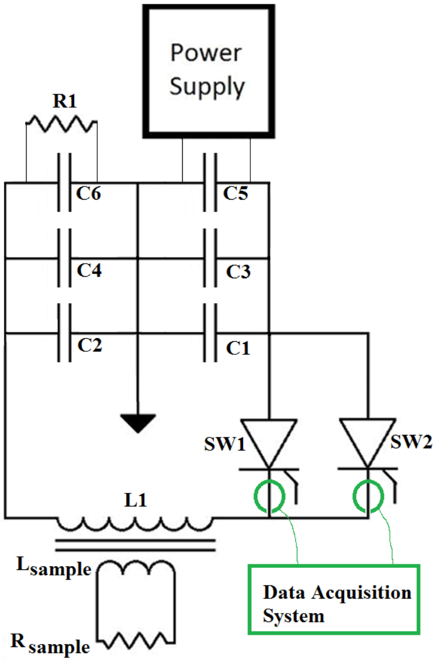

Figure 3.8. Simplified electrical schematic for the second-generation system.

The capacitors on the first-generation pulsed-power supply saw a modest voltage reversal of about 20%–30% after a pulse, despite the relatively high resistance in the output loop. This is at the upper limit of acceptability for the metalized-film pulse-discharge capacitors. In the second-generation system, a second set of capacitors was added to prevent this voltage reversal. The operation of the system seen in Figure 3.8 is as follows: First, the power supply charges the energy storage capacitors C1, C3, and C5 to a prescribed voltage. Capacitors C2, C4, and C6 are initially held at 0 V by R1. The experiment is initiated by SW1 and SW2 closing simultaneously and allowing current to flow through the primary coil (L1), which charges C2, C4, and C6. The energy stored in C2, C4, and C6 is discharged over a much longer timescale than the experiment, through R1. More efficient modes of operation that reuse this energy are possible, but for the purposes of this project simply discharging the energy was sufficient.

Each capacitor in the banks shown in Figure 3.7 is a 1 µF, 2 kV capacitor intended for snubber applications requiring high current pulses. Each of the capacitors shown in Figure 3.8 corresponds to one row of 30 capacitors in Figure 3.7. C1, C3, and C5 are the three rows of capacitors on the right, while C2, C4, and C6 are the three rows of capacitors on the left in Figure 3.7. The purpose of the three parallel sets of capacitors is to provide a simple way to reliably configure the system for three different waveforms.

The second-generation test apparatus was built specifically for NCMC and is over twentyfold more efficient than the previous version when efficiency is defined as distance of material removed divided by stored energy. Most of these gains result from both a waveform that is more closely matched to the skin depth of the materials being cut and a greater turn ratio between the coil and the sample. The thirteen-turn coil used in the majority of the experiments allowed the drive (or primary) current to be reduced by a factor of six from the current required for the first generation's two-turn coil. This lower current allowed for a thinner, more flexible output section while still providing more efficient operation due to the current-squared dependence of the resistive losses. A solid model of the output section is shown in Figure 3.9.

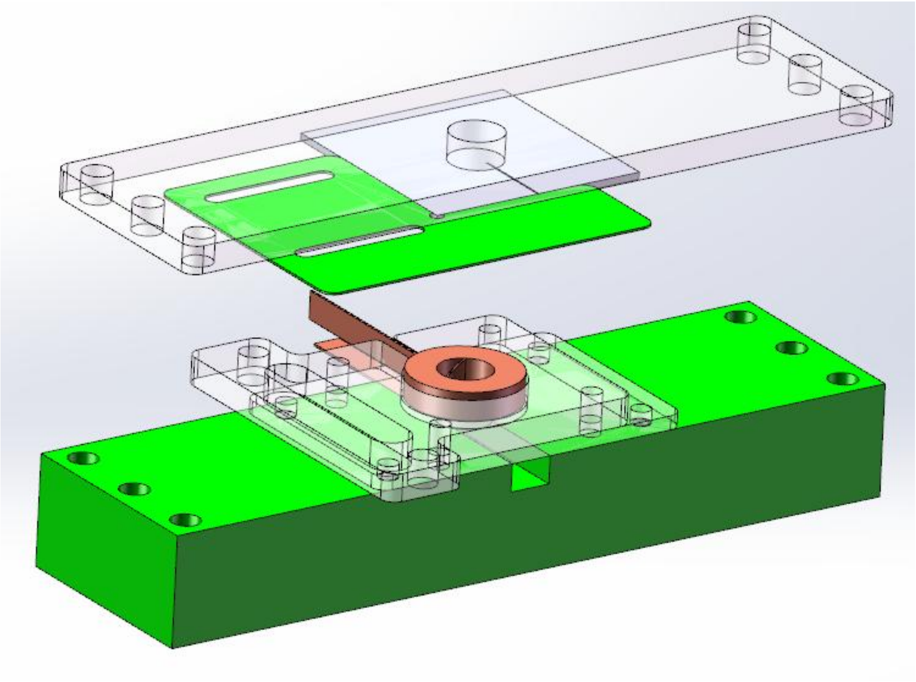

Figure 3.9. A solid model of the output section of the second-generation apparatus.

The green block at the bottom of Figure 3.9 is made out of G-10 fiber-reinforced resin and provides a stiff base to which the rest of the components are secured. The output coil is glued into a 6.35 mm thick acrylic part, which is secured to the G-10 base through a second acrylic block. It is important to control the alignment of the coil to the sample so that the experimental conditions are held constant for each test. To achieve this, one corner of a sample is indexed to the top plate by pressing it into a thin G-10 part, which is glued to the acrylic top plate. The diameter of the hole in the top plastic support is 12 mm. For multi-pulse experiments, the sample was secured to the top plate with double-sided tape. Figure 3.10 shows photographs of the output section without a sample and with a mounted sample.

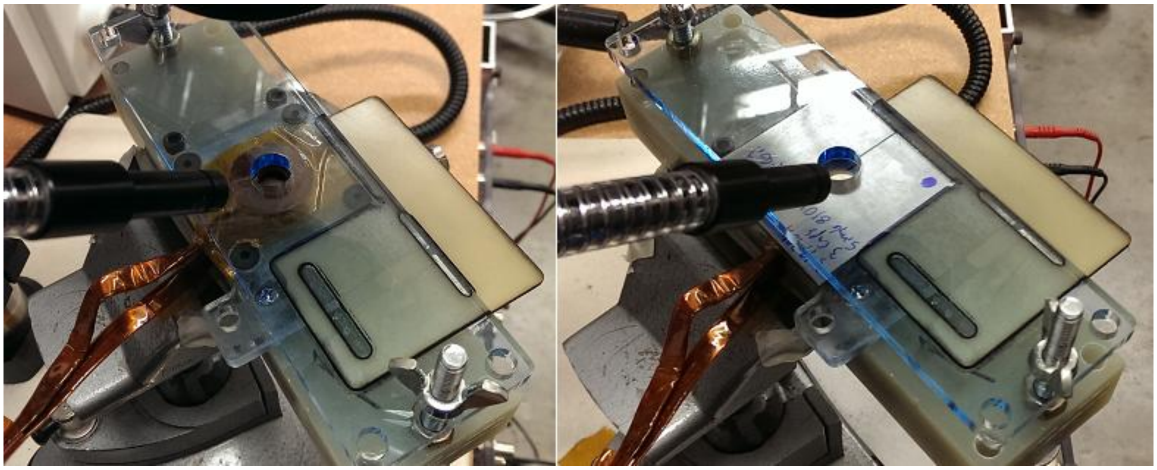

Figure 3.10. The output section alone (left) and with a mounted sample.

The coil used in these experiments had an outer diameter of 25.4 mm, an inner diameter of 10.7 mm, and was wound from copper ribbon measuring 6.3 mm by 0.5 mm.

The coil current is the main measurement taken experimentally. This measurement is made using two Rogowski coils, one for each of the silicon-controlled rectifier switches. The data is collected using a 12-bit National Instruments analog-to-digital converter card.

3.4 Experiments to Investigate the Onset of Magnetic Cutting

3.4.1 ELECTRIC DISCHARGE MACHINE STARTER CUTS COMPARED TO MAGNETIC SAW CUTS

The magnetic saw cuts produced by the first- or second-generation systems typically have a kerf between 10 µm and 100 µm. Since magnetic cutting relies on the previous cut to generate the enhancement point for the next cut, the starter cut should ideally be of these dimensions. The following investigation was conducted with larger-than-ideal (0.33 mm) starter cuts, because that is the finest starter cut that could be reliably produced. The samples were made using a wire EDM process, which provided a high degree of reproducibility from sample to sample. The samples measured 50.8 mm by 50.8 mm by 0.8 mm. The EDM starter cut had a kerf of 0.33 mm and extended 22.2 mm into the sample.

A consequence of using larger-than-necessary starter cuts is that initiating the first few magnetic saw cuts requires higher current than is needed to produce the fine cuts that follow. The experiments described in this section establish the magnetic pulse needed to initiate magnetic sawing in 0.79 mm thick 6061 T6 aluminum plate from 300 µm wide starter cuts. The experimentally determined magnetic pulse is simulated using a finite element code to establish the approximate current densities and magnetic pressures present at the onset of cutting. These results are compared to the conditions necessary to extend the magnetic saw cuts in a steady-state mode of operation, which is the objective of a second set of experiments.

3.4.2 EXPERIMENTAL PROCEDURES

To establish the onset of magnetic cutting, samples were photographed, placed above the coil, and aligned such that the tip of the EDM starter cut protruded 2.9 mm into the coil. The samples were pulsed once, removed from the fixture, and photographed on both sides. The charge voltage of pulsed-power supply was varied from 800 V to 1400 V.

A second set of experiments was conducted to determine optimal conditions for extending magnetic saw cuts in a steady-state mode of operation. The samples created in the first set of experiments were clamped in the same location as in the single-pulse experiment but were secured using double-sided tape to prevent them from moving as a result of impulses produced during cutting. The samples were repetitively pulsed at about 1 Hz for 200 pulses at the prescribed voltage level. Then the samples were removed and photographed.

3.5 Initial Parametric Experiments with Aluminum Plate

3.5.1 EXPERIMENTAL OVERVIEW

The purpose of the following experiments was to establish the point of onset across three thicknesses and with three waveforms. Once the current that produced onset for a given sample was established, the geometry and excitation would be simulated using Maxwell 3D, in order to determine current distribution, heating, and pressure at the cut tip. The results of these simulations could be compared to test models for the onset of cutting.

The nine conditions that were tested are depicted graphically in Figure 3.11.

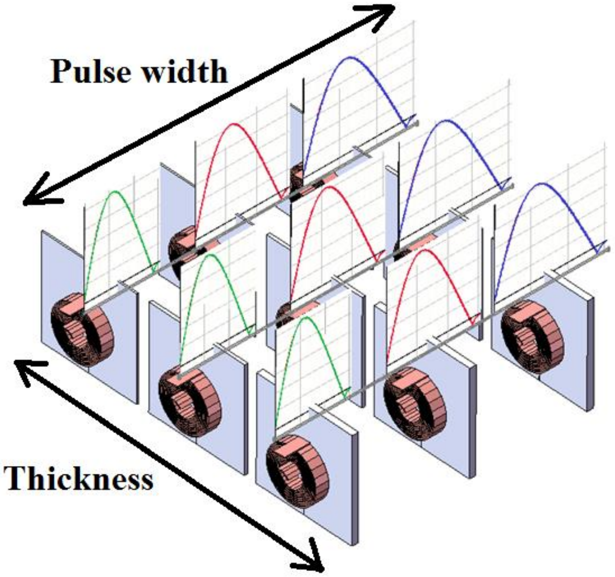

Figure 3.11. The nine test conditions for the initial parametric experiments with aluminum plate. The three thickness of plate are shown along with the coil-placement while the pulse type for each test is depicted above the samples.

Samples of 6061 T6 aluminum 0.79 mm, 1.6 mm, and 3.2 mm thick were used with three different pulse durations (17 µs, 25 µs, and 30 µs) for a total of nine sets of conditions. The goals were to:

1) Find the excitation that produced onset for a given material thickness and pulse duration.
2) Establish the band between the onset of cutting and bifurcations.

3.5.2 EXPERIMENTAL PROCEDURES

The pulsed-power supply was configured for a given waveform by connecting a number of rows of the capacitors from the active and passive capacitor banks. One, two, and three rows produced output currents with pulse durations of about 17 µs, 25 µs, and 30 µs respectively. The output current cannot be directly prescribed by the apparatus because it is influenced by the load, which includes the magnetically coupled sample. As such, the charge voltage was used as an independent variable, though the actual current was measured and these measured currents were used in the simulations to determine the conditions at the cut tip. Once the apparatus was set up, a sample was labeled and photographed under 10× magnification to establish the starting state. Then a sample would be mounted and a single current pulse of a given magnitude was applied. The sample was photographed again and 200 more pulses applied. The charge voltage of the apparatus was increased by 100 V, and the experiment was repeated using this greater excitation. If multiple sustained bifurcations were observed during a 200-pulse test, that set of conditions (material thickness and pulse duration) was discontinued as it was beyond the operating mode of interest. If no sustained bifurcations were observed, the current was increased by 100 V for each sample up to 1.9 kV, which was the maximum allowable charge voltage for the pulsed-power supply.

The purpose of using a fresh sample for each test was to eliminate the chance that a specimen could be damaged by previous lower-current experiments. Earlier work done with multi-pulse experiments showed that unobserved damage could accumulate and produce a fine cut and blowhole after repeated pulses.

3.6 Parametric Experiments with Aluminum and Copper Plate

3.6.1 EXPERIMENTAL OVERVIEW

These experiments were a refinement of the testing described in the previous section. The focus of these experiments was to find the onset conditions with copper as well as aluminum with a high degree of fidelity so that a method could be developed to predict the onset of cutting. These are two out of the three primary goals of this dissertation.

3.6.2 EXPERIMENTAL PROCEDURES

There were two types of tests used in this experiment, repeated-pulse tests and single-pulse tests. In the repeated-pulse tests, a sample was tested multiple times and observed while the charge voltage was increased by 25 V on each test until damage was seen. The excitation level where damage was observed was taken to be the minimum because of the possibility that previous current pulses had damaged the sample without being observed. The repeated-pulse test was not photographed as it was not considered as reliable as the single-pulse tests.

Once a repeated-pulse test had established the approximate excitation that caused the onset of cutting, single-pulse tests were performed to confirm and document the onset of cutting. For these tests, a sample was first labeled and fiducial marks were lightly scratched into the coil and non-coil sides. Then the sample was photographed under 10× magnification to establish the baseline state of the cut tip. The sample would then be mounted, pulsed, and photographed again. The onset of cutting was considered to be the excitation level that produced visible damage for a given set of experimental conditions. Once the onset of cutting was observed in a single-pulse experiment, additional experiments were done at this excitation level plus 20%, 40%, and 60%. For some tests, it was not possible to do all these tests due to the 1.9 kV voltage limit on the pulsed-power supply.

The purpose of these higher-energy tests was to provide inputs to exercise the numerical melt-only model and to give additional support to the onset point. The primary indication of onset was a light melt on the center of the rim of the EDM starter cut in a single-pulse test. This was not always a clear marker so having results for higher-energy cases with measurable cut distances provided further assurance that the onset case was indeed correct.

3.7 Printed Circuit Board Experiments

3.7.1 STARTER-CUT TECHNOLOGIES

A major problem in the study of the magnetic saw effect is the generation of starter features. Features that are small enough to study the effect in a regime similar to that observed in flaws are difficult to make in a manner controlled enough to be reproducible. EDM cutting has often been used [14, 16], with features as fine as 0.33 mm. EDM technology is capable of smaller feature sizes, but practical considerations generally limit it to the 0.33 mm kerf.

An alternative approach to producing samples with fine features is to use PCB technology. The PCBs used in these experiments have a much smoother surface finish than the EDM samples used in the previous experiments.

3.7.2 PRINTED CIRCUIT BOARD TEST SAMPLES

Figure 3.12 shows a solid model of the PCB test samples. The fiberglass substrate is rendered semi-transparent so that the top and bottom copper layers are visible. The workpiece section of a PCB sample measures 44.5 mm across and has a slit extending nominally 12.7 mm from one edge. The kerfs of the slits are 0.44, 0.28, and 0.20 mm ± 0.01 mm, measured from enlarged digital images taken with a calibrated 10× microscope.

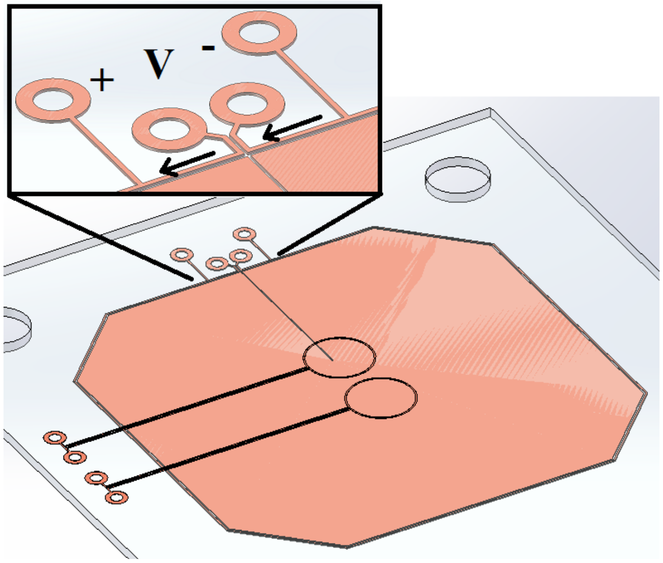

Figure 3.12. A solid model of the components of a PCB sample. The inset shows the leads of the Kelvin-type resistance-measuring loop, which surrounds the workpiece section of the copper. The two loops on the top surface can be used to measure the change in magnetic field for simulation validation purposes.

The plating thickness of a one-ounce copper layer is nominally 0.036 mm. The built-in Kelvin-type resistance measurement (see Figure 3.12 inset) was used to measure the average thickness of each sample. The plating thickness was computed by measuring the dimensions of the loop using calibrated microscope images and by assuming a resistivity close to pure copper. The calculated plating thickness was 0.036 mm and the standard deviation in thickness across the samples was 7.5% of the total.

3.7.3 APPARATUS OVERVIEW

The output section of the second-generation apparatus was modified to provide better alignment for the PCB experiments. Since holes could accurately be cut in the PCB samples at no extra cost, four outer holes were used for alignment rather than indexing from a corner as was done with the EDM samples. Figure 3.13 shows the modified output section.

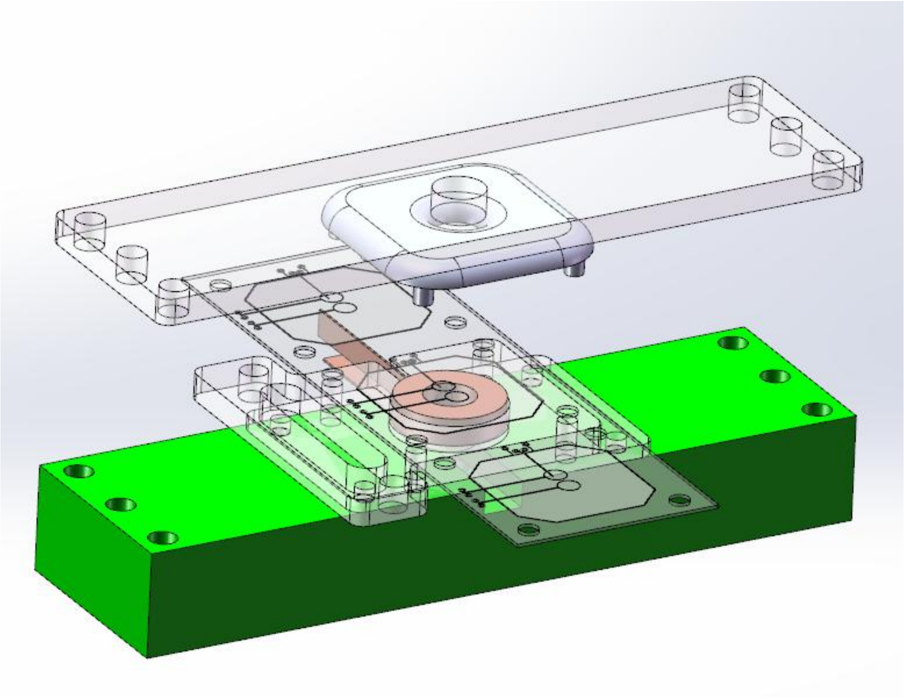

Figure 3.13. The modified output section for the PCB experiments.

Each PCB contained three samples corresponding to kerf dimensions of 0.20, 0.28, and 0.44 mm, which reduced costs and made for easier organization. This sample design is shown semi-transparent in Figure 3.13 so that the coil beneath it is visible. A fused deposition modeling 3D printed plastic part was used to secure the sample to the acrylic block that supports the coil.

A simplified model of the sample and coil and a photograph of a sample mounted below a microscope are shown in Figure 3.14.

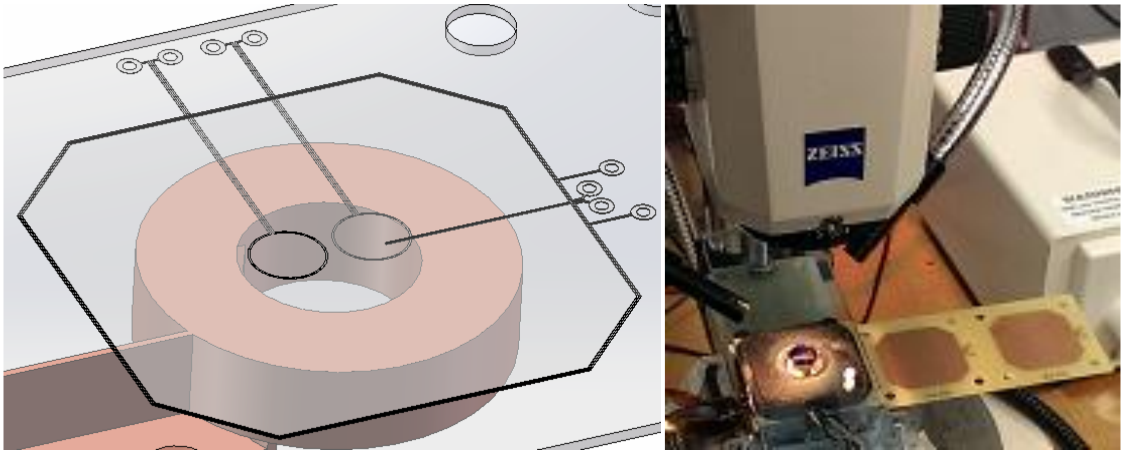

Figure 3.14. Left, a simplified solid model of a sample suspended above a drive coil. On the right, a sample is mounted above the drive coil.

The stereo microscope allowed viewing of the cuts as they were made. However, a consequence of this ease of viewing was that the conductor of the sample was on the opposite side of the substrate from the coil.

The two small circular loops were on the coil side of the sample. These loops were electrically isolated from both the test sample and the drive coil and were used as magnetic field (B-dot) sensors. The change in magnetic field measured by the circular loops was used to provide a check to the simulations.

3.7.4 EXPERIMENTAL PROCEDURES

To find the threshold of damage, test articles were mounted above the drive coil and single pulses of current were applied. The voltage on the pulsed-power supply was increased in 25 V increments until damage was observed. At that point a new sample was tested at the voltage where damage was first observed to ensure that previous tests had not somehow weakened the original sample leading to a premature failure.

Once the threshold for damage was established for each of the three kerf dimensions, the damaged samples were photographed. For each sample type, five additional tests were run to establish how the cut distance progresses at higher currents. These tests were conducted at the threshold voltage plus 10%, 20%, 30%, 40%, and 50% increases in voltage. Since current scales approximately as voltage, and energy as voltage squared, the peak test conditions correspond to an approximately 50% increase in current and a greater than doubling of the energy deposited onto the workpiece.

CHAPTER 4. RESULTS

This section describes the results from five distinct experiments and simulations that were discussed in the previous two chapters. The first section summarizes the simulation-only results from the centerline simulation series. This series takes a “big picture” perspective and investigates how sample thickness, sample position on the centerline, and pulse width affect the conditions at the cut tip. Section 4.2 summarizes the results from the threshold experiments on 0.79 mm thick 6061 T6 aluminum plate. Section 4.3 presents the results of an expanded experimental series that investigates cutting across three thickness and three pulse durations. This series used 6061 aluminum plate and found the onset conditions to a precision of 100 V on the apparatus. Section 4.4 describes another series performed with a copper alloy, Al-25, that employed finer granularity, and an improved criterion for cutting. Section 4.5 describes the final series of experiments, which used PCBs for the samples and investigated how the feature size (kerf) affects the excitation level that causes the onset of cutting.

4.1 Centerline Simulation Results

These results are for a series of simulations that investigate how three major factors influence conditions at the cut tip. Unlike the subsequent results sections, these results do not directly correspond to any experiments. The transient results from the center case of the test matrix are shown first to give the reader an understanding of the results before displaying the full results in reduced form. The trends in the results are more easily seen in reduced data form, since the matrix’s 63 elements make direct comparison of the transient results cumbersome. Though these simulations were not meant to simulate any particular cases, the center case uses values that are close to conditions known to produce magnetic saw cuts. From this starting point, the simulations are intended to provide a guide to how the sample thickness, sample position on the centerline, and pulse width change the conditions at the cut tip—whether or not these new conditions would actually produce magnetic saw cuts.

4.1.1 TRANSIENT RESULTS FROM THE CENTER CASE

Table 4.1 shows the setups for each of the 63 simulations from this series with the center case highlighted.

Table 4.1. The conditions for the 63 centerline simulations with the center case highlighted.

Specimen thickness:	**0.79 mm**			**1.57 mm**			**3.15 mm**		
Pulse length:	17 μs	25 μs	30 μs	17 μs	25 μs	30 μs	17 us	25 μs	30 μs
Position:	-6 mm	-6 mm	-6 mm	-6 mm	-6 mm	-6 mm	-6 mm	-6 mm	-6 mm
	-4 mm	-4 mm	-4 mm	-4 mm	-4 mm	-4 mm	-4 mm	-4 mm	-4 mm
	-2 mm	-2 mm	-2 mm	-2 mm	-2 mm	-2 mm	-2 mm	-2 mm	-2 mm
	-0 mm	-0 mm	-0 mm	-0 mm	-0 mm	-0 mm	-0 mm	-0 mm	-0 mm
	+2 mm	+2 mm	+2 mm	+2 mm	+2 mm	+2 mm	+2 mm	+2 mm	+2 mm
	+4 mm	+4 mm	+4 mm	+4 mm	+4 mm	+4 mm	+4 mm	+4 mm	+4 mm
	+6 mm	+6 mm	+6 mm	+6 mm	+6 mm	+6 mm	+6 mm	+6 mm	+6 mm

The center case is a 25 μs, 4 kA peak current, waveform applied to a 1.57 mm thick sample with the cut tip centered in the coil (the 0 mm position). Figure 4.1 shows transient plots of the power lost and the pressure on the inner4 element, which is at the cut tip. This was described in section 2.2.1.

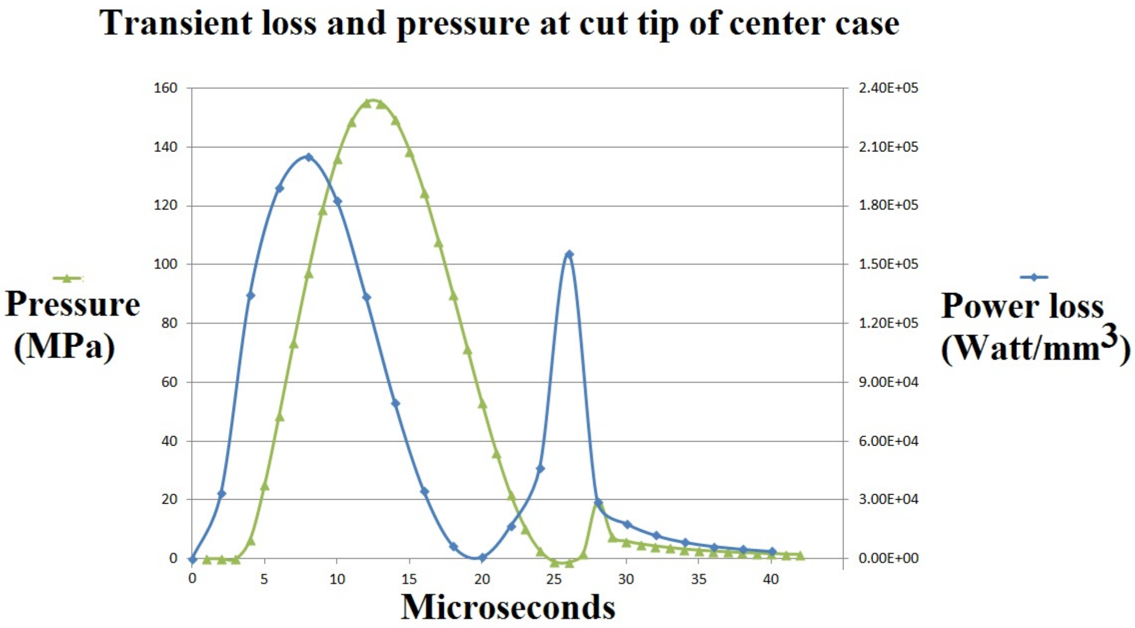

Figure 4.1. The transient power loss and pressure at the cut tip, for the center-case simulation.

Figure 4.1 illustrates how the power loss at the cut tip leads the pressure and has a more substantial second peak toward the end of the pulse, when the magnetic field is diffusing out. This trend appeared in all the results from this series, although the relative magnitudes of the peak pressures and power losses change with the simulation conditions. The full results of peak power, total energy lost, and peak pressure are described in reduced data form later in this section.

Transient plots of the forces on the remaining elements described in Figure 2.10 are shown in Figure 4.2.

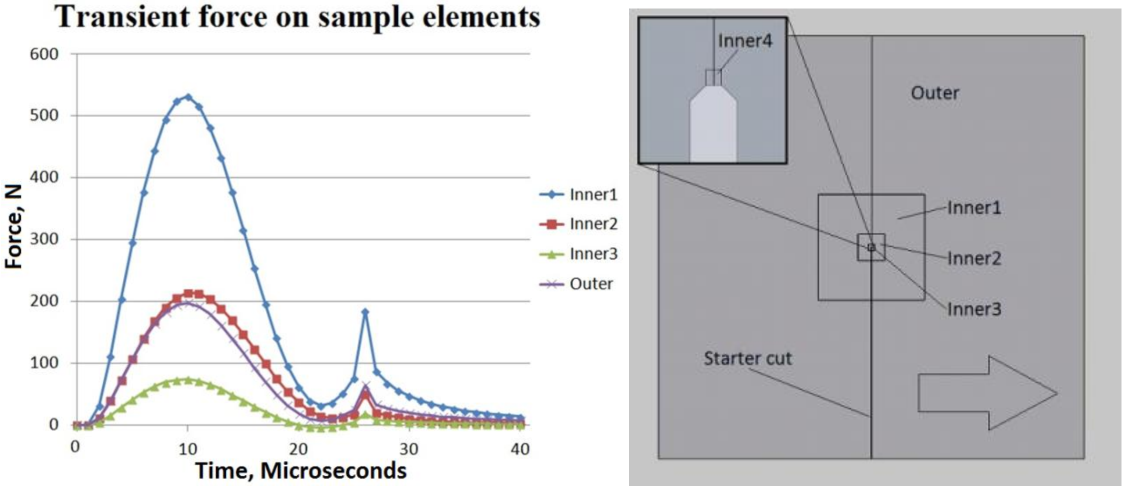

Figure 4.2. This plot shows the transient forces on the elements away from the cut tip for the center-case simulation.

The forces shown in Figure 4.2 can be converted to average pressures by assuming that the forces are applied evenly to the associated surfaces. Considering these average pressures, only the element Inner1 has a significant peak pressure of about 70 MPa.

Significant repulsion forces are produced between the coil and sample during pulses. The impulses for these forces are relatively low, but for repetitive experiments, they can accumulate and cause movement of several millimeters if the coil and sample are not adequately constrained. Figure 4.3 shows the transient repulsion force between the coil and sample in the center case.

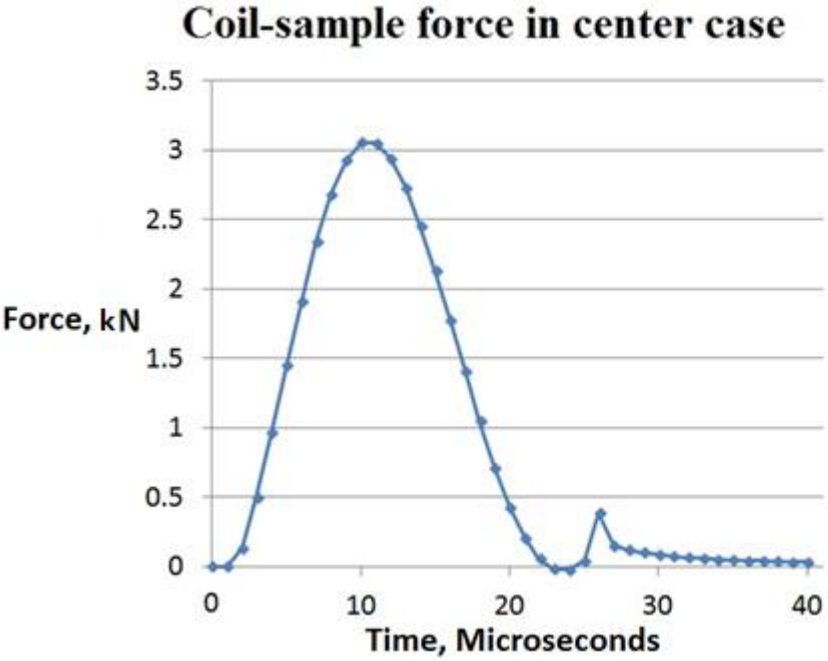

Figure 4.3. The transient coil-sample repulsion force for the center case.

Though the peak force on the coil for the center case is over 3 kN, the impulse is only 0.036 kg*m/s due to the relatively short pulse width. The reduced data results focus on the impulse, since inertia in the constraint system would probably keep the peak force from being directly reacted. The coil-sample impulse results from the rest of the simulation cases are presented later in this section.

4.1.2 REDUCED RESULTS FROM THE 63 CENTERLINE SIMULATIONS

The most noteworthy results from the 63 centerline simulations are presented to show how changes in position, material thickness, and pulse width affect the conditions at the cut tip and coil-sample repulsion impulses.

The peak power loss results for the 63 parametric simulations are shown in Figure 4.4.

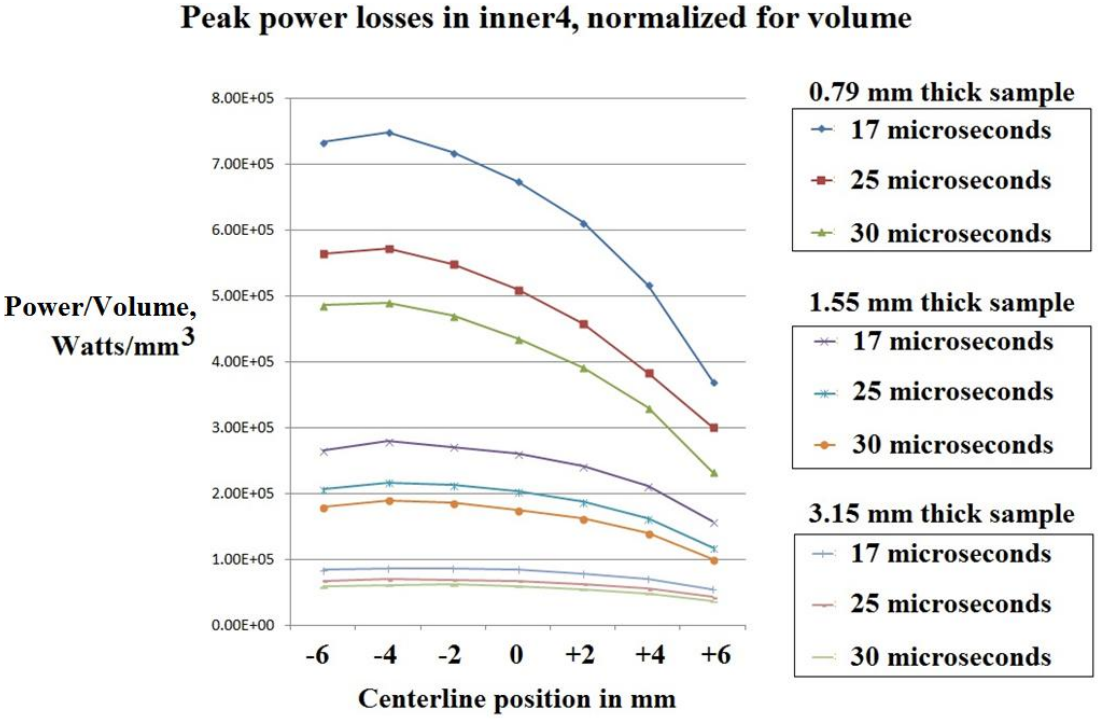

Figure 4.4. Peak power lost in Inner4 for the 0.79 mm, 1.57 mm, and 3.15 mm thick samples.

The *x*-axis shows the distance of the cut tip along the centerline of the coil, with 0 mm being the cut tip at the center of the coil. The simulation results suggest that if the cutting process is primarily melting, then the cut distance per pulse should be maximum at a position of about –4 mm from the centerline for these coil and sample geometries. The peak power lost at Inner4 decreases considerably as the cut tip is moved away from the –4 mm position. In the case of the fastest pulse and thinnest sample, the power lost in Inner4 decreases by about 50% from peak; however, in the case of the slowest pulse and thickest sample, the decrease is only about 34%. This effect can largely be explained as follows. As the cut tip is moved further into the coil, the current is forced to take a longer path. This longer path adds resistance and stray inductance that is not coupled to the primary coil. Figure 4.5 depicts this effect for three coil-cut positions.

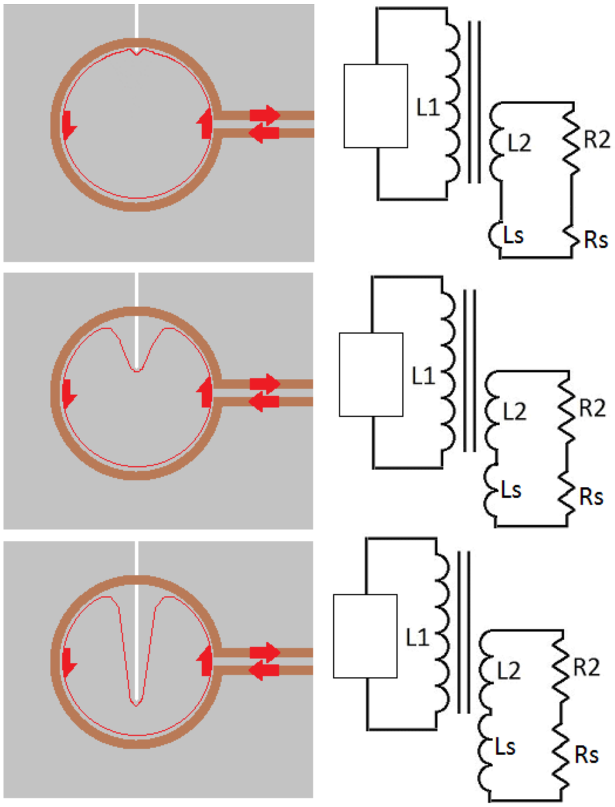

Figure 4.5. The figures on the left show the simplified coil and induced current paths for three different cut depths; the figures on the right illustrate simplified equivalent circuits.

In Figure 4.5, the added resistance and inductance are modeled as Rs and Ls. As the cut depth increases, both Rs and Ls increase. Each of those factors decrease the peak current induced in the sample. The effect of this increase is greatest in the thinner samples because resistance plays a larger role in determining the peak current in those cases. The resistance of the induced current in the sample is maximized in the case of the thinnest sample and the fastest pulse.

The peak power in Inner4 decreases from the –4 mm position to the –6 mm position in every case. This is probably because the cut tip in the –6 mm case does not protrude far enough into the coil to cause full diversion of the current in the sample. So although the –6 mm position maximizes the total current that is induced in the sample, this current is not forced to make a sufficiently sharp turn to maximize the power losses at the cut region.

Figure 4.6 shows the total losses in the Inner4 element, normalized for volume.

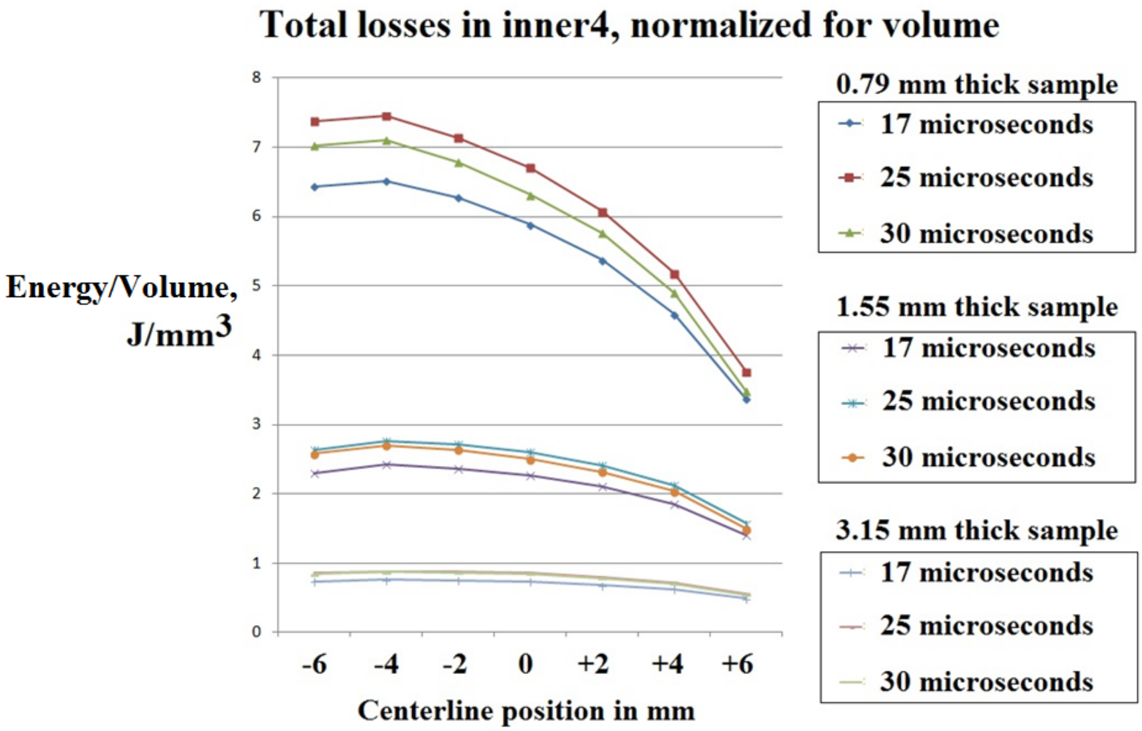

Figure 4.6. The total losses in Inner4 tip centerline simulation results.

The total losses plotted in Figure 4.6 are clustered into three groups based on material thickness. This trend is less apparent in Figure 4.4, indicating that the total energy losses per cubic millimeter are more dependent on material thickness than are the power losses. This is probably due to the material’s thickness influencing the effective pulse width of the power losses because the magnetic diffusion can only penetrate as far as the material’s thickness. Note that for the thinnest sample, the 25 µs pulse actually dissipates more energy in the cut region than the 30 µs pulse, even though the 30 µs pulse would require more energy to generate. This seems to indicate that the sample thickness is limiting the diffusion time for the 30 µs pulse, negating the advantage of having a longer pulse width. The 25 µs and 30 µs results are much closer for the thicker samples.

Figure 4.7 shows the peak pressure results from the centerline simulations.

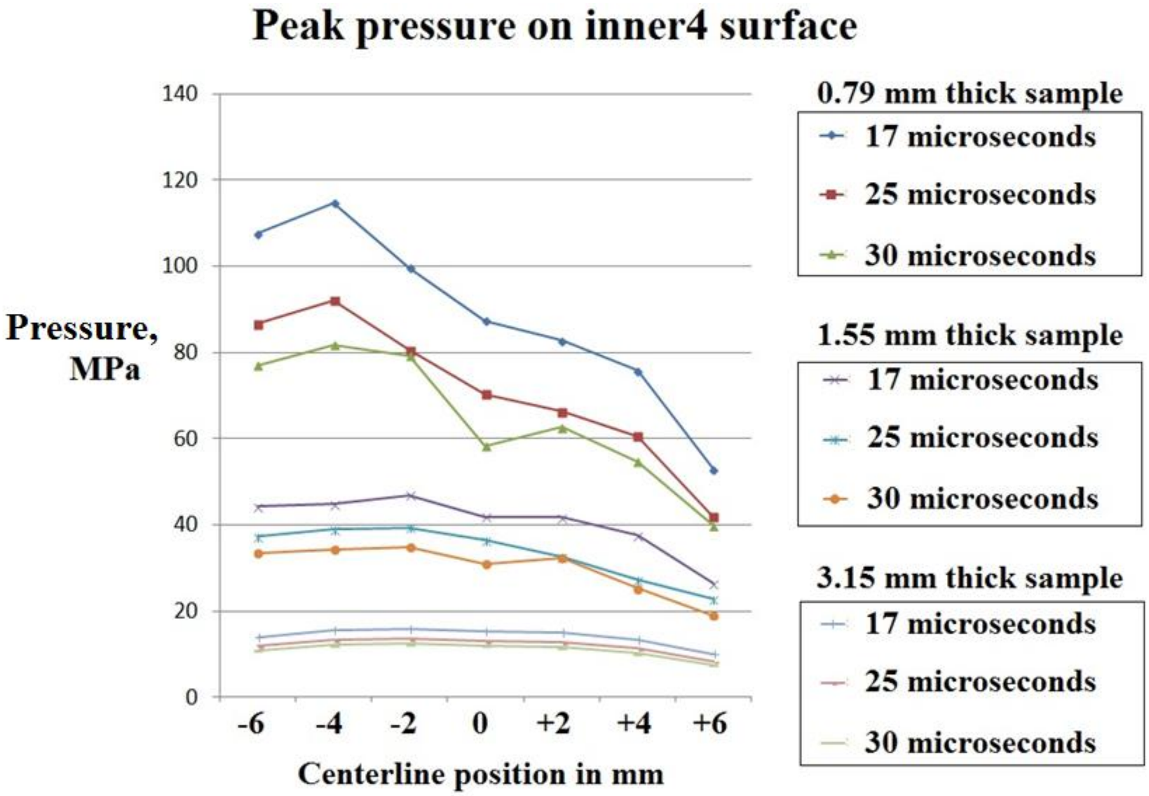

Figure 4.7. The peak pressure on the surface of Inner4 for the 63 centerline simulations.

The plots of the peak pressure on Inner4 look similar to the peak-loss plots shown in Figure 4.3. The positions with the greatest peak pressures are –2 mm to –4 mm, which is similar to the area of peak heating. The peak pressure results were found using the total force on the Inner4 element and applying this force to the inner surface, which does not take directionality into account.

The coil-sample impulse results for the centerline simulations are shown in Figure 4.8.

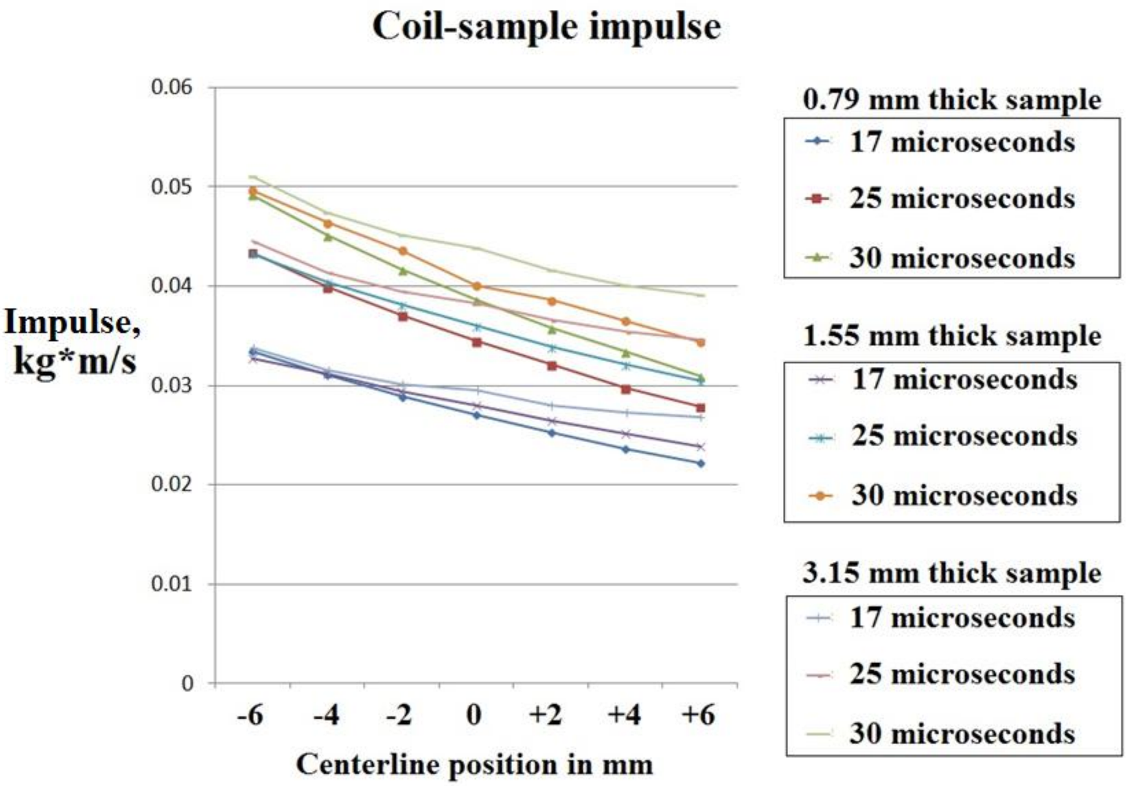

Figure 4.8. The peak coil-sample force for each of the 63 centerline simulations.

The results of Figure 4.8 cluster by triplets for the negative centerline positions but differ from the preceding results; the pulse width rather than the sample thickness determines the groupings. The sample thickness determines the rate at which the total impulse decreases as the cut protrudes further into the current's path (more positive centerline position). These results suggest that the coil-sample impulse can be reduced, even for thick samples, by shortening the duration of the excitation.

4.2 Cutting Onset Results in 0.79 mm Thick 6061 Aluminum

This section summarizes the results for the experiments to find the onset of cutting in 0.79 mm thick 6061 T6 aluminum plate. There were two types of experiments: single-pulse experiments using an EDM starter cut (section 4.2.1) and 200-pulse experiments where steady-state cutting was observed (section 4.2.2).

The results of the experiments are presented as photomicrographs, which document the changes to the cut-tip region after an experiment. Also included are the approximate transient energies and pressures at the cut tip, obtained by simulating the experimental conditions (measured geometry, material properties, and excitation) using the electromagnetic code, as described in section 2.2.2.

4.2.1 RESULTS OF SINGLE-PULSE EXPERIMENTS USING AN ELECTRIC DISCHARGE MACHINE STARTER CUT

Figure 4.9 shows the samples before and after a single pulse for each test.

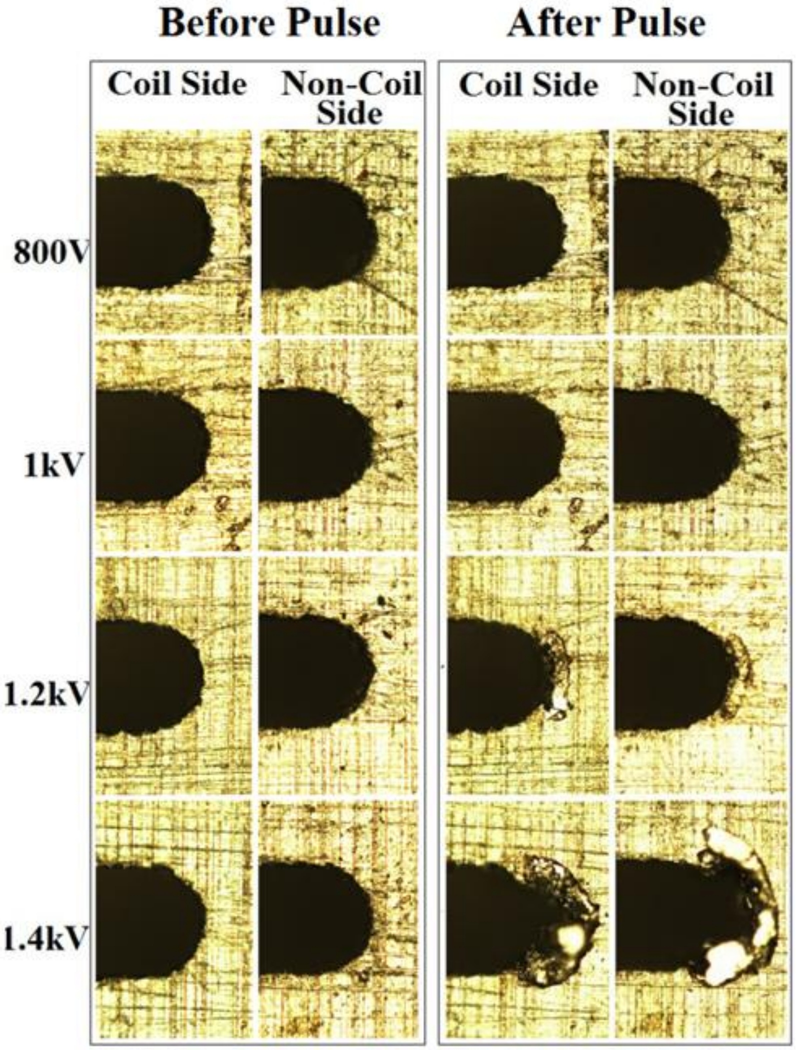

Figure 4.9. Photomicrographs of tested samples taken at 10× magnification. The kerf of the EDM cut is 0.33 mm.

No damage is visible at 800 V or 1 kV. At 1.2 kV, the center of the EDM starter cut appears to have melted and resolidified. At 1.4 kV, the melted region is much larger. Figure 4.10 shows the solid model used to calculate the current densities and forces on the workpieces.

The geometry was analyzed in a transient, 3D electromagnetic simulation using Maxwell 3D. The waveform captured during the 1.2 kV single-pulse experiment was applied as the excitation to the coil. Figure 4.10 shows the total force and power dissipated in the center keystone on the coil side.

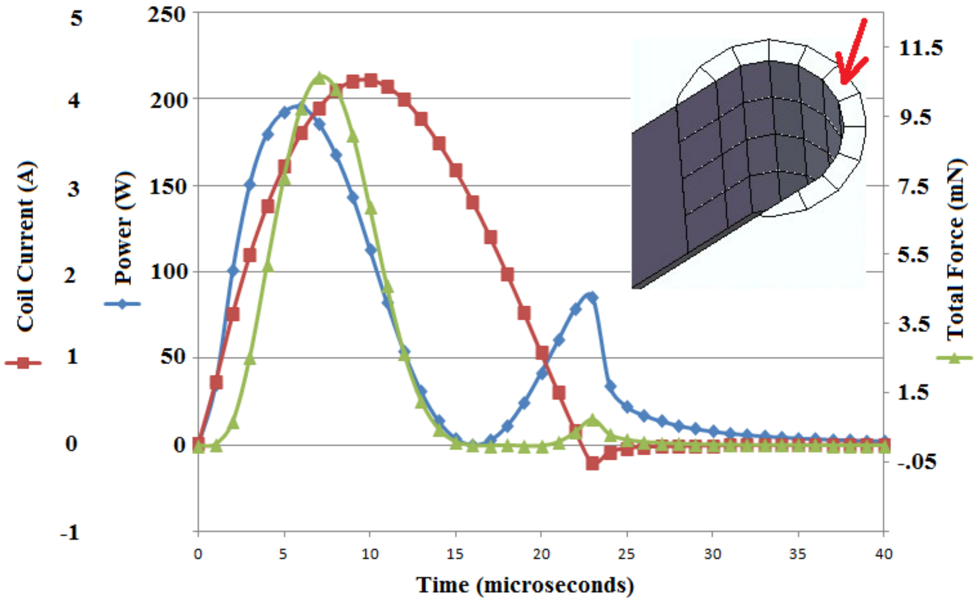

Figure 4.10. Transient plots of the coil current, power dissipation, and the total force in the center element on the coil side for the 1.2 kV case as well as the solid model used.

Integrating the power dissipated in this element and comparing the result to previously published energy-to-melt values for aluminum [18] suggests that the element melts at about 8 μs. The force applied to the corner element corresponds to a pressure of about 210 MPa. This pressure is not enough to yield room-temperature 6061; however, 6061 loses strength with increasing temperature [19, 20], so 210 MPa can be expected to deform material that is close to melting and certainly to eject material that has melted.

Figure 4.11 shows how power dissipation and applied force vary for elements down the centerline and radially from the center.

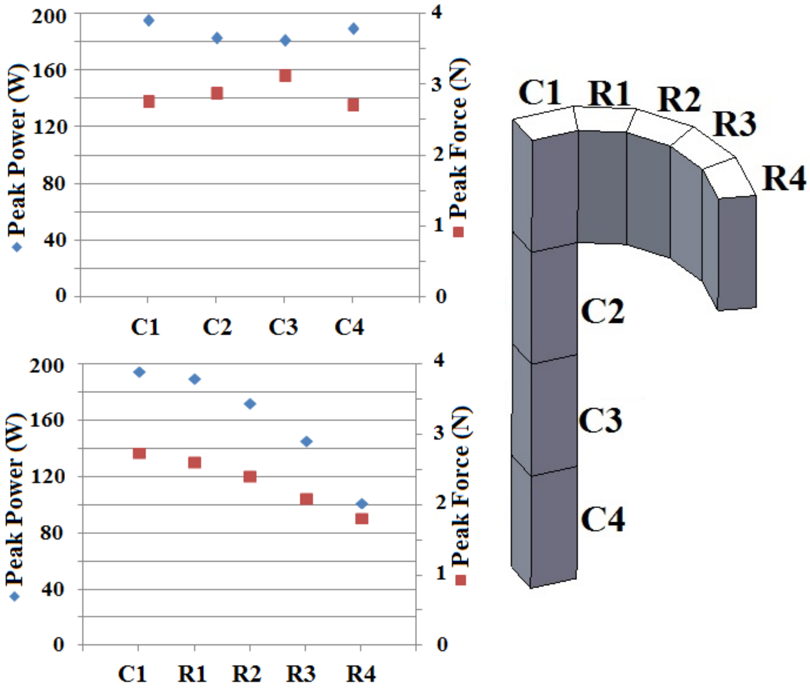

Figure 4.11. The peak powers and peak forces are plotted for the coil-side radius elements as well as for the centerline elements.

Figure 4.11 also shows significantly more variation across the radius than down the centerline for both the peak force and the peak power. The power is highest for the outer elements (C1, C4), whereas the force peaks on the inner elements (C2, C3). The outer areas of cuts show signs of damage before the inner parts. This suggests that the primary damage mechanism is melt-based rather than pressure-based. The drop in peak current for radial elements suggests a possible mechanism for straight cutting. If the center element fails first, the cut should progress in a straight line.

4.2.2 Results of Steady-State Cutting, 200-Pulse Experiment

After the single-pulse experiments, the samples were reaffixed and 200 additional pulses were applied so that steady-state cutting could be observed. Figure 4.12 shows photographs of the results of these experiments.

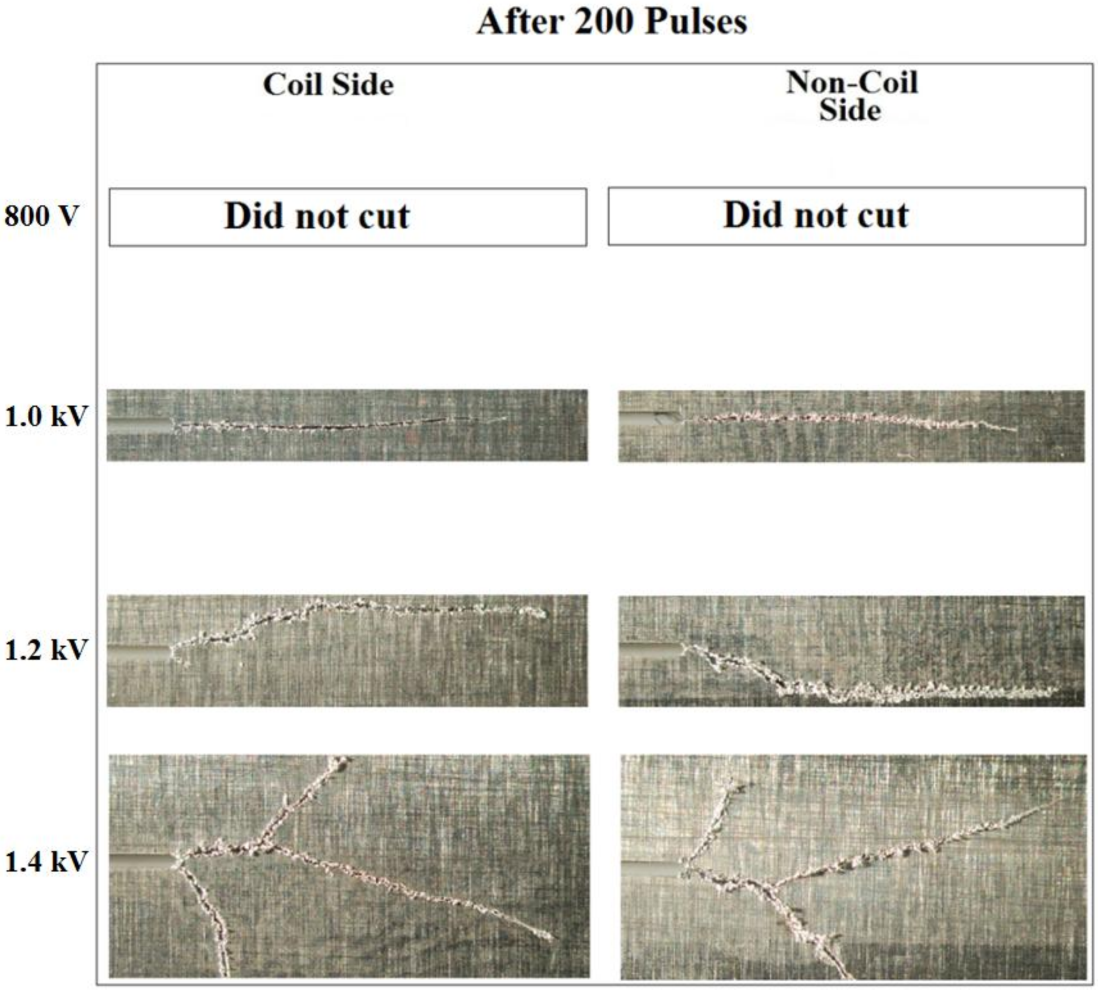

Figure 4.12. Results from magnetic saw cuts produced by 200 pulses applied repetitively at about 1 Hz.

At 800 V, no damage to the starter cut was observed. The overall resulting cuts from the 1000 V, 1.2 kV, and 1.4 kV experiments are shown.

The most noteworthy result from this series of experiments is that there is a relatively narrow range of conditions that produce acceptable cuts. Below 1000 V, cutting is difficult to establish and maintain. At 1000 V the best results are obtained; however, the cuts are still somewhat irregular. Above 1200 V, cuts are susceptible to bifurcations and are in any case difficult to control.

The geometries of the starter cut and steady-state cutting conditions are significantly different. Two simulations were run to compare the power loss and pressure at the cut tip for these disparate cases. Figure 4.13 shows the geometry observed experimentally as well as the solid models used to represent them. Figure 4.14 displays the excitation current, the heating, and the pressure at the cut tip.

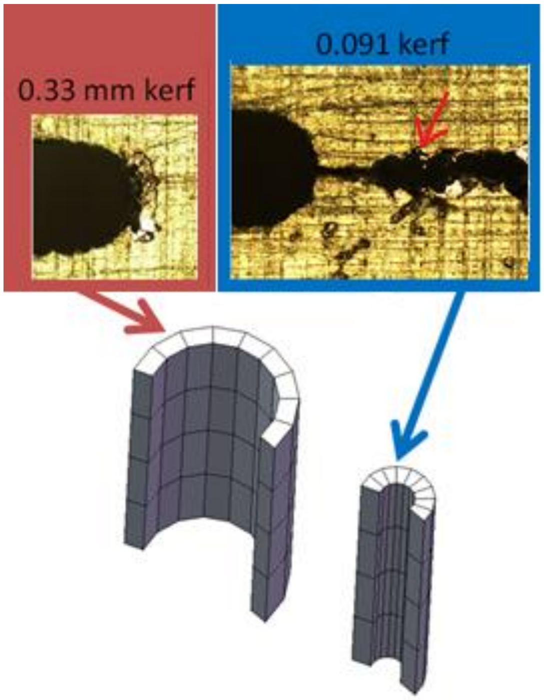

Figure 4.13. The photomicrographs show the observed geometries of an EDM starter cut and the steady-state magnetic saw cut. The solid models are representations of the starter features that were used in the simulations.

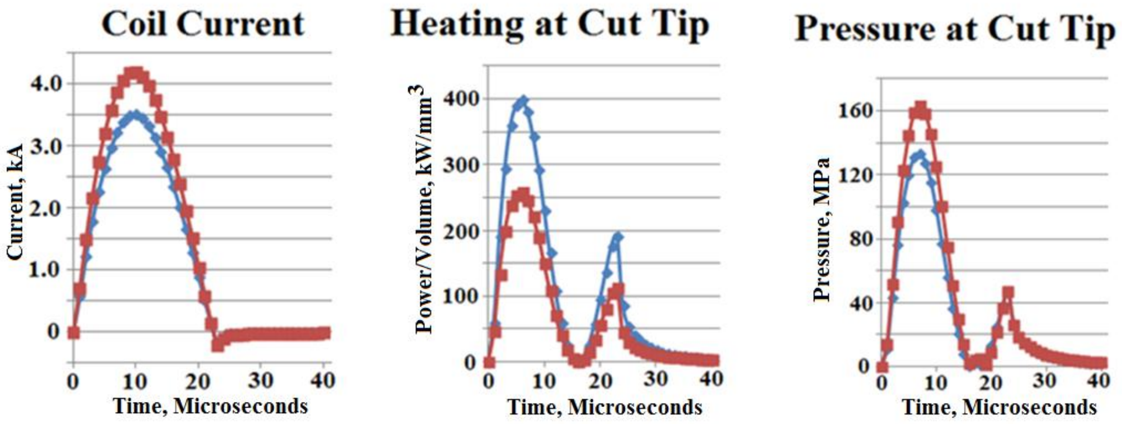

Figure 4.14. The excitation currents and the resulting heating and pressure at the cut tip for the EDM starter cut (red) and steady-state (blue) magnetic saw cutting cases.

Despite having a lower excitation current, the heating at the cut tip for the steady-state cutting case is significantly greater than the EDM starter-cut case. This shows the importance of starting feature size to the current enhancement. The pressures at the cut tips are proportioned similarly to the excitation currents. The steady-state cutting case has greater heating and less pressure than the EDM starter-cut case; since the cut advances significantly further in the steady-state cutting case, these results point to heating as the dominant mechanism, at least in these cases.

4.3 Initial Parametric 6061 Aluminum Plate Results

The initial parametric experiments using 6061 aluminum examines how the excitation level required to produce cuts changes across three material thicknesses and three pulse durations. The experiments found the operating band of non-cutting, cutting, and bifurcations for each material type. The results of simulations of the cutting conditions were examined to find what parameter is most correlated to cutting. Whereas the results of section 4.2 are presented as raw data in the form of photographs, the results of these experiments are presented in the form of reduced data. Once the experiments were performed, test coupons were visually inspected to determine which tests produced cuts. Table 4.2 shows an overview of the results of the test matrix.

Table 4.2. The experimental test matrix and observed results for the initial parametric 6061 aluminum plate experiments.

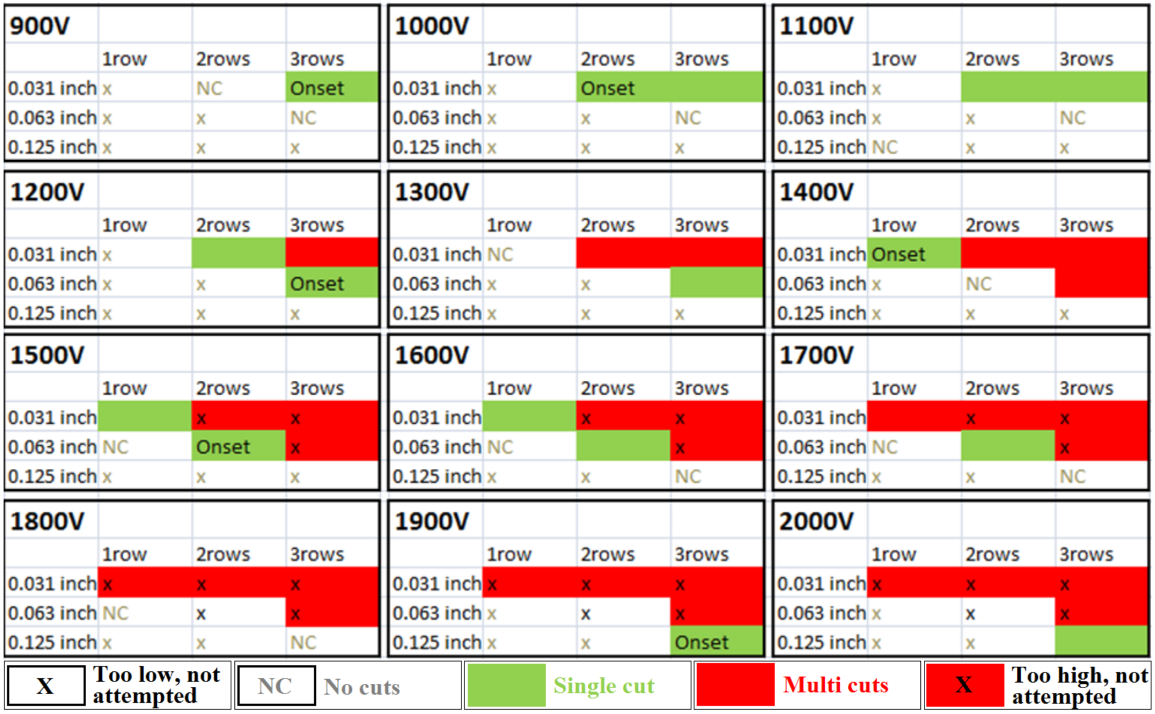

900V	1row	2rows	3rows
0.031 inch	x	NC	🟩 Onset
0.063 inch	x	x	NC
0.125 inch	x	x	x

1000V	1row	2rows	3rows
0.031 inch	x	🟩 Onset	🟩
0.063 inch	x	x	NC
0.125 inch	x	x	x

1100V	1row	2rows	3rows
0.031 inch	x	🟩	🟩
0.063 inch	x	x	NC
0.125 inch	NC	x	x

1200V	1row	2rows	3rows
0.031 inch	x	🟩	🟥
0.063 inch	x	x	🟩 Onset
0.125 inch	x	x	x

1300V	1row	2rows	3rows
0.031 inch	NC	🟥	🟥
0.063 inch	x	x	🟩
0.125 inch	x	x	x

1400V	1row	2rows	3rows
0.031 inch	🟩 Onset	🟥	🟥
0.063 inch	x	NC	🟥
0.125 inch	x	x	x

1500V	1row	2rows	3rows
0.031 inch	🟩	🟥 x	🟥 x
0.063 inch	NC	🟩 Onset	🟥 x
0.125 inch	x	x	x

1600V	1row	2rows	3rows
0.031 inch	🟩	🟥 x	🟥 x
0.063 inch	NC	🟩	🟥 x
0.125 inch	x	x	NC

1700V	1row	2rows	3rows
0.031 inch	🟥	🟥 x	🟥 x
0.063 inch	NC	🟩	🟥 x
0.125 inch	x	x	NC

1800V	1row	2rows	3rows
0.031 inch	🟥 x	🟥 x	🟥 x
0.063 inch	NC	x	🟥 x
0.125 inch	x	x	NC

1900V	1row	2rows	3rows
0.031 inch	🟥 x	🟥 x	🟥 x
0.063 inch	x	x	🟥 x
0.125 inch	x	x	🟩 Onset

2000V	1row	2rows	3rows
0.031 inch	🟥 x	🟥 x	🟥 x
0.063 inch	x	x	🟥 x
0.125 inch	x	x	🟩

X	Too low, not attempted	NC	No cuts	🟩	Single cut	🟥	Multi cuts	🟥 X	Too high, not attempted

The onset of cutting was considered to be the point where cuts would extend after multiple pulses; later experiments (sections 4.4 and 4.5) used a different criterion for the onset of cutting: the first signs of visible damage from a single pulse.

Maxwell 3D was used to find peak current density, peak magnetic field, and power and energy deposited in two 10 μm cubes. One of these cubes is illustrated in Figure 4.15.

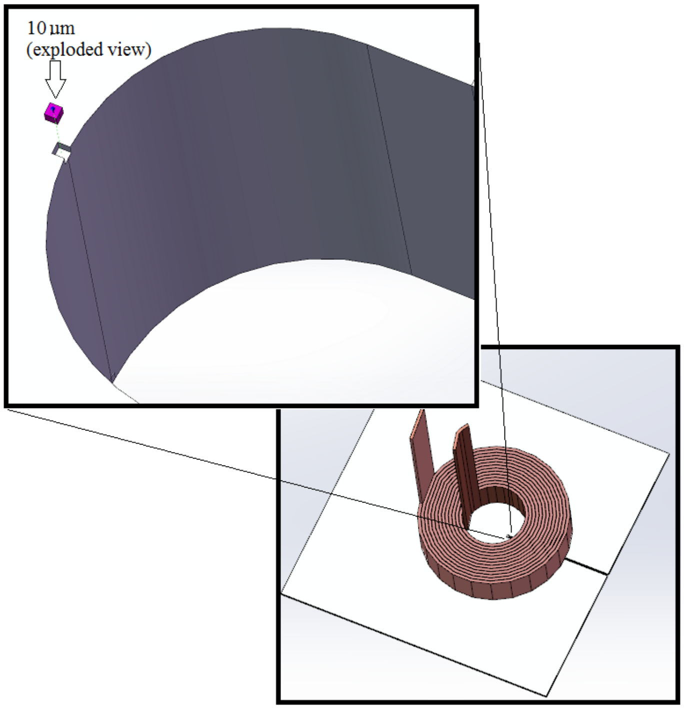

Figure 4.15. This figure shows the 10 µm cube on the coil-side surface of a model of the starter notch. The cube has been shifted up and highlighted for clarity. A similar cube is also on the surface of the non-coil side of the notch.

These 10 µm “nibble” cubes were positioned at the points on the top and bottom surfaces that were previously determined to have the highest current density (Figure 4.11). The details of how the tests were simulated to arrive at the values tabulated below are discussed in section 2.2.3. The results of these simulations are compared in Table 4.3 and Figure 4.16 in effort to find the parameter that remained most constant as the cutting conditions were changed.

Table 4.3. Results of simulating the conditions of the experiments on 6061 aluminum plate. The apparatus was not able to produce currents high enough to initiate cutting in some cases; these cases are marked out.

Specimen thickness:	**0.78 mm**			**1.6 mm**			**3.2 mm**		
Pulse length:	**17 μs**	**25 μs**	**30 μs**	**17 μs**	**25 μs**	**30 μs**	**17 μs**	**25 μs**	**30 μs**
Energy lost in coil-side nibble (J/mm^3)	1.91	2.28	2.74	-	2.28	2.18	-	-	2.34
Energy lost in non-coil-side nibble (J/mm^3)	1.82	2.18	2.63	-	2.09	2.00	-	-	1.92
Peak power lost in coil-side nibble (MW/mm^3)	0.226	0.206	0.201	-	0.216	0.177	-	-	0.202
Peak power lost in non-coil-side nibble (MW/mm^3)	0.216	0.196	0.201	-	0.198	0.163	-	-	0.17
Peak J (A/m^2)	9.2×10^{10}	8.8×10^{10}	8.9×10^{10}	-	9.0×10^{10}	8.2×10^{10}	-	-	7.9×10^{10}
Peak B (T)	17.2	17.5	18.2	-	20.3	19.1	-	-	19.1

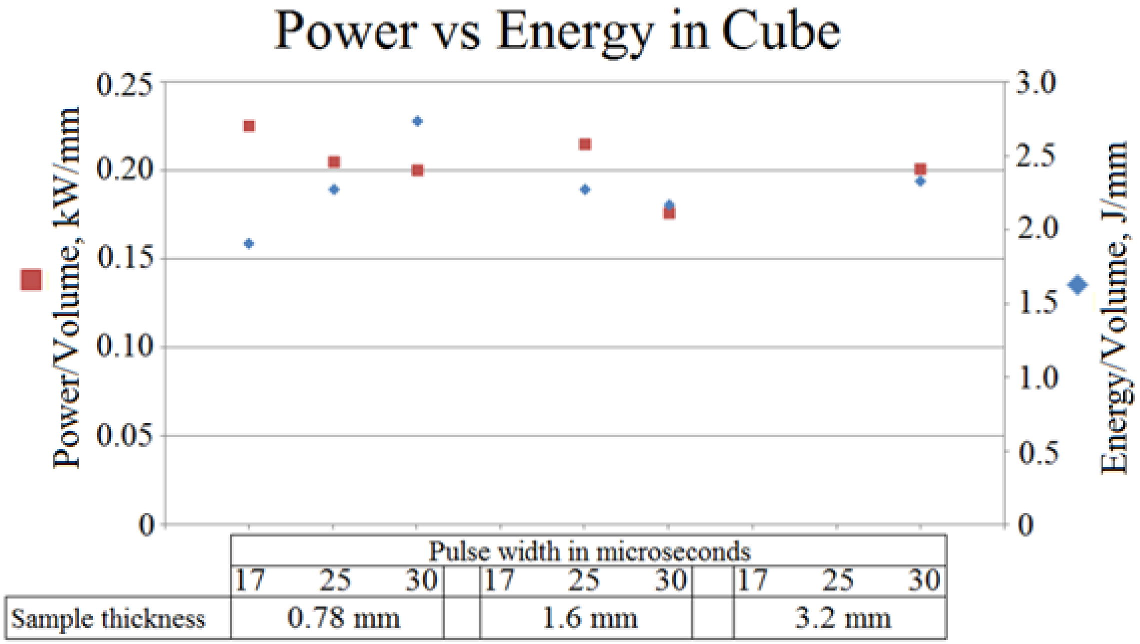

Figure 4.16. A plot of the power and energy dissipated in the coil-side 10 µm cube across the simulated results.

Table 4.3 and Figure 4.16 show that for a wide range of cases, there are quite narrow conditions at the onset of cutting. None of the parameters stands out as more constant than any other enough to make a convincing case, and there are not enough samples for statistics to be meaningful. All three pulse widths could only produce cuts in the thinnest samples because of limitations with the power supply, which greatly limits the conclusions one can draw about the effect of different pulse widths.

4.4 Parametric Aluminum and Copper Plate Results

The objective of these experiments is to establish the onset of cutting across two material types, three material thickness, and three pulse durations. These parametric experiments are a refined and expanded follow-up version of the experiments described in section 4.3.

The methodology was revised in order to find the threshold of cutting to a precision of 25 V of charge voltage on the apparatus. The experiments were expanded to include a copper alloy, Al-25.

The results from these experiments are presented starting from a broad perspective so as to show a simplified but comprehensive picture of all the experiments. The photomicrographs are shown for each experiment followed by tabulated results for the onset conditions. Then the results for the numerical melt-only model are presented for the higher-than-threshold experiments, and these results are compared to the measured cut distances.

4.4.1 OVERVIEW OF RESULTS

These experiments are divided into units where each unit consists of all the magnitudes of excitations for that particular setup. A setup consists of a particular material type, material thickness, and pulse duration. A complete unit consists of the excitation that produces the threshold of cutting (T0) for this setup as well as the threshold excitation plus 20%, 40%, and 60% (T20, T40, and T60 respectively). Due to limitations of the apparatus, complete results were not obtained from every setup. Table 4.4 shows the results obtained from each of the setups considered in these experiments.

Table 4.4. An overall map of the results of the experiments. The colors indicate the completeness of the results for each of the fifteen setups.

	6061 T6 Aluminum Plate			**Al-25 Copper**	
	0.41 mm	0.79 mm	1.55 mm	0.36 mm	0.83 mm
17 µs	T0–T60	T0, T20	N/C	T0, T20	N/C
25 µs	T0–T60	T0–T60	T0, T20	T0–T60	T0
30 µs	T0–T60	T0–T60	T0, T20	T0–T60	T0, T20

The onset of cutting is established for all but two setups, and complete results are available in seven out of the fifteen setups. For these experiments, the onset of cutting was considered to be the first signs of visible damage from a single pulse. As observed in previous sections, the thicker materials require greater excitations to cut, and the apparatus reaches its voltage limit at lower output current levels when it is configured to make the shortest pulse. This causes the diagonal bands seen in Table 4.4.

Photomicrographs for all the experiments are shown in Figures 4.17 through 4.22. The results are grouped into units, and all results from a given material thickness are presented on a single “page.” The two conditions where the onset of cutting could not be established have been omitted (6061 T6, 1.55 mm thick, 17 µs and Al-25, 0.83 mm thick, 17 µs). Each page of photomicrographs corresponds to one of the columns of Table 4.4; this relation is reinforced by a box around each unit of photomicrograph results that corresponds to its cell in Table 4.4. This relation is shown in Figure 4.17.

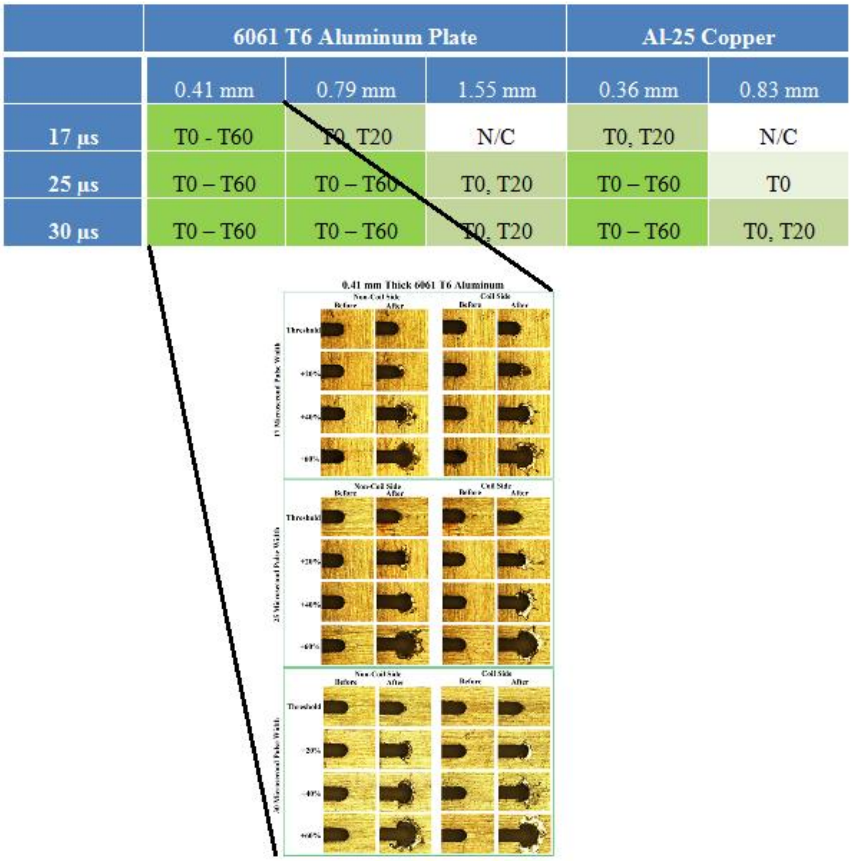

	6061 T6 Aluminum Plate			Al-25 Copper	
	0.41 mm	0.79 mm	1.55 mm	0.36 mm	0.83 mm
17 µs	T0 - T60	T0, T20	N/C	T0, T20	N/C
25 µs	T0 – T60	T0 – T60	T0, T20	T0 – T60	T0
30 µs	T0 – T60	T0 – T60	T0, T20	T0 – T60	T0, T20

Figure 4.17. Each of the columns of Table 4.4 corresponds to one page of photomicrographs presented in the following section.

4.4.2 PHOTOMICROGRAPHS

Figures 4.18 thorough 4.22 show photomicrographs of the cut tip before and after the cutter pulse was applied, for each setup.

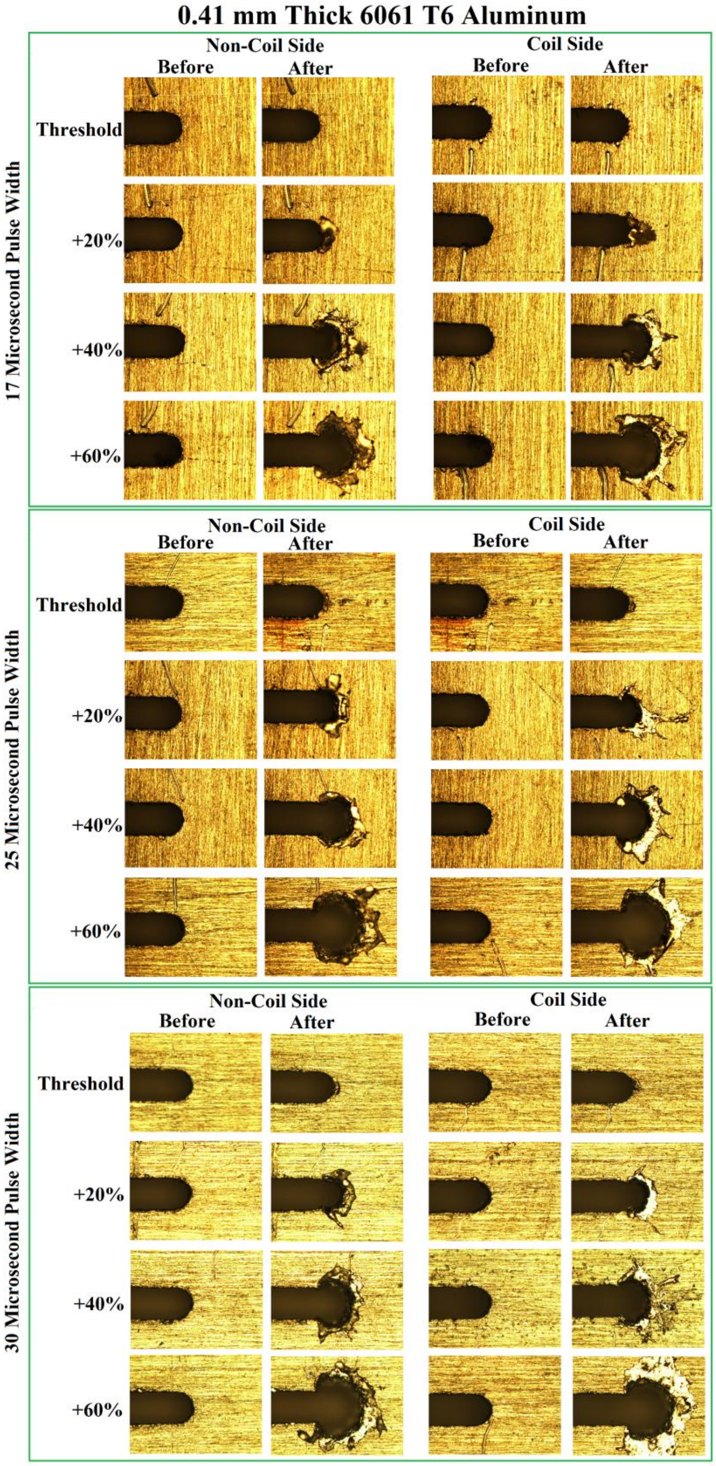

Figure 4.18. The photomicrograph results for 0.41 mm thick 6061 T6 aluminum.

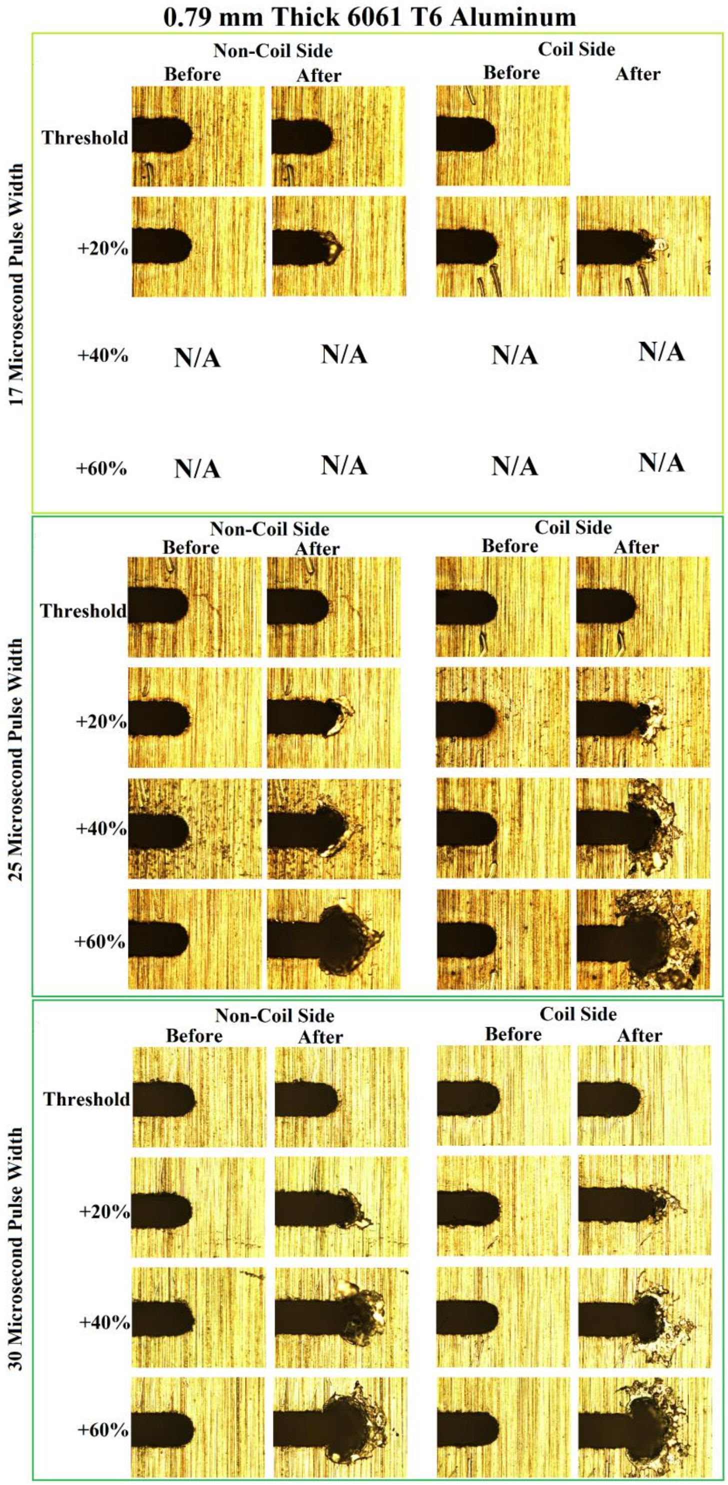

Figure 4.19. The photomicrograph results for 0.79 mm thick 6061 T6 aluminum.

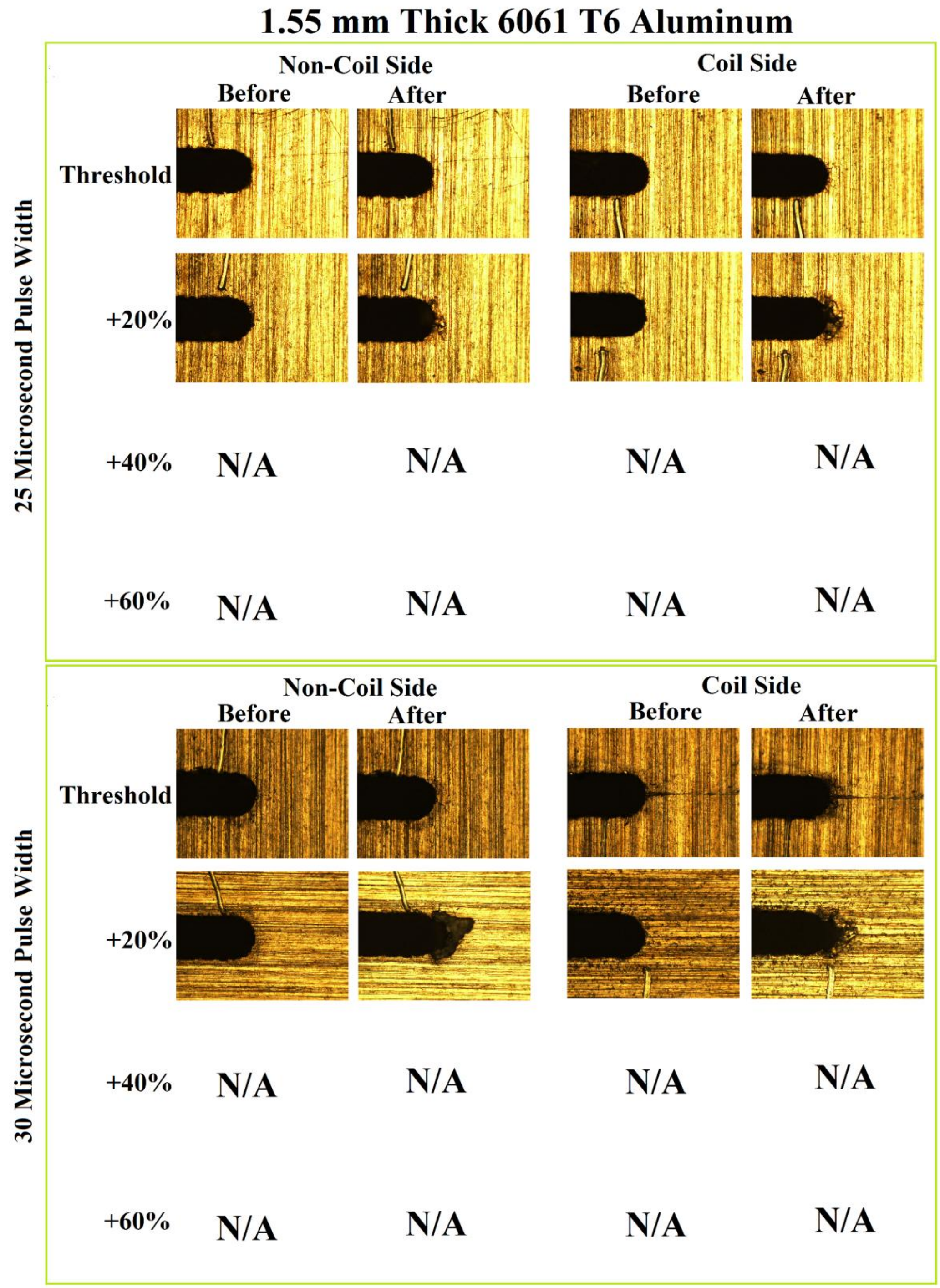

Figure 4.20. The photomicrograph results for 1.55 mm thick 6061 T6 aluminum.

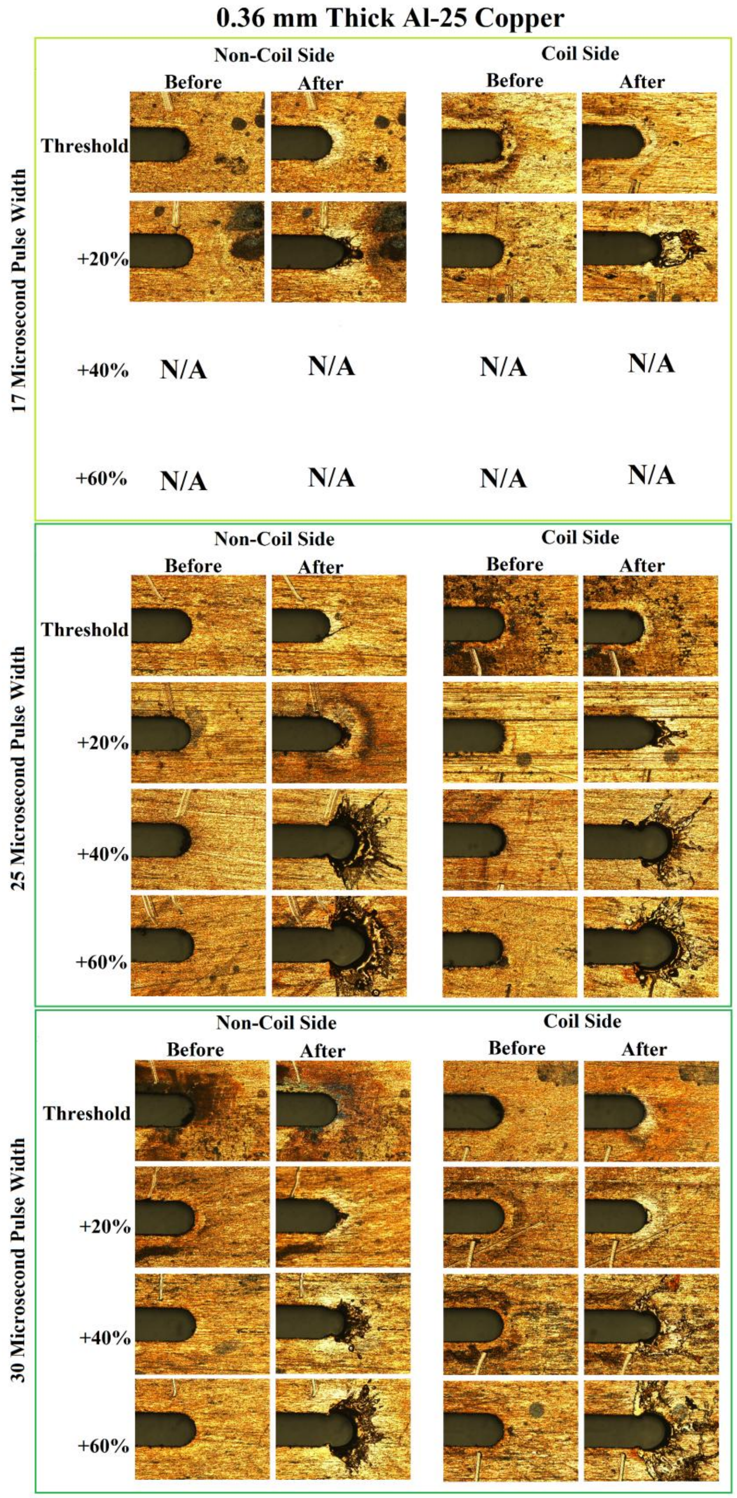

Figure 4.21. The photomicrograph results for 0.36 mm thick Al-25 copper.

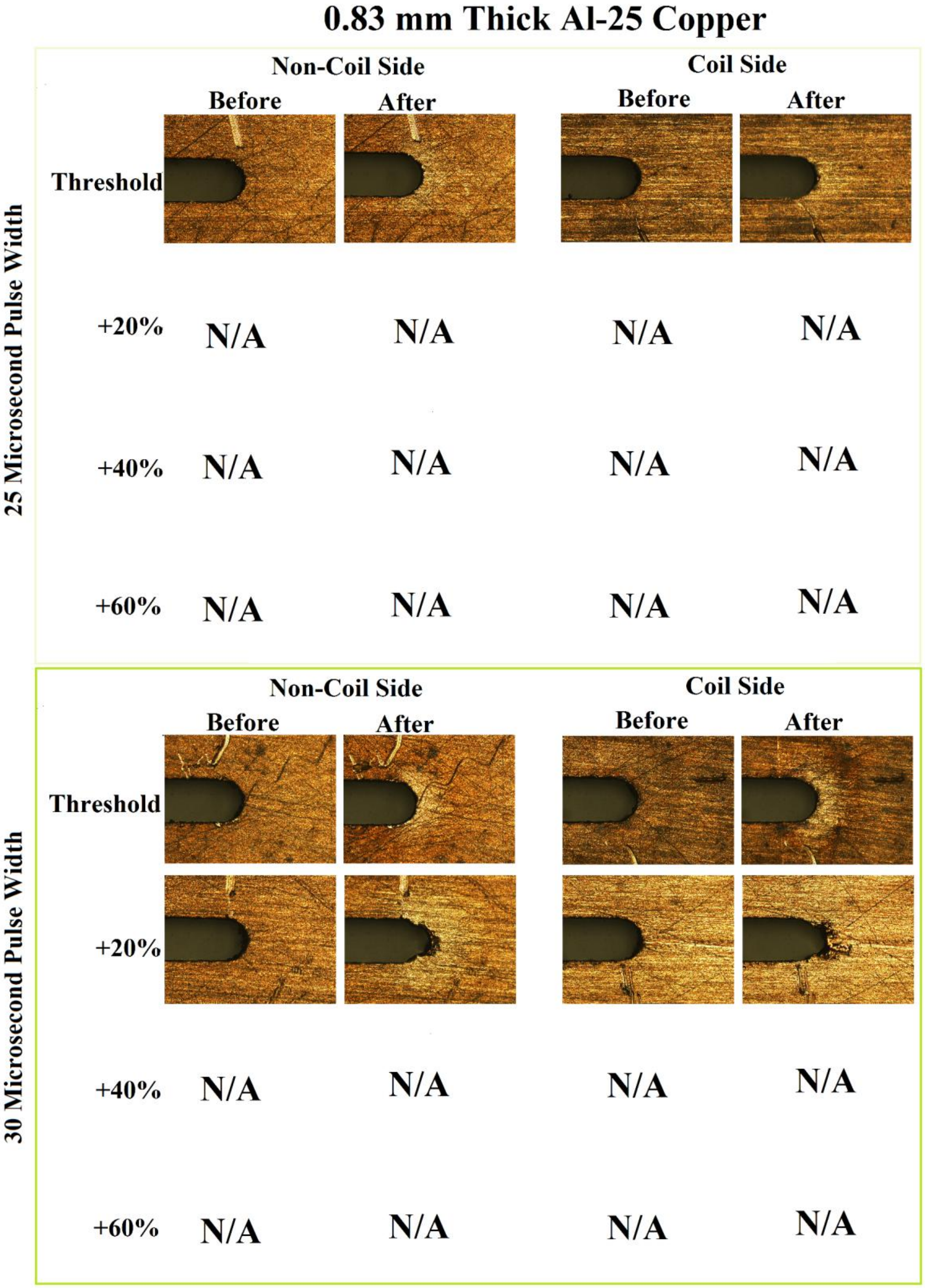

Figure 4.22. The photomicrograph results for 0.83 mm thick Al-25 copper.

4.4.2 ONSET SIMULATION RESULTS

As described in section 2.2.3, the conditions of each of the threshold experiments were modeled using Maxwell 3D to obtain the heating and pressures at the cut tips. The results of these simulations are shown in Tables 4.5–4.7. Tables 4.5 and 4.6 show the results from the 6061 T6 aluminum experiments and Al-25 copper experiments, respectively, in terms of energy/volume, power/volume, and pressure. Table 4.7 compares the standard deviation, normalized to the average, for the energy, power, and pressure on each side of the cut tip.

Table 4.5. The energy, power, and pressure at the cut tip for the onset conditions of the experiments using 6061 T6 aluminum plate.

	0.41 mm thick			**0.79 mm thick**			**1.55 mm thick**		
	17 µs	25 µs	30 µs	17 µs	25 µs	30 µs	17 µs	25 µs	30 µs
Energy coil-side (J/mm^3)	2.93	3.43	3.45	3.22	3.58	3.61	N/A	3.22	4.04
Energy non-coil-side (J/mm^3)	2.95	3.41	3.44	3.10	3.48	3.51	N/A	2.85	3.60
Power coil-side (MW/mm^3)	0.335	0.297	0.255	0.383	0.314	0.274	N/A	.361	.329
Power non-coil-side (MW/mm^3)	0.338	0.295	0.254	0.369	0.304	0.266	N/A	0.271	.293
Pressure coil-side (MPa)	19.7	18.7	16.6	26.6	24.0	21.7	N/A	22.9	25.6
Pressure non-coil-side (MPa)	20.0	19.0	16.4	25.5	23.0	21.0	N/A	21.9	24.5

Table 4.6. The energy, power, and pressure at the cut tip for the onset conditions of the experiments using Al-25 copper plate.

	0.36 mm thick			**0.83 mm thick**		
	17 µs	25 µs	30 µs	17 µs	25 µs	30 µs
Energy coil-side (J/mm^3)	4.95	5.04	4.64	N/A	7.37	7.01
Energy non-coil-side (J/mm^3)	4.89	4.89	4.59	N/A	6.71	6.4
Power coil-side (MW/mm^3)	0.604	0.468	0.368	N/A	0.721	0.581
Power non-coil-side (MW/mm^3)	0.600	0.427	0.364	N/A	0.657	0.531
Pressure coil-side (MPa)	65.1	55.3	44.5	N/A	90.2	76.1
Pressure non-coil-side (MPa)	66.0	55.9	45.1	N/A	85.8	72.4

A published energy to begin to melt aluminum value is about 1.7 J/mm^3 while the energy to begin to melt copper is about 4.1 J/mm^3 [18]. Note that these are for the pure metals rather than alloys. The calculated energy deposited at the cut tip in the experiments is significantly greater than published energy to melt in the aluminum case, but the copper results are more mixed. The 0.83 mm thick copper experiments' energies are about double the aluminum results, which is roughly in line with the 2.4 multiple in the published melt energies for the pure elements. The results for thinner copper melts are lower energies than expected when one looks at the total energy deposited. Table 4.7 compares the normalized standard deviation for energy, power, and pressure across all the experiments.

Table 4.7. The standard deviation normalized for the average of the energy, power, and pressure on both sides of the cut tip. These normalized results do not have units.

	6061 T6 Aluminum	Al-25 Copper
Energy coil-side (Standard Deviation/Average)	0.096	0.22
Energy non-coil-side (Standard Deviation/Average)	0.086	0.18
Power coil-side (Standard Deviation/Average)	0.13	0.25
Power non-coil-side (Standard Deviation/Average)	0.13	0.23
Pressure coil-side (Standard Deviation/Average)	0.16	0.27
Pressure non-coil-side (Standard Deviation/Average)	0.14	0.24

The energy lost in the non-coil-side cut tip is the most consistent value in Table 4.7. These results are consistent with melting being the primary mechanism for NCMC. The non-coil side of the cut tip was the side observed when the samples were mounted, which may explain why this side appears to have the most regular results. There is not a large difference between the normalized standard deviation across the categories considered. This is because the energy, power, and pressure all increase as the excitation level increases. The pressures given in these tables were calculated with the 10 μm cube approach described in section 2.2.3 and cannot be directly compared to results that calculated the pressure from different-sized elements because the force is integrated over the volume of the element but only applied to a surface. However, they can be compared to each other.

4.4.3 NUMERICAL MELT-ONLY MODEL RESULTS

The line-current outputs from the Maxwell 3D simulations were used as inputs to the numerical melt-only model. The outputs from the numeral melt-only model were compared to the cut distances measured in the experiments.

A critical input parameter for the numerical melt-only model is the energy required to melt a given volume of the material. There are widely used, published values of this parameter for pure aluminum and copper [18], but not for the alloys that were tested—6061 T6 aluminum and Al-25 copper.

The experimental data falls between the calculated melt-begin and melt-end values for pure aluminum, but it is closer to the melt-end value, as shown in Figure 4.23. One would expect an alloy to melt at a lower energy than a pure material; however, it is unclear if the material must be brought to a fully melted state before it can be removed. The rest of these results use the melt-end value. The purpose of this numerical model is to show plausibility of a melt-dominated model for NCMC rather than be a close empirical fit. A model that attempts to match the data will be explored in the discussion section. As a first approximation Figure 4.23 compares the outputs from the numerical melt-only model using two criteria for the removal of material: (1) the energy to begin to melt aluminum and (2) the energy needed to bring the aluminum to the end of the melt stage.

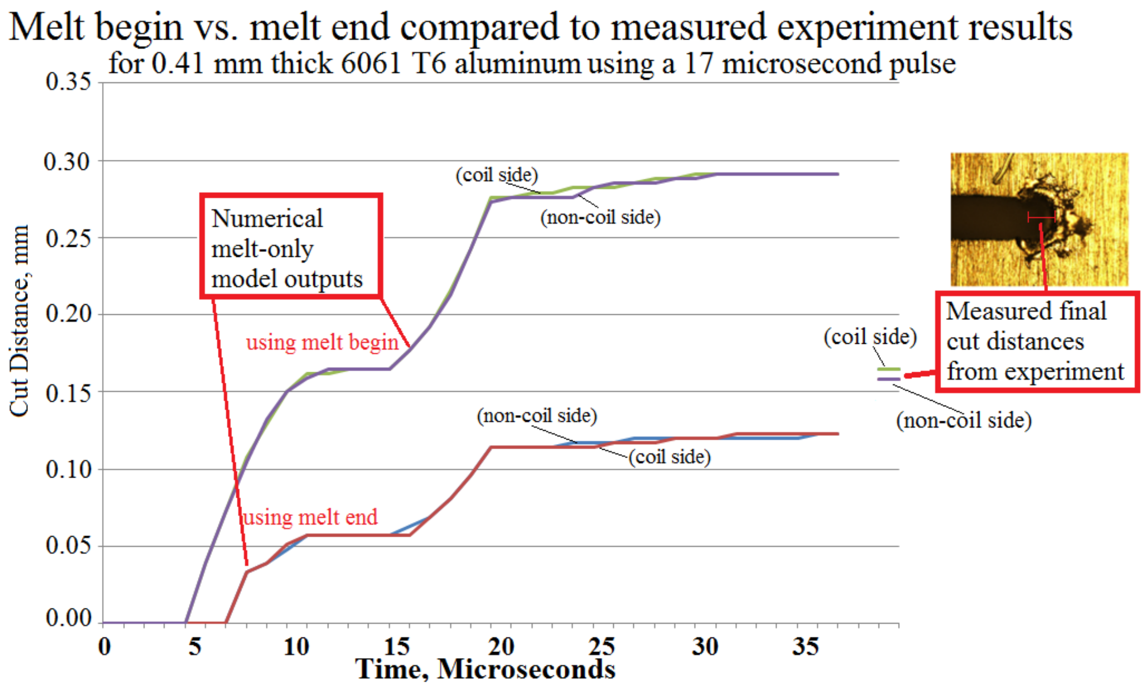

Figure 4.23. The output of the numerical melt-only model using the melt-begin and melt-end parameters as the amount of energy needed to remove material for the T40 case. The measured results are shown on the far right.

Figure 4.23 indicates that using the melt-end value for pure aluminum as the parameter that the numerical melt-only model uses to determine when material should be removed provides a closer match to the experimental data than using the melt-begin value.

The rest of the figures in this section follow the general format of Figure 4.23. The output of the numerical melt-only model is shown as a waveform of the predicted cut distance with respect to time. To the right of this waveform are the cut distances that were measured after the experiment, from the photomicrograph results. While Figure 4.23 shows only the T40 case, Figures 4.24–4.30 show the T40 and T60 cases. The T0 and T20 cases are not shown in order to better show the T40 and T60 cases and because the cut distances were not significant in many cases.

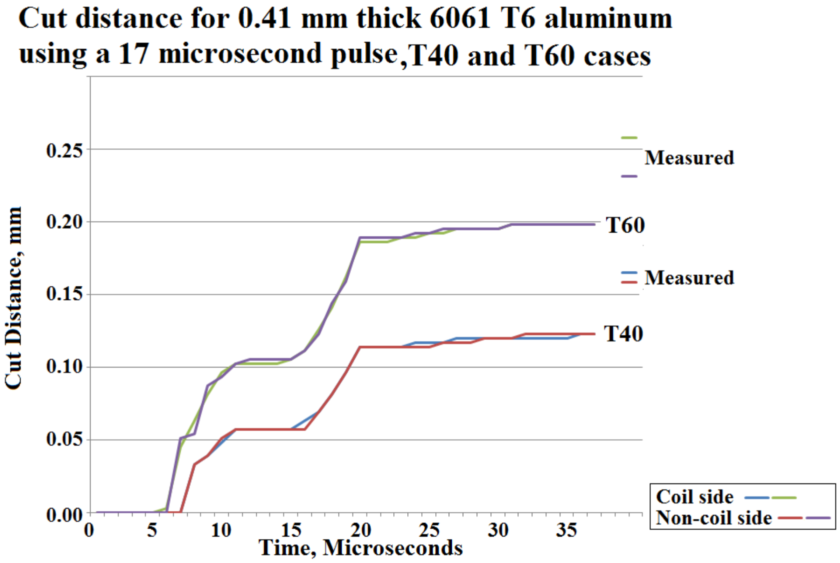

Figure 4.24. The output of the numerical model compared to the measured results for the T40 and T60 cases of 0.41 mm thick 6061 T6 aluminum using a 17 µs pulse. The melt-end value for pure aluminum was used as the material-removal criterion.

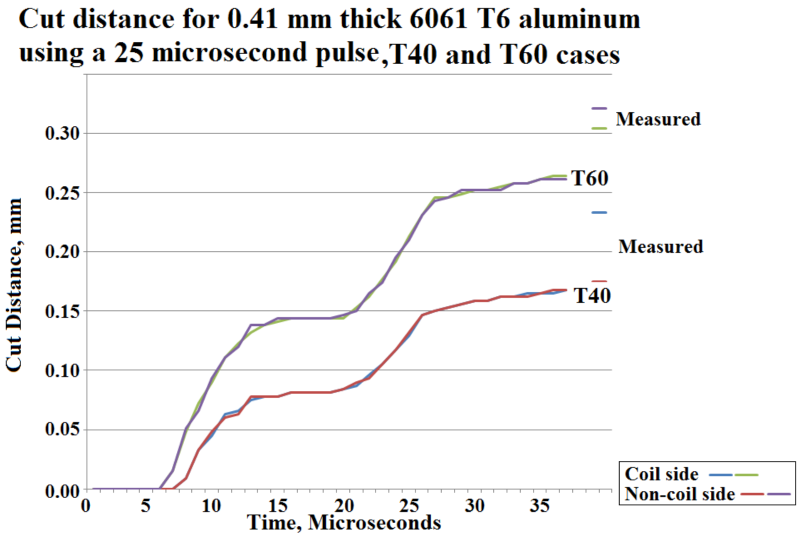

Figure 4.25. The output of the numerical model compared to the measured results for the T40 and T60 cases of 0.41 mm thick 6061 T6 aluminum using a 25 µs pulse. The melt-end value for pure aluminum was used as the material-removal criterion.

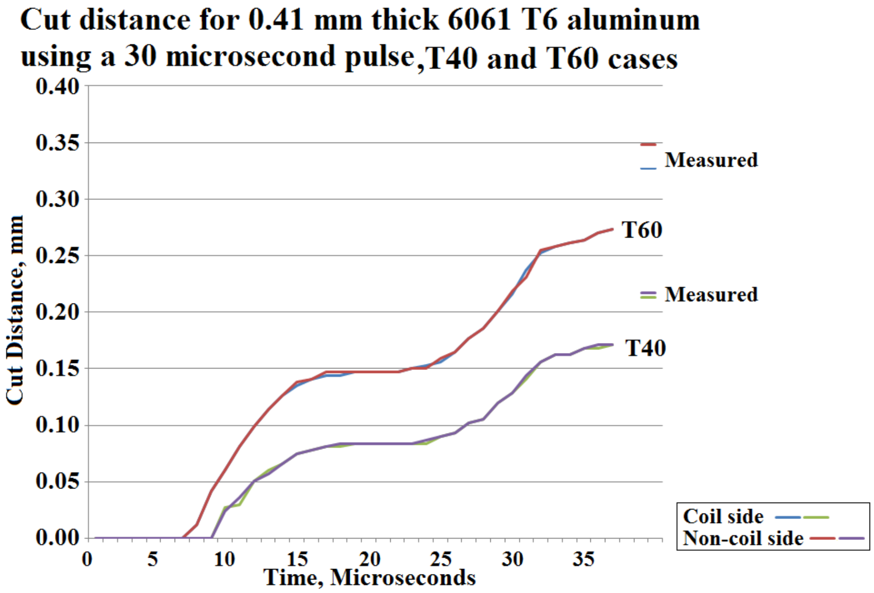

Figure 4.26. The output of the numerical model compared to the measured results for the T40 and T60 cases of 0.41 mm thick 6061 T6 aluminum using a 30 µs pulse. The melt-end value for pure aluminum was used as the material-removal criterion.

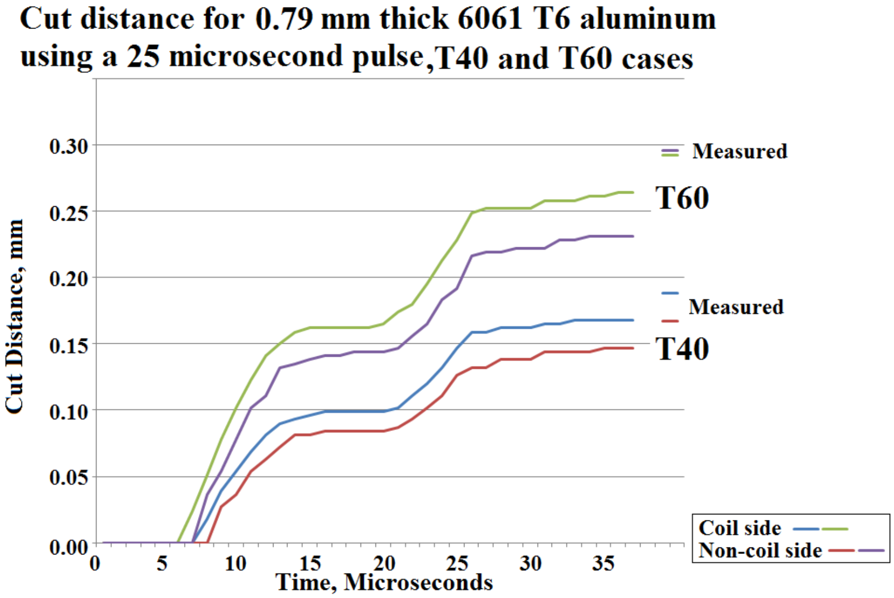

Figure 4.27. The output of the numerical model compared to the measured results for the T40 and T60 cases of 0.79 mm thick 6061 T6 aluminum using a 25 μs pulse. The melt-end value for pure aluminum was used as the material-removal criterion.

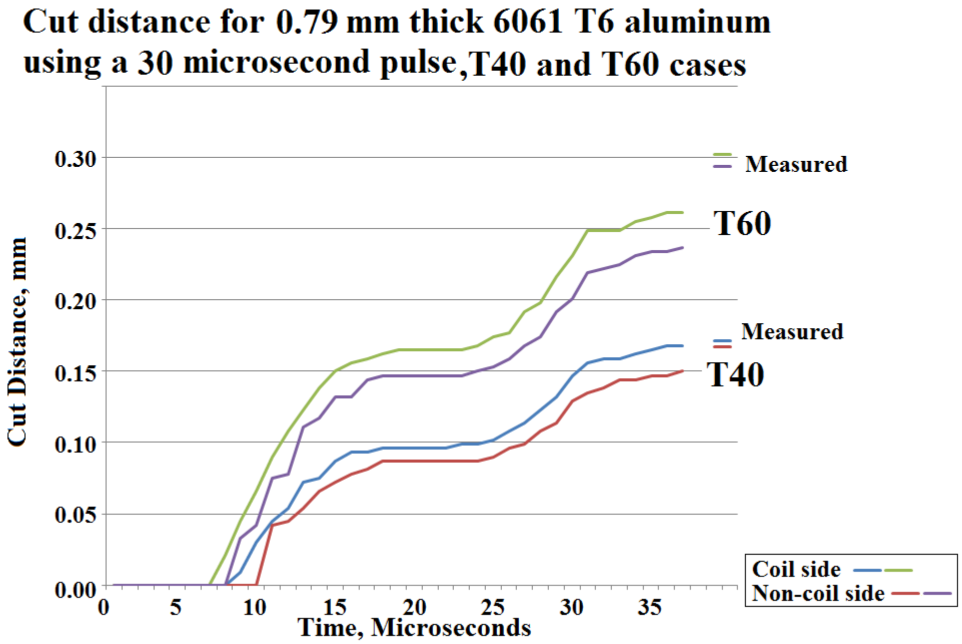

Figure 4.28. The output of the numerical model compared to the measured results for the T40 and T60 cases of 0.79 mm thick 6061 T6 aluminum using a 30 μs pulse. The melt-end value for pure aluminum was used as the material-removal criterion.

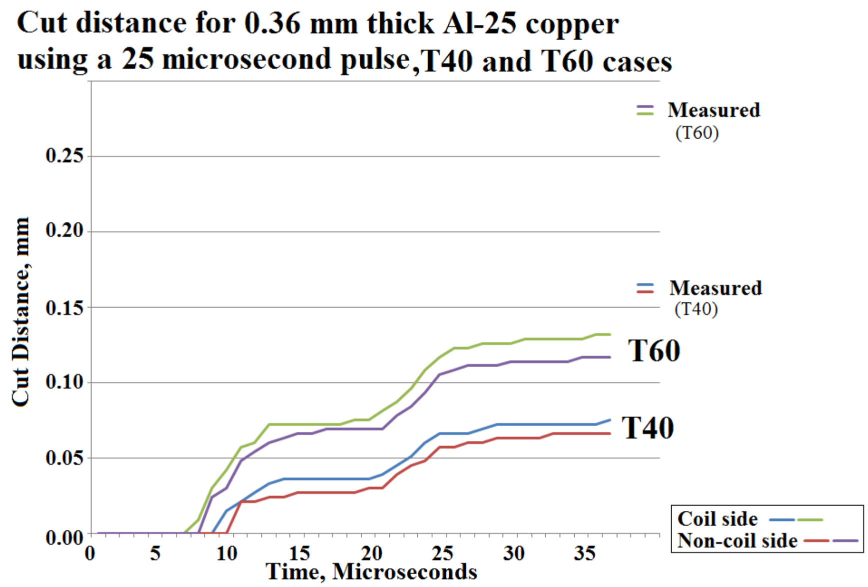

Figure 4.29. The output of the numerical model compared to the measured results for the T40 and T60 cases of 0.36 mm thick Al-25 copper using a 25 µs pulse. The melt-end value for pure aluminum was used as the material-removal criterion.

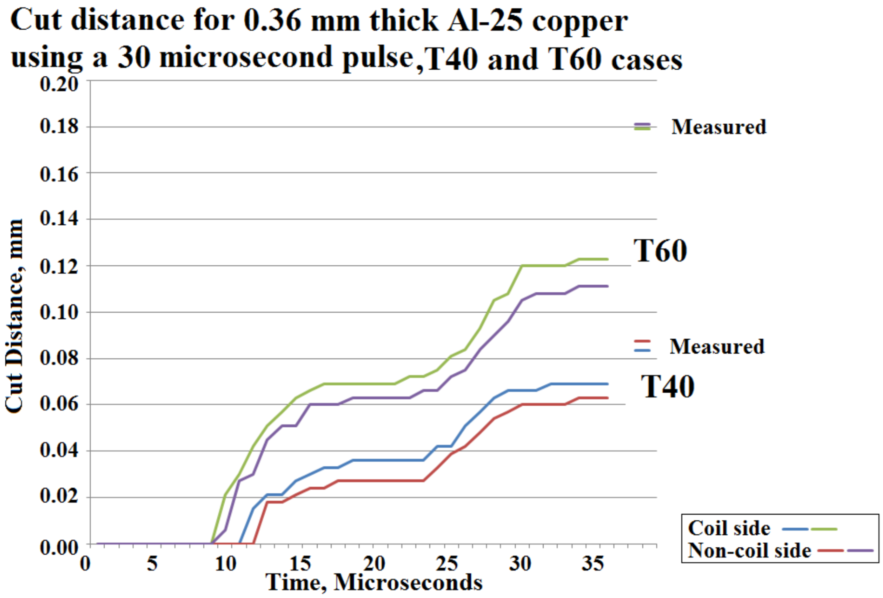

Figure 4.30. The output of the numerical model compared to the measured results for the T40 and T60 cases of 0.36 mm thick Al-25 copper using a 30 µs pulse. The melt-end value for pure aluminum was used as the material-removal criterion.

All of the measured cut distances are greater than the distances calculated by the numerical model in Figures 4.23 through 4.30. This probably indicates that material is removed from the cut front before it is fully melted. The uncertainty of the actual energy to melt the 6061 T6 and Al-25 alloys adds an additional degree of error between the model and the measured values. For the numerical simulations of 0.41 mm thick aluminum, the coil-side and non-coil-side cuts proceed at virtually the same rate. However, the copper and thicker aluminum samples show a greater discrepancy between the two sides. This does not appear to be reflected by the measurements from the photomicrographs. One explanation for this discrepancy is that the numerical model does not include temperature-dependent resistivity, which would force a more even current distribution between the two sides.

4.5 Printed Circuit Board Experiments Results

The primary objective of the PCB experiments is to show how the geometry of the cut tip affects the onset of cutting. As in section 4.4, the experiment can be considered in two parts. The first finds the onset conditions for the three geometries tested and compares these results in table form. The second part examines how the cuts propagate when excitations above the threshold value are applied. The end result is a plot where the experimental results are compared to the output of the numerical melt-only model.

The results of the PCB experiments are given in this section, as are the results of a code-validation simulation and two sets of simulation results that model the experiments. The direct results are photomicrographs of the samples from which cut-distance measurement were taken. The first set of simulation results is from experimental conditions modeled with a finite element code, as described in 2.2.3. Outputs from this set of simulations were used to exercise the numerical melt-only model. The second set of simulation results shows the outputs of the numerical melt-only model, which are compared to the measurements taken from the photomicrographs.

4.5.1 PHOTOMICROGRAPHS RESULTS FOR PRINTED CIRCUIT BOARD EXPERIMENTS

The results of the experiments are shown in Figure 4.31.

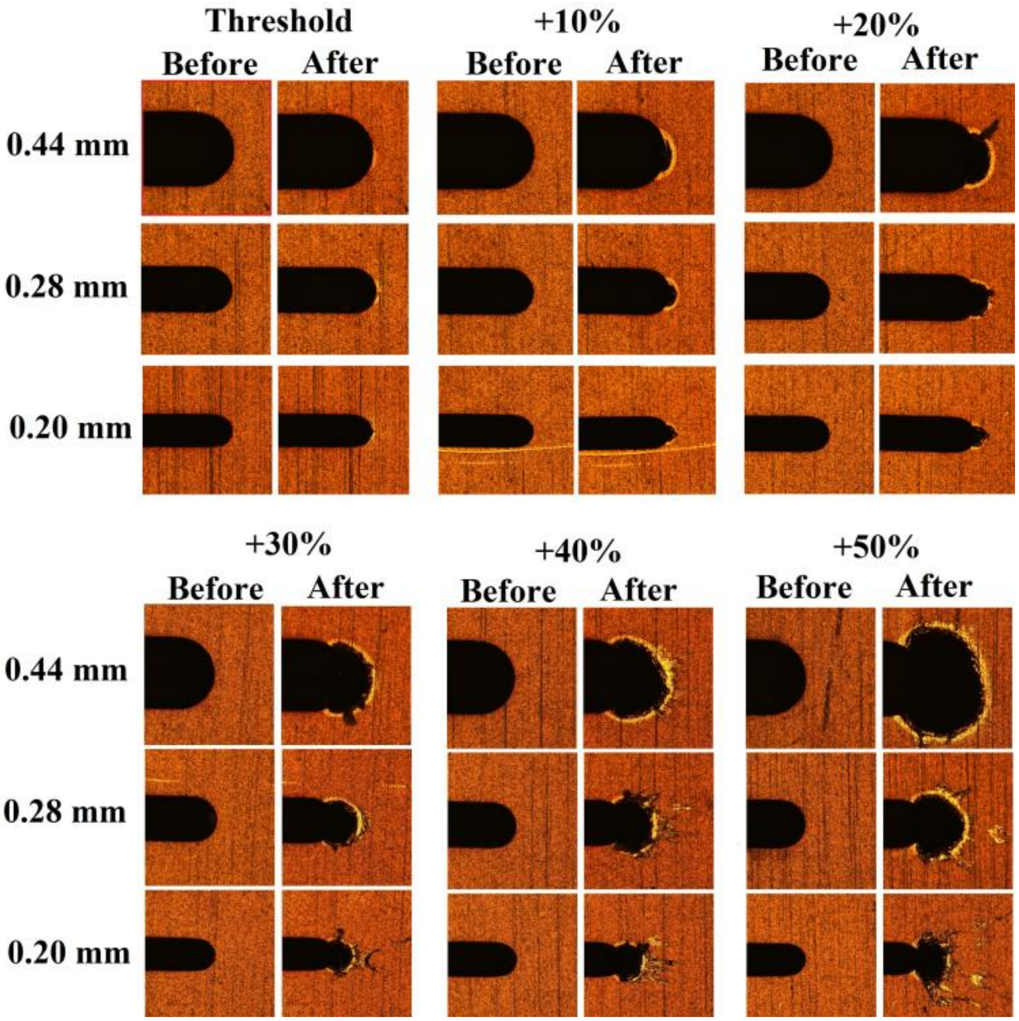

Figure 4.31. Experimental results for three different kerf thickness and six levels of current applied to the samples, ranging from the threshold for cutting to approximately 1.5 times the threshold current. All these photographs were taken with a 10× optical microscope.

As expected, lower currents are required to cut samples with smaller feature sizes. No bifurcations were observed in any of the tests. The geometry for the experiments was modeled and simulated using current waveforms calculated from Rogowski coil signals measured in the experiments using a 12-bit digitizer.

4.5.2 Results from Simulation Validation using B-Dot Coils

PCB technology allowed highly dimensionally accurate B-dot sensors to be built into the samples. These coils were used to validate the simulation results. The B-dot coils were also modeled in the FEA code, and the voltage induced in the coils was compared between simulations and experiments. Figure 4.32 shows the result of one of these comparisons.

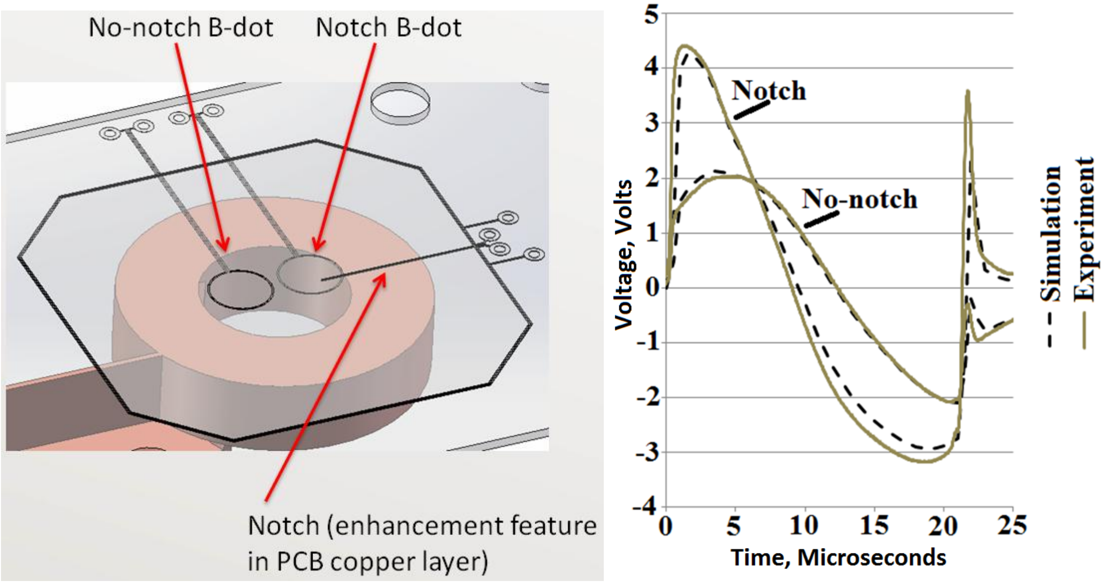

Figure 4.32. Comparison of the voltages induced in the two B-dot loops for an experiment and a 3D transient FEA simulation of the experiment.

The agreement between the simulations and experiments was very good, which suggests that the modeling approach is valid.

4.5.3 FINITE ELEMENT ANALYSIS OF PRINTED CIRCUIT BOARD EXPERIMENTS

FEA simulations were run for each of the cases shown in the experimental results section. Table 4.8 shows reduced results from the simulations of the threshold condition.

Table. 4.8. Reduced data from the simulations of the threshold cases are shown below. All the values computed below were measured at the 10 µm cube that is shown in Figure 4.15.

	Feature Kerf		
	0.20 mm	**0.28 mm**	**0.44 mm**
Energy (J/mm^3)	6.76	6.59	6.28
Peak Power (kW/mm^3)	620	610	590
Peak B (T)	5.86	6.03	6.39
Peak Pressure (MPa)	10	11	11
Impulse (µN*s)	0.011	0.011	0.012
Peak Excitation Current (A)	1050	1200	1420
(Excitation Current)^2/ Radius (MA^2/mm)	5.51	5.14	4.58

Using previously published energy-to-melt values [18], it takes about 4.1 µJ to begin to melt and 5.9 µJ of energy to fully melt a 10 µm cube of copper. The threshold values of Table 4.8 are just above this value. This result is consistent with a melt-dominant mechanism.

Comparing the values in the Peak Excitation Current row shows that, as the feature kerfs are increased, greater excitation currents are needed to cause the onset of cutting. This is probably because the larger kerfs do not cause as much enhancement of the current density at the cut tip as the smaller kerfs do. The excitation energy that causes the onset of cutting appears to scale directly with the kerf width of the enhancement feature. The last row of Table 4.8 compares this relation across the three kerfs tested. This is an important result as it suggests that the energy efficiency of the NCMC approach could be improved if the size of blowholes can be reduced.

4.5.4 NUMERICAL MELT-ONLY MODEL OF PRINTED CIRCUIT BOARD EXPERIMENTS

As described in section 2.2.3, a line-current density was saved at each time step of the FEA simulation. These line-current densities were input to a numerical version of the melt-only analytical model, as described in section 2.1.1. The outputs of the numerical melt-only model for the threshold plus 20% 30%, 40%, and 50% cases are shown in Figure 4.33.

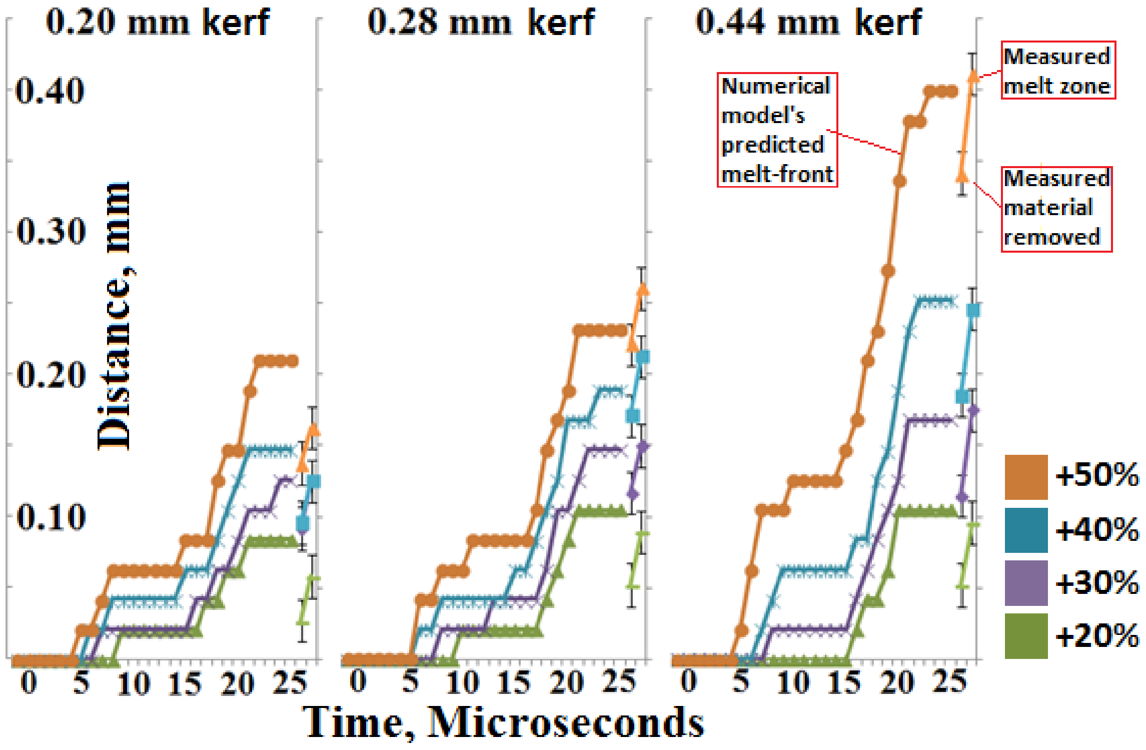

Figure 4.33. The cut distances computed by the 1D analytical model for all cases except the threshold and threshold + 10%. Immediately to the right of the computed cut-distance plots are the measured results for the measured distance that material was removed (lower value) as well as the measured distance to the end of the melted area (higher value).

The 1D numerical model generally over-predicts the cut distance, with the 0.20 mm kerf cases being the worst. One explanation for this is that the model assumes that all melted material is ejected; the model may need to be expanded to consider the pressures on molten material. The pressures for the wider-kerf and higher-energy cases are higher; if the ejection process only occurs above some minimum pressure, these higher-pressure cases will eject a greater percentage of their molten material, which is consistent with the results of these experiments.

4.5.5 Remark on Bifurcations in Printed Circuit Board Experiments

None of the photomicrographs in Figure 4.31 show signs of bifurcations, even at 50% greater charge voltages than the onset condition. In section 4.2.1 bifurcations were observed within 40% of the charge voltage that produced onset for 0.79 mm thick 6061 T6 aluminum. One may conclude that the PCB samples do not bifucate, but rather make larger blowholes as the excitation is increased. Additional experiments were performed to investigate bifurcations with the PCB samples. The excitation current was increased to double the threshold current and applied to a new PCB sample, which did not bifucate. Figure 4.34 shows a photomicrograph of this experiment as well as a lower-excitation multiple-pulse experiment that did develop a bifucation.

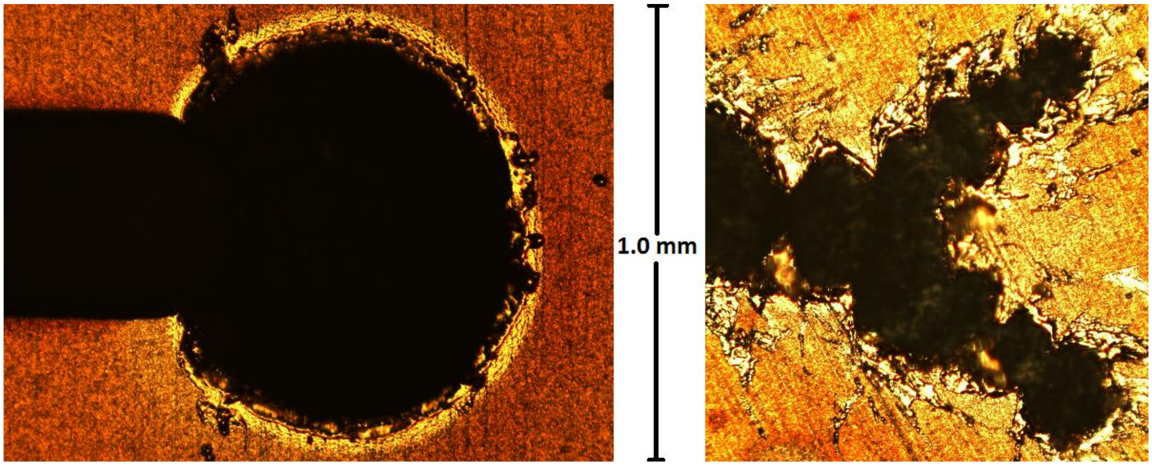

Figure 4.34. Photomicrographs of a double-threshold excitation experiment (using a 0.44 mm kerf PCB sample) that produced only a large blowhole and a multiple-pulse experiment at a far lower excitation level (900 V vs. 1350 V) that produced a bifurcation.

One explanation for the above results is that if bifurcations result from multiple initiation points, it is possible that the PCB surface is too smooth to develop multiple initiation points. The plating process that constructs the copper on PCBs results in a surface that is much smoother than EDM cuts or NCMC-produced blowholes. This theory will be expanded in the discussion section.

CHAPTER 5. DISCUSSION

This chapter provides a description of the NCMC process. It begins with a general model for cutting onset considering only the area in the immediate vicinity of the cut tip. This general model will be used to develop two criteria for the onset of cutting, the second of three objectives of this dissertation. Three additional findings from this research are also discussed here. This chapter concludes by discussing the limitations and exceptions to the models and analysis.

5.1 Cutting Onset

Based on the research described in this dissertation, observed magnetic saw cutting can be thought of as the localized melting and ejection of material due to the concentration of current for a sufficient time for melting and ejection to occur. Though transient magnetic diffusion affects current distribution at the cut tip, the current density in the vicinity of the cut tip is largely determined by the geometry of the cut tip itself, at least in the cases studied here. Both the point of highest current density and the gradient in current density near the cut tip are important in determining the conditions for onset.

In the case of an infinitely large starting feature (effectively a slab without a starter cut), the front face of the entire sample would melt at essentially the same time. However, as the feature size is reduced to the sub-millimeter radii that were studied, the gradient in current density at the feature becomes significant, and new behaviors such as the magnetic saw effect are observed.

5.1.1 A MODEL FOR THE ONSET OF CUTTING

This section will explore the dominant mechanisms for the onset of cutting. The objective is to provide a useful framework for understanding the magnetic saw effect itself, without the complexities of NCMC such as interactions between the coil and sample. The source will be a prescribed current density in the area of the cut tip rather than the current applied to the coil. The reason for making this simplification is that there is not a one-to-one correspondence between the coil current and the current density at the cut tip; many factors, especially feature size, alter this relationship. Coil-sample interactions will be explored in more detail in section 5.3.

Figure 5.1 illustrates a model for the onset of cutting, based on the experimental evidence that the dominant mechanism is melting and ejection of liquid metal.

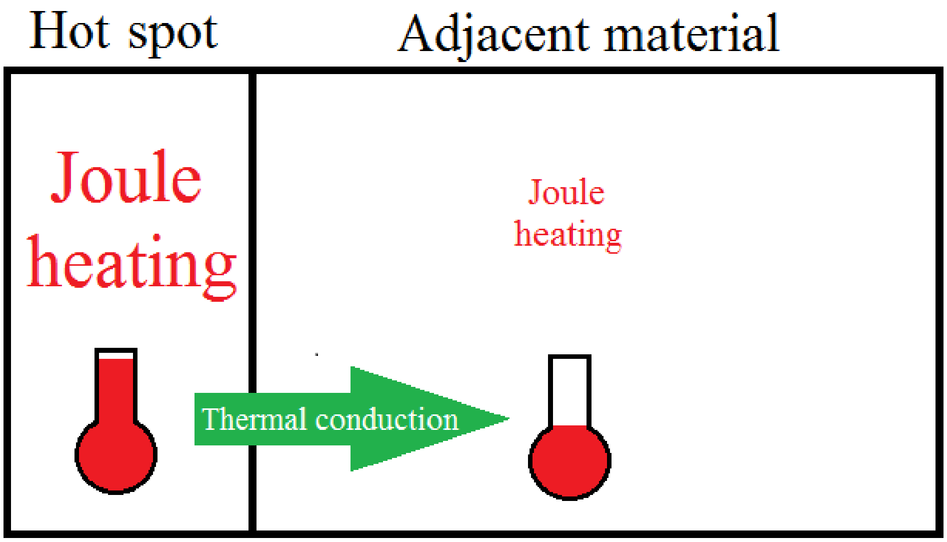

Figure 5.1. A simple schematic representation of the general model for onset. The model assumes a hot spot with a high degree of Joule heating, an adjacent zone with less volumetric heating, and transfer of energy from the hot spot to the adjacent zone through thermal conduction. The relative magnitude of Joule heating and conduction is one way of classifying the operating regime.

The starter feature accentuates a gradient in current density at the cut tip. This enhanced gradient results in a hot spot since the cut tip is being heated faster than the surrounding material. Thermal conduction draws heat away from the hot spot to the surrounding bulk material; this effect may or may not be significant depending on the nature of the cut tip and the applied current pulse. For onset to occur, two criteria must be met:

1) Joule heating at the hot spot must be greater than the thermal conduction to the bulk material.
2) Thermal energy must be applied to the hot spot for long enough to bring the hot spot to its melting point.

These requirements provide two perspectives for understanding the onset of cutting. Depending on conditions, one of these will be the primary consideration. For conditions where volumetric heating overwhelms thermal conduction for the majority of the pulse, it makes the most sense to think about the onset of cutting from an accumulated-energy standpoint, with thermal conduction acting as a minor loss mechanism. The experiments of chapters 4 and 5 suggest that calculating the energy at the cut tip without heat conduction does a reasonably good job of predicting onset and cut distance. However, there are cases—such as long or multiple pulses—where an adiabatic energy assumption would lead to erroneous results. The calculated energy dissipated at the cut tip may be well above the melting point, but the current density for the majority of the pulses is too low to overcome thermal diffusion. Therefore, the material at the cut tip is near its melt temperature, but the incoming power is too low for onset to occur. In these cases, it makes more sense to consider a current-density threshold (rather than an accumulated-energy threshold) above which onset occurs. The experiments discussed in this dissertation did not directly explore this operating regime, but some insight can be gained by considering the role of thermal diffusion in these experiments.

Figure 5.2 shows a more detailed, graphical representation of this onset model, which is the basis for the numerical melt model with thermal conduction discussed in Chapter 2.

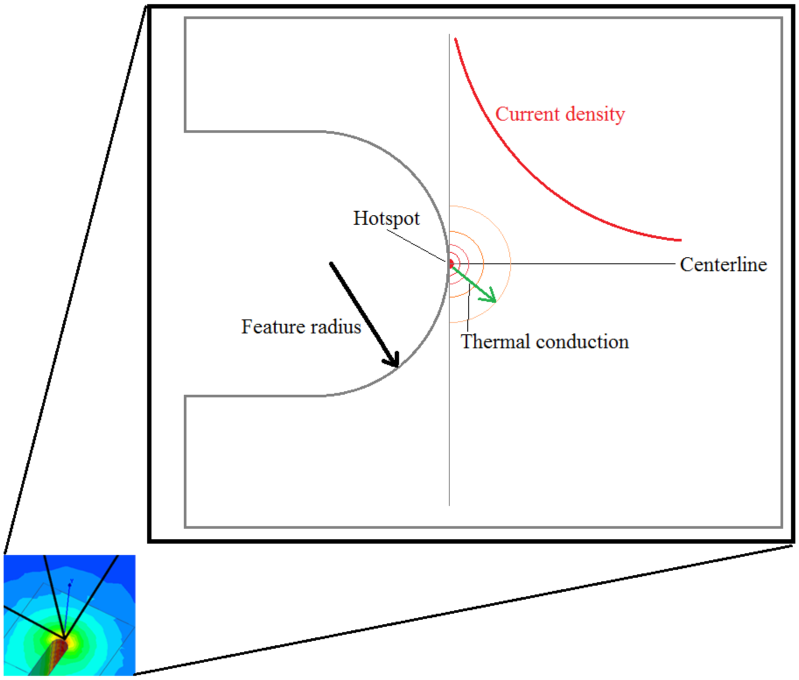

Figure 5.2. A graphical representation for the onset model.

In Figure 5.2, a current density is applied to the area around the cut tip. For the material along the centerline, the current density generally follows the resistive-only model described in Appendix B. The hot spot is material at the point of highest current density. The temperature of the hot spot and the material in its immediate vicinity determine the thermal conduction losses. Once the hot spot reaches its melting point, its temperature no longer rises, although energy is still being added to overcome the latent heat of the material. At this point the thermal gradient at the hot spot decreases and the greatest thermal gradient is moved out to new material. This section will focus on the time interval during which the hot spot reaches its melting temperature.

The role of thermal conduction using the numerical melt model described in section 2.1.4 is described here, along with the results of the PCB and 0.36 mm thick copper Al-25 plate experiments. The PCB and copper plate experiments were selected as examples because they use a similar material but involve different independent variables. The PCB experiments used three different kerfs and an excitation with the same pulse duration for each kerf. The 0.36 mm thick copper Al-25 experiments used three different duration pulses but the same kerf for each. Figure 5.3 compares the ratio of power from Joule heating to thermal conduction at the hot spot for both sets of experiments; this will be referred to as the power ratio.

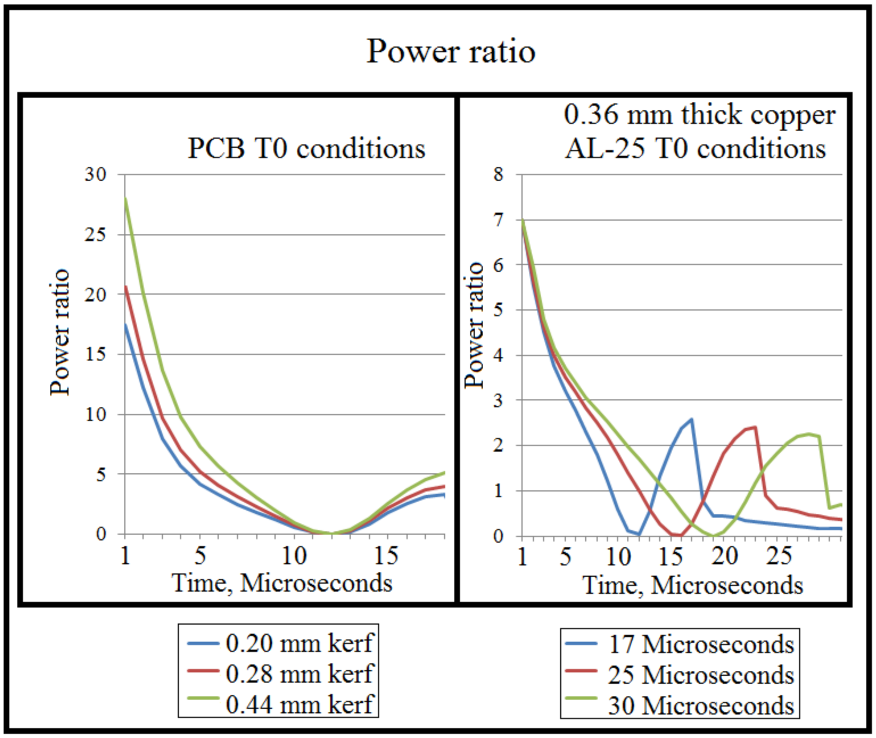

Figure 5.3. The power ratio (ratio of power generated at the hot spot divided by the power flow out of the hot spot by thermal conduction) for the T0 conditions of the PCB and copper Al-25 plate experiments.

Figure 5.3 shows that the feature size largely determines the ratio of power generation to thermal conduction. For the PCB cases, the three different kerfs show three different magnitudes, with the smallest kerf (0.20 mm) showing the lowest power ratio due to the higher thermal gradients that the smaller feature produces. The three different pulse durations of the copper plate experiments show roughly the same power ratio even though the excitation magnitudes are quite different.

From these power ratio plots, it appears that the feature size is more important than the pulse length in determining the thermal gradients at the cut tip. This provides further support for resistive-only current distribution, at least in this regime.

It should be noted that the power ratio varies considerably during the pulses. This effect is better appreciated after examining the current densities in each case; these are shown in Figure 5.4.

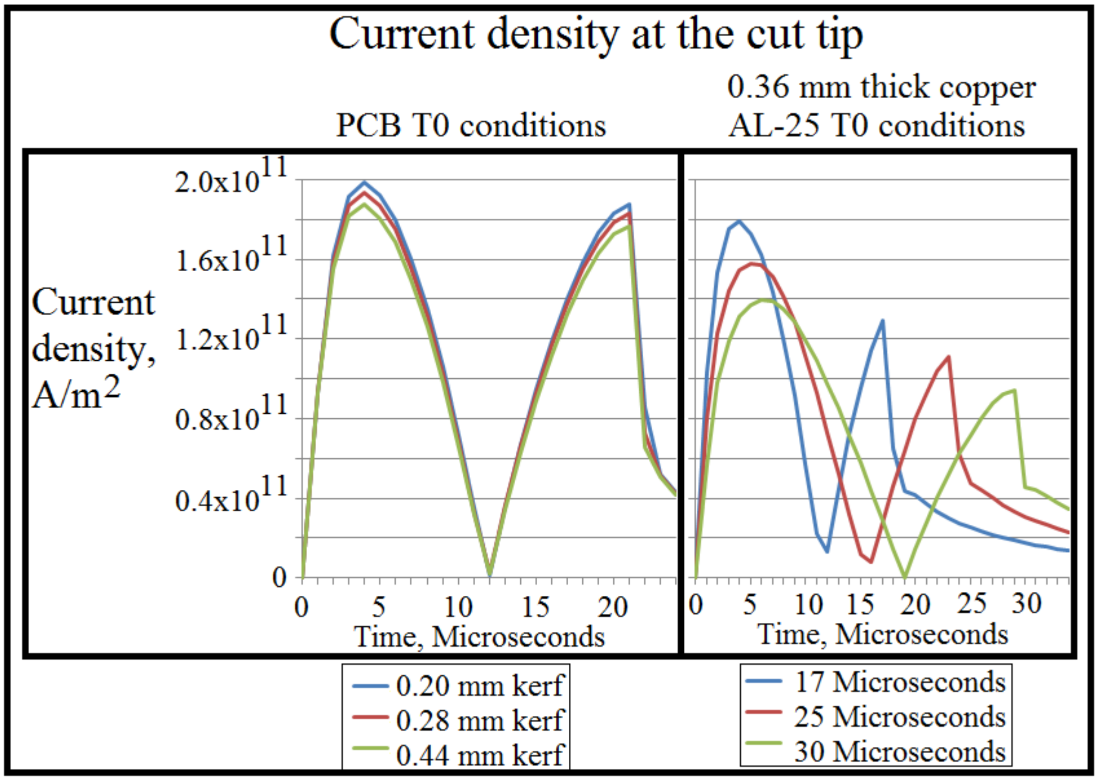

Figure 5.4. The current densities at the cut tip for the T0 conditions of the PCB and copper Al-25 plate experiments.

Although the hot spot's two heating periods are roughly equal in the PCB cases, the power ratio during the first is considerably greater than during the second. This is largely because the higher temperatures during the second heating period cause greater heat conduction away from the hot spot. The copper plate results show a similar effect where the power ratio at the end of the pulse is considerably reduced, even accounting for the lower magnitude of the current density in the second part of the pulse.

One might think that the current density could be used to determine a characteristic thermal gradient for a given feature size. By assuming that the hot spot is at its melting temperature, one could deduce a critical current density in terms of only material properties and feature geometry. However, the time dependence of the heating near the cut tip adds an additional degree of complexity that can affect thermal gradients.

The numerical melt model with thermal conduction can be used to calculate a time-dependent, critical current density for which the heating and thermal conduction are equal. For each time step, the code calculates the power lost from the first element due to thermal conduction, and then it computes a current density that would generate resistive losses at that rate. The results for the three kerfs of the PCB experiments and the three waveforms for the copper plate experiments show how the critical currents vary across these parameters. Figure 5.5 shows the calculated critical current densities for the T0 conditions of the PCB and copper plate experiments.

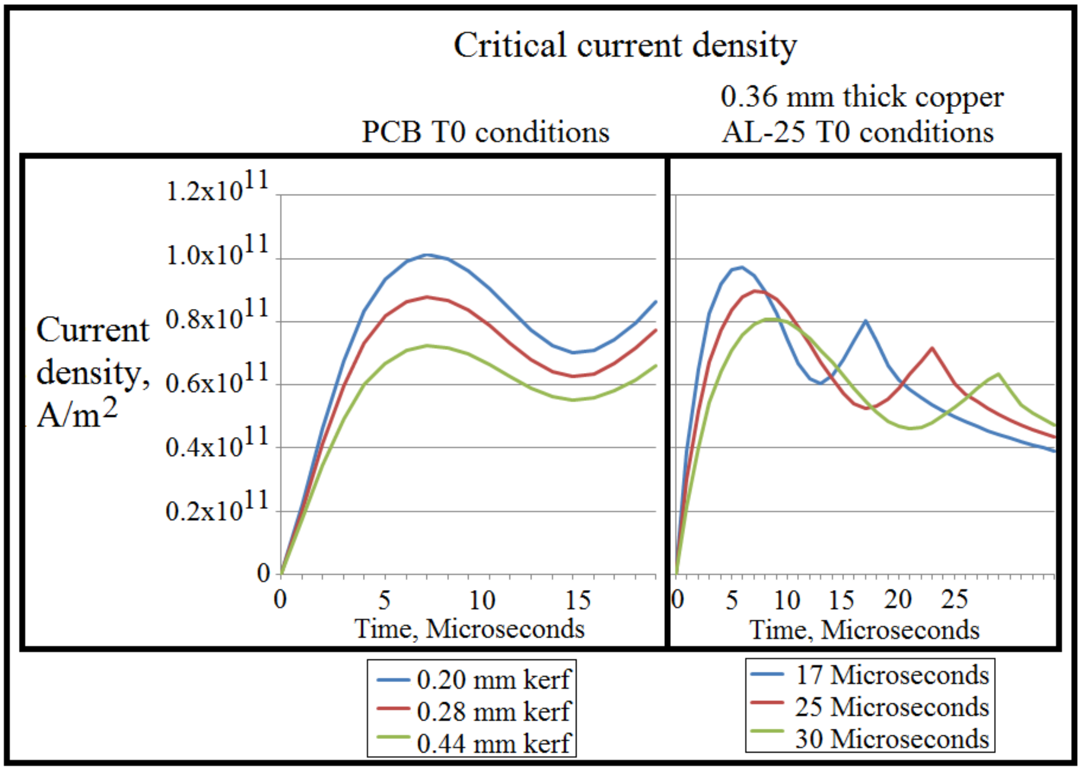

Figure 5.5. The calculated critical current densities for the T0 conditions of the PCB and copper plate experiments.

The critical current densities increase during the first part of the pulse. This is to be expected, as thermal conduction will be low for low initial temperatures. Then the critical current appears to dip as the excitation decreases. The dip can be explained as thermal diffusion increasing the temperature of the material surrounding the hot spot, effectively decreasing the thermal gradients. As the current density increases a second time, the calculated critical current rises again. However, since the material near the hot spot is at a greater temperature at this point in time, the thermal diffusion out from the hot spot is diminished. As a result, the critical current for the second part of the excitation is less than the first even though the temperature at the hot spot is greater at this time.

Although the critical current density is not constant during the pulses, one can still approximate an average value given a material, feature size, and excitation. The results for the aluminum samples are similar to those for the copper samples but roughly half the magnitude. Table 5.1 summarizes the critical currents and energy to melt computed from the experiments in this dissertation; the full results are given in Appendix C. These values assume that a single pulse of 15–30 μs duration is applied to a sample at room temperature using a feature size in the range of 0.33 mm.

Table 5.1. The average energy required for onset and the computed critical current densities.

	6061 T6 Aluminum	**AL-25 Copper**	**Copper (PCB)**
Average energy to onset (J/mm^3)	3.4	5.7	6.5
Average critical current density (A/m^2)	4.8×10^{10}	1.0×10^{11}	8.7×10^{10}

Rows 1 and 2 in the table correspond to the two criteria for the onset of cutting that were presented at the beginning of this subsection. The computed energy values are between the energy to melt-begin and melt-end values published in [18]. There is no direct evidence regarding at what point (between the beginning and end of melt) material begins to be removed. In Chapter 4, material was assumed to be removed at the end of melt, and this criterion matched experimental data reasonably well. However, it is probably the case that material begins to be removed at an earlier point; neglecting thermal conduction and using an end-of-melt removal criterion canceled each other to some degree.

5.1.2 DISCUSSION ON THE ONSET OF CUTTING

For the experiments conducted in the course of this research, the onset of cutting is best understood from an energy perspective. For the pulses used, the calculated critical current densities are easily exceeded if the energy criterion is met. The energy lost from the hot spot is on the order of 10–20% for these cases, meaning that generation significantly exceeds the primary loss mechanism (thermal conduction).

There are cases where it may make more sense to think about the onset of cutting from a power perspective. For example, if multiple pulses of a lower magnitude are applied to a sample, the thermal conduction may be high enough to prevent onset for all but the peaks of the waveforms. These cases are similar to the view and experimental setup described by Gallo [16]. The current density gradient of the direct-drive systems is low than for an NCMC system, which may explain the lower critical current density reported in [16].

5.2 Three Additional Findings of Note

This section discusses three additional findings from this research. The first is that resistive (rather than inductive) effects determine the current distribution in the area immediately around the cut tip for the cases studied. Considering only resistive effects greatly simplifies the study of this area.

The second finding is that the energy required to initiate cutting scales in proportion to feature size. This suggests that small feature sizes may be beneficial for efficient cutting.

The final finding is that the current generated in the sample is not affected by what occurs at the cut tip. The significance of this finding is that modeling NCMC can be greatly simplified by (1) first calculating the total current induced into the workpiece and then (2) using these calculated currents to compute the local current densities at the cut tip.

5.2.1 RESISTIVE EFFECTS DOMINATE CURRENT DISTRIBUTION AT THE CUT TIP

A model that calculates the current distribution at the cut tip considering only resistive effects generally matches more inclusive FEA results for the excitations and geometries studied; this shows that resistive effects dominate magnetic effects at the cut tip. The current distribution at the cut tip is important because it largely determines the thermal gradients in the vicinity of the cut. Neglecting inductive effects at the cut tip simplifies the understanding of this area.

A comparison between the resistive-only model of current distribution and FEA results for a single time step of the PCB experiments using three different kerfs is shown in Figure 5.6.

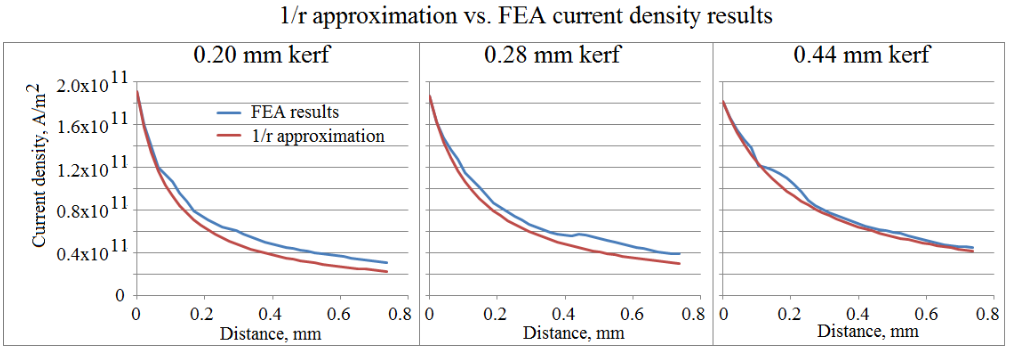

Figure 5.6. The resistive-only model of current distribution is compared with FEA simulations that include both resistive and inductive effects. The plots show the results at a single time step from three of the PCB experiments, each with a different kerf starter feature.

Figure 5.6 considers a single time step during an early portion of the pulse. The current densities during the full pulse follow the trend seen in Figure 5.6; however, there are some time steps where magnetic effects change the gradient in current density to a small degree. Figure 5.7 shows the power dissipated in the ten μm cube divided into four time intervals in the center. Surrounding this are the current distributions for each microsecond for the first quarter millimeter extending from the cut tip.

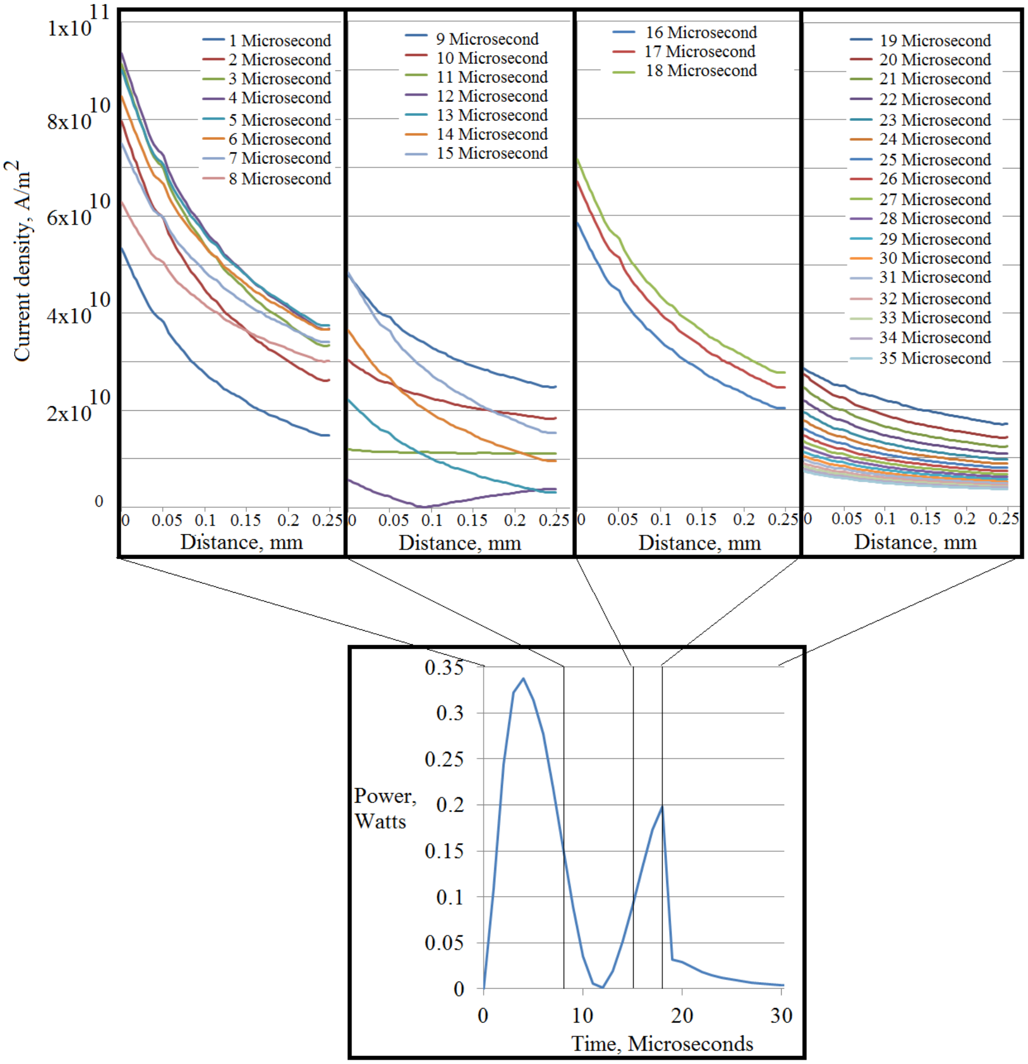

Figure 5.7. The power in the coil-side 10 μm cube and current distribution along the coil-side line for a representative experiment.

The current densities at most of the time steps seen in Figure 5.3 follow the resistive-only model of current distribution closely, especially in the first and third time intervals. The experiment that is the basis of the simulation shown in Figure 5.3 is the T0 condition for 0.41 mm thick 6061 T6 aluminum, but the other experiments show trends similar to those seen in Figure 5.7. Despite the fact that a significant portion of the pulse duration is spent in time intervals two and three, the majority of the heating occurs in time intervals one and two because of the greater current density at the cut tip. Figure 5.8 illustrates this point by showing the predicted and measured cut distance. The vertical lines divide the plot into four time intervals.

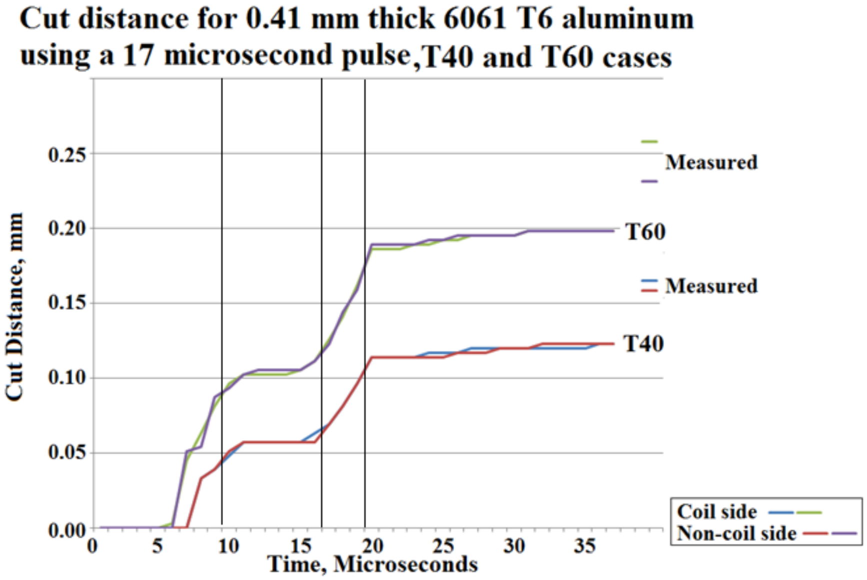

Figure 5.8. The predicted and measured cutting for the 0.41 mm thick 6061 T6 aluminum using 17 μs pulses with the quadrants of Figure 5.7 superimposed. Note that the time intervals have been shifted by one microsecond to account for a delay introduced by the numerical model.

The resistive-only current distribution model predicts that smaller feature sizes will have higher gradients in current density at the cut tip. This suggests that the thermal gradients will be higher for smaller feature sizes as well. Thus, the smaller feature sizes require higher power levels to initiate cutting due to the greater thermal conduction losses. The high thermal gradients that result from the small feature sizes may set a lower bound on the size of a magnetic saw cut and explain why magnetic saw cuts do not seem to initiate from microscopic features alone. Magnetic saw cuts smaller than about 10 μm were not observed.

The resistive-only current-density model is developed in Appendix B. It should be noted that while this model is valid for the pulse widths used in this research, inductive effects become important at shorter pulse widths.

5.2.2 INPUT ENERGY NEEDED TO CUT SCALES WITH FEATURE SIZE

The PCB experiments show that the onset of cutting requires less energy stored in the pulsed-power supply for smaller feature sizes than for larger feature sizes. The PCB experiments explore well-controlled feature sizes with 0.20 mm, 0.28 mm, and 0.44 mm kerfs. Analysis shows that while the conditions at the cut tip are similar for the three kerfs, the excitation currents that produce the onset of cutting are significantly different. The energy that is stored in the pulsed-power supply for each case is proportional to the square of these excitation currents. The results of the PCB experiments indicate that the energy stored in the pulsed-power supply required for onset to occur scales approximately with the feature kerf.

Table 5.2 shows the results from FEA simulations of the conditions that were found to produce the onset of cutting.

Table 5.2. Results from FEA simulations of the PCB T0 conditions.

	Feature Kerf		
	0.20 mm	**0.28 mm**	**0.44 mm**
Energy at cut tip (J/mm^3)	6.76	6.59	6.28
Peak power at cut tip (kW/mm^3)	620	610	590
Peak B (T)	5.86	6.03	6.39
Peak pressure (MPa)	10	11	11
Impulse (µN*s)	0.011	0.011	0.012
Peak Excitation Current (A)	1050	1200	1420
(Excitation Current)^2/Radius (MA^2/mm)	5.51	5.14	4.58

The first five rows of Table 5.2 show that the conditions at the cut tip are quite similar for the three cases. However, the excitation currents required to create these conditions vary considerably; these values are highlighted in red. The excitation energies are proportional to the square of these peak excitation currents. Dividing each of the squares of the peak excitation currents by the associated radii results in values that are approximately constant across the three experiments. This result is highlighted in yellow and shows that the scaling of the excitation energy to feature size is approximately proportional to the feature radius. This finding suggests that significant improvements to the efficiency and the size of the pulsed-power device may be possible if the diameter of the NCMC cuts can be reduced. This is because a smaller-diameter NCMC cut would allow the onset of cutting for the next cut to occur earlier than a larger-diameter cut would. Figure 5.9 plots the stored energy vs. the feature radius for the PCB onset conditions.

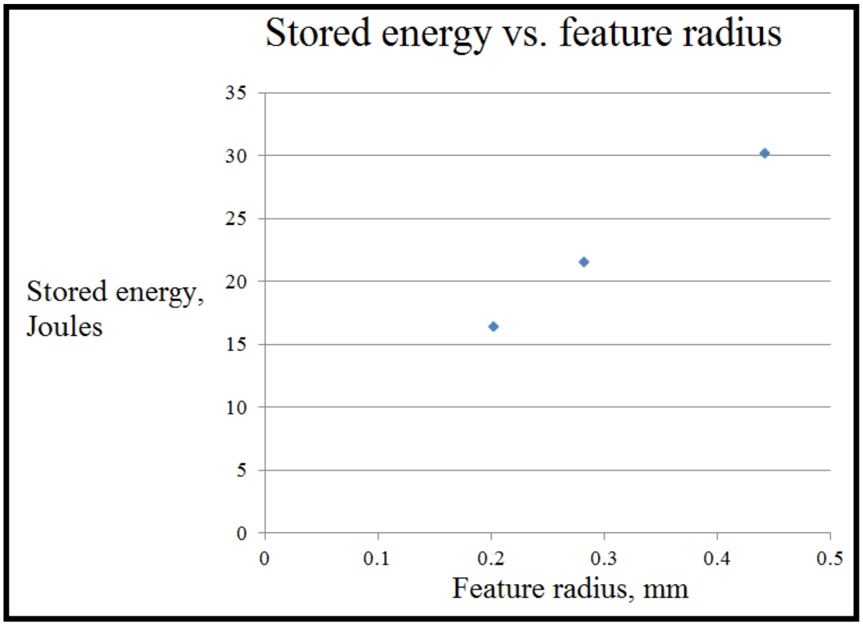

Figure 5.9. The energy stored in the pulsed-power supply compared to the feature radius for the onset conditions of the PCB experiments.

If the trend shown in Figure 5.9 continues, it appears that the energy required for onset could be reduced considerably with feature sizes that are readily achieved with steady-state magnetic saw cuts.

5.2.3 CURRENT GENERATED IN THE SAMPLE NOT AFFECTED BY CUT-TIP CONDITIONS

The cut-tip region is considered to be the area of high current density, about 1 mm in diameter, surrounding the cut-tip. Though the high current densities increase losses in this region, the area is simply too small to measurably influence the overall current flowing in the workpiece. The energy lost in a 1 mm by 1 mm section of a 0.41 mm thick 6061 T6 sample was about 30 times smaller than the energy lost in the rest of the aluminum sample. The best overall efficiency measured using the second-generation system, from stored energy to the energy required to melt the material removed, was about 0.11%. So the actual melt and removal of material is only a tiny fraction of the overall energy consumed. This system was not optimized for efficiency, but even a substantial improvement in the operating efficiency would not decrease the overall energy used by the system enough to make the cutting operation a significant fraction of the total energy.

The significance of this finding is that modeling NCMC operation can be greatly simplified by (1) first calculating the total current induced into the workpiece then (2) using these calculated currents to compute the local current densities at the cut tip. Because the cut-tip region does not influence the overall transformer operation between the sample and coil, it is possible to split the simulation into two parts and add additional effects to the smaller-scale simulation. This approach was used in this work, with Maxwell 3D providing the inputs to the numerical melt model as well as the numerical melt model augmented with thermal conduction. Future research could use an FEA code to compute the induced currents, and then use a second code to modify these values to include such effects as the removal of material, temperature-dependent resistivity, and temperature-dependent thermal conductivity. More detailed analyses of coil-sample interactions are given in Appendix D.

5.3 Limitations of This Research

This section describes several known limitations of this research.

5.3.1 COPPER 110 AND 1100 ALUMINUM

Some soft materials, such as copper 110 and 1100 aluminum, deform before the onset of cutting. Figure 5.10 shows an annealed copper sample that deformed rather than be cut.

Figure 5.10. An annealed copper 110 sample where deformation at the starter notch was observed.

Samples like the one shown in Figure 5.10 were tested at many different excitation levels and none were found to produce normal cutting. It appears that for the case of a 0.33 mm feature kerf, the pressure due to $\boldsymbol{J} \times \boldsymbol{B}$ forces causes the material to yield before melting occurs. The same materials will show the usual results of cutting if the starter feature is narrowed, with a small razor cut, for example. Figure 5.11 shows an example of this using another copper 110 sample of the same type as shown in Figure 5.10.

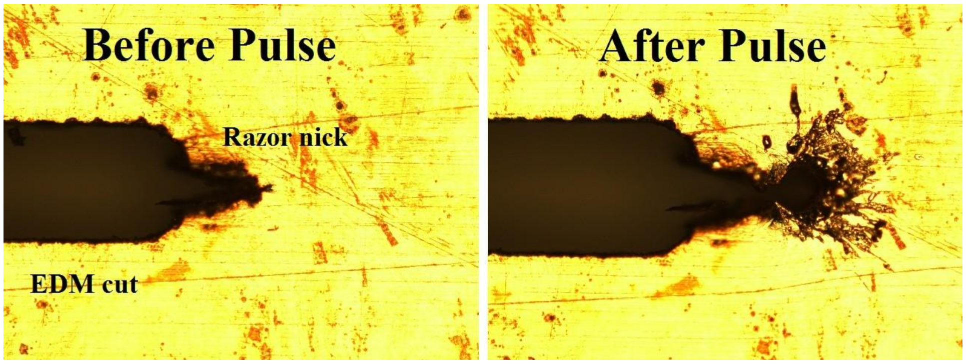

Figure 5.11. An annealed copper 110 sample where the starter feature was enhanced with a razor nick shows the usual melting and cutting rather than the deformation seen in Figure 5.10.

The more pure materials like copper 110 and 1100 aluminum would have been preferable to the alloys that were used for the plate experiments because the higher-purity metals' characteristics are better known and there would be less variation from batch to batch. However, these metals are too soft to be used for experiments that started with an EDM cut because of the deformation issue. If a feature finer than 0.33 mm could be affordably made in a repeatable fashion in the future, the high-purity alloys would make good test samples.

5.3.2 TEMPERATURE-DEPENDENT MATERIAL PROPERTIES

Temperature-dependent electrical resistivity was not considered in this dissertation, largely because the version of Maxwell 3D used for the FEA simulations did not support it. The resistivity of metals such as copper and aluminum changes significantly as they are heated. However, this effect can be considered as part of the melting-and-ejection process and thus is a relatively consistent source of error. The addition of temperature-dependent resistivity in the FEA simulations will decrease the computed current densities at the cut tip, but this is somewhat offset by increased resistivity due to the increased temperature. The lack of temperature-dependent resistivity probably explains why the numerical melt-only model predicts noticeable difference in the cut distances between the coil and non-coil sides for thick samples. Figure 5.12 compares the numerical melt-only model's outputs for two sample thicknesses.

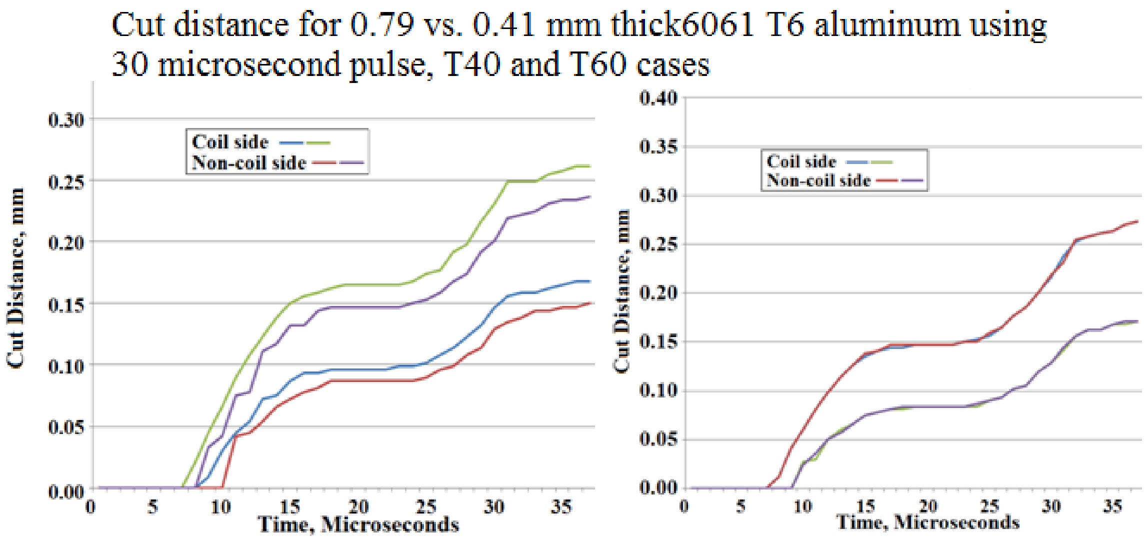

Figure 5.12. The predicted cut distances for 0.79 mm and 0.41 mm thick 6061 T6 aluminum.

Figure 5.12 indicates that as the sample thickness increases, the cut should extend farther on the coil side of the sample; however, this is not observed in experimental results. Including temperature-dependent resistivity would reduce the difference in current density between the coil and non-coil sides and may be sufficient to negate the difference in cut distance between the two sides. However, the discrepancy between the cut distances shown in Figure 5.12 is not large without including this effect.

The thermal conductivity of metals also changes with temperature [21]. For copper and aluminum, the trend is generally that thermal conductivity decreases as temperature increases. If this effect were added, the critical current densities shown in Table 5.1 would decrease.

Temperature-dependent electrical resistivity and thermal conductivity would change the values of the simulation results, but the overall trends should be the same.

These effects are compatible with the onset model described in this chapter; in the future, more sophisticated analysis tools could be used to explore their contributions.

5.4 Efficiency Considerations

This section discusses the efficiency of the NCMC hardware constructed thus far and what may be achievable with future systems.

5.4.1 COMPARISON OF MEASURED ENERGY TO MINIMUM ENERGY TO MELT

Though it is a major advance from the previous system, the overall efficiency of the second-generation NCMC system is still quite low. All the efficiency results are provided in Appendix E. The overall efficiency is taken to be the energy required to melt the amount of material removed divided by the energy stored in the capacitors. The energy required to eject the material is insignificant in comparison to the energy required to melt the material. The greatest efficiency was only 0.11 %, though this value was achieved in two cases. In analyzing the efficiency results, it is clear that larger excitations helped the overall efficiency. This is probably because in all the cases, a significant amount of the energy dissipated at the cut tip is used to bring the material to its melting point; this energy is a lower fraction of the total energy dissipated at the cut tip for the higher excitation cases.

Although higher excitation levels appear to be the better operating mode in these single-pulse tests, they are probably not ideal because higher excitation levels produce larger blowholes, which result in lower enhancement for subsequent cuts and are more likely to bifurcate. A better solution may be to have a pulse train of several lower-amplitude pulses that are close enough in time to prevent excessive cooling. This way, the pulses would still benefit from heat deposited by the previous pulses.

5.4.2 ANALYSIS OF LOSSES

This section analyzes the losses experienced by the second-generation NCMC system during a single pulse and considers what may be possible with future designs. The second-generation NCMC apparatus was designed for laboratory flexibility rather than high efficiency. Figure 5.13 shows the flow of energy during a single pulse.

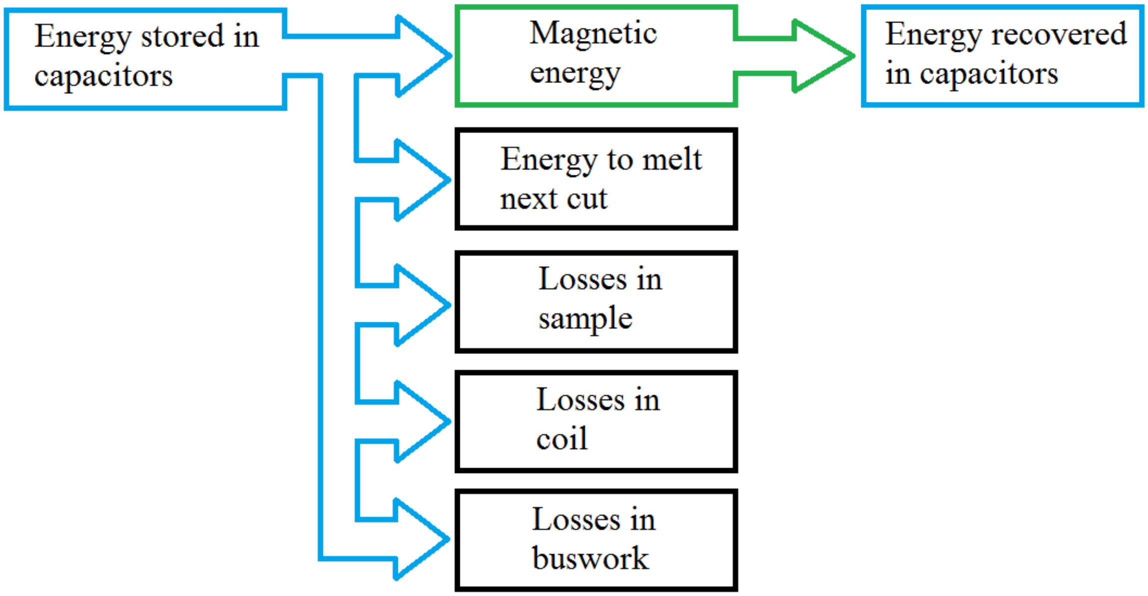

Figure 5.13. A schematic illustration of the flow of energy during a single pulse.

As the capacitors are discharged, a current flows through the coil and charges a second bank of capacitors. The energy stored in the second bank of capacitors could possibly be recovered by a more sophisticated system. The energy that is not reclaimed in these capacitors has been dissipated resistively in some part of the system. The results for the 0.41 mm thick 6061 T6, 30 µs, T60 case are shown in Table 5.3.

Table 5.3. The energy partitioning of the 0.41 mm thick 6061 T6, 30 µs, T60 case. Peak magnetic energy is a transient quantity that does not figure into the energy balance totals at the beginning or end of the pulse.

Energy stored in capacitors	**52.5 J**	**100%**
Peak magnetic energy	12.0 J	(transient)
Energy recovered in capacitors	33.0 J	63%
Resistive losses in coil	3.2 J	6.1%
Resistive losses in sample	5.3 J	10%
Resistive losses in buswork	11.0 J	21%
Energy delivered to cut	0.058 J	0.11%

Table 5.3 shows that the efficiency of the system could be nearly tripled by recovering the energy stored in the second capacitor bank. If resistive losses in the coil and buswork could be reduced, an even larger amount of the initial energy would be recoverable. By adding just energy recovery and lower-resistance buswork, efficiency for the case described could be increased from about 0.11% to about 0.3–0.4%. More radical approaches might be able to increase this further.

5.4.3 REMARKS ON EFFICIENCY

In the course of this research, several concepts for improving efficiency have been considered; however, given the time requirements to construct pulsed-power supplies, none have been tested.

A new type of high *di*/*dt* semiconductor switch may allow for more efficient and compact design while reducing the impulses between the coil and sample. Both generations of test hardware were designed around thyristors that were intended for line-frequency applications. These switches were limited to a maximum *di*/*dt* of about 1 kA/μs and a voltage of about 2 kV. The Silicon Power CCSTA43N40A10 is capable of 25 kA/μs and has a peak operating voltage of 4 kV in a much more compact package. Figure 5.14 compares the two switches presently in use to a single CCSTA43N40A10 that could replace them on a future design.

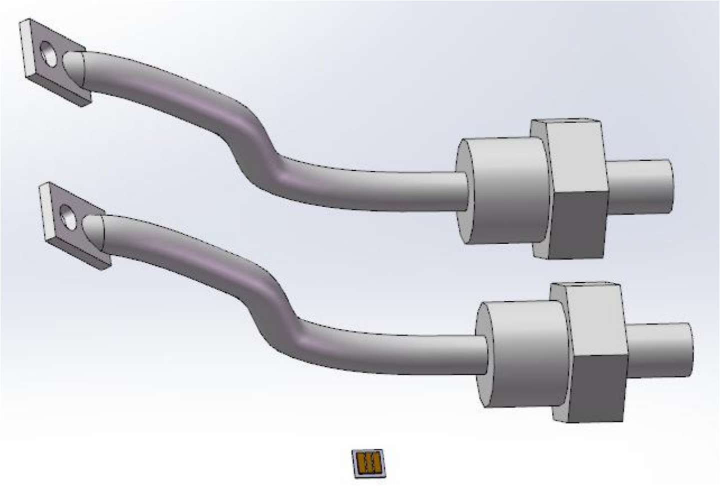

Figure 5.14. A new type of semiconductor switch (bottom) compared to the switches used for the second-generation NCMC system.

Moving to 4kV operation could allow for much shorter pulses, and shorter pulses would decrease the stored energy requirement and conduction losses.

Another way to enhance the system efficiency is to have multiple pulses very close together in time. This would probably require more stored energy to achieve, but having the pulses close together in time would allow the heat deposited in the cut-tip region to be reused. One could generate an additional pulse by discharging the energy stored in the second capacitor bank back through the coil in reverse, thereby immediately reusing the recovered energy.

Pre-heating the samples would lower the stored energy requirements because the material would start at a higher temperature and the thermal conduction between pulses would be lower. During early multi-pulse testing, it was observed that as the sample heated, more material was removed by each cut.

5.5 Comparison to Other Machining Technologies

This section evaluates where the NCMC process may fit with existing technologies. It begins with a comparison of the NCMC process to cutting with a small rotary saw and jigsaw. Then the NCMC process is compared with larger-scale commercial cutting technologies.

5.5.1 COMPARISON OF NCMC TEST HARDWARE TO SMALL COMMERCIAL SAWS

A photograph of two small saws is shown in Figure 5.15.

These two saws were compared to the second-generation NCMC system for cutting a straight line 2.5 cm into a 0.79 mm thick 6061 T6 aluminum samples. Three tests were run with a commercial power meter monitoring the power consumption. The averaged results from these tests are shown in Table 5.4.

Figure 5.15 Two small saws used for model building. These saws can use blades as thin as 0.13 mm and were procured to investigate the possibility of using them to make the starter cuts. A standard size sample can be seen on the radial saw.

Table 5.4. The averaged results from three tests run for both types of saws cutting 2.5 cm into a 0.79 mm thick 6061 T6 aluminum samples.

	Jigsaw	**Radial saw**
Standby power (W)	43	50
Energy to cut 2.5 cm (kJ)	0.75	2.0
Time to cut 2.5 cm (s)	23	17

The standby power for the NCMC apparatus was about 46 W, largely due to the high-voltage charger. This power draw could conceivably be reduced to nearly zero as a purpose-built capacitor charger would eliminate the need to have the capacitors charged in standby. The NCMC system required 266 pulses to cut 2.5 cm, with each pulse requiring about 25 J. Not including any charging losses, the NCMC system would use about 6.7 kJ of energy to cut the distance. To match the jigsaw's speed, the NCMC system would need to operate at about 16 kHz. The maximum theoretical operating frequency for 25 J pulses would be about 12 kHz with the current hardware due to charging power limitations.

As one would expect, commercial equipment outperforms the second-generation NCMC system in terms of speed and efficiency. As described in the previous section, there are many ways that the efficiency of future NCMC system could be enhanced; it is conceivable that a future NCMC system could outperform the saws tested in terms of cut speed and operating power. However, NCMC has several unique characteristics (non-contact, very fine kerf) that may make it better suited for specialty applications rather than as a general-purpose cutting tool.

5.5.2 NCMC COMPARED TO LASER, WATERJET, AND EDM CUTTING

The NCMC concept is early in its development, and it is difficult to see where, if at all, it might fit in with large-scale commercial metal-cutting equipment. NCMC's advantage in this area is probably its low consumables, which might translate into very high reliability and low downtime.

A prudent development path would be to find an application where NCMC was particularly well suited and develop a solution toward that goal. Comparing laser, waterjet, and EDM technologies without a particular application in mind is difficult and not very informative. This is because the equipment can operate in many different modes that are often mutually exclusive. For example, the maximum cutting speed and the best dimensional accuracy cannot be realized at the same time. This section will detail a number of NCMC's unique characteristics and discuss how they could help it find a place among the current cutting technologies.

No contact. NCMC does not need to touch the workpiece. The coil does need to be fairly close to the workpiece, ideally less than 1 mm, but further distances are theoretically possible. NCMC could cut metals housed in non-conducting materials such as plastic. In the PCB experiments, for example, the coil was pressed to the G-10 substrate rather than to the copper layer. The copper layer was cut through the plastic without damaging the plastic. Laser and arguably waterjet cutters do not contact the workpiece, but neither of these technologies could have cut through plastic without causing damage.

Low consumables. NCMC does not require the cutting apparatus to experience high temperatures or forces, so there is no need for any consumable components. This is possible because NCMC uses the material being cut to enhance current density to a level that causes damage rather than doing the enhancement within the apparatus itself. The fact that it does not have any consumable parts is a major difference between NCMC and laser, waterjet, and EDM technology. The consumable for EDM technology is brass wire, which must be discarded after a single use. Waterjet technology uses an abrasive cutting compound and high-pressure nozzles that must be replaced. Lasers have optics such as mirrors and lenses that have limited lifetimes.

For large-scale commercial operations, the return on investment will probably be the determining factor. A fully developed NCMC system may be able to provide very long operating life, which would minimize the need for recalibration and other maintenance. However, the technology is not far enough along to be able to make substantiated claims about might be possible.

Fine kerf. NCMC cuts generally have kerfs of about 0.07–0.1 mm, and kerfs as fine as 0.013 mm have been produced. This is much thinner than EDM or waterjet kerfs as well as most laser cutter kerfs.

Melt-based cutting. NCMC's melt-based cutting process could be used to cut materials like molybdenum or possibly tool steel that are difficult to cut with conventional machining approaches. 0.5 mm thick molybdenum was successfully cut with NCMC. While waterjet or laser technology may be able to cut molybdenum, one machine shop refused to attempt it for fear of damaging equipment. Steel shim stock was successfully cut with NCMC, but thicker steels are not able to be cut with the second-generation NCMC system.

Requires a starter cut. A starter cut is critical for NCMC operation since it is what enhances the local current density to levels high enough to cut. Other cutting technologies have some starting feature requirements, but they are not as difficult to make as the NCMC starter cut. For example, EDM cutting requires a starter hole to be drilled by some other means and, while some waterjet cutters are able to pierce, in practice starter holes are often used.

Requires that the coil's footprint be unobstructed. The utility of NCMC's ability to make fine-kerf cuts is considerably decreased by its requirement for a large amount of material around these cuts. The surrounding material is required so that a high current can be developed in the workpiece from a coil that is operating well below its thermal and pressure limits. A 2.54 cm coil was used for the experiments in this dissertation. Smaller coils are possible, but they will generate more heat per pulse and be harder to cool.

5.6 Reduction to Practice

This section outlines three major issues to be solved before NCMC could be a viable manufacturing process. This is the third of three primary objectives of this dissertation.

5.6.1 ELIMINATING BIFURCATIONS

This section outlines what is known about bifurcations and suggests how they may be eliminated. Bifurcations were not directly studied in this research, but they were observed on many occasions. A bifurcation occurs when a single cut splits into two. Figure 5.16 shows the typical morphology of a cut that exhibits bifurcations.

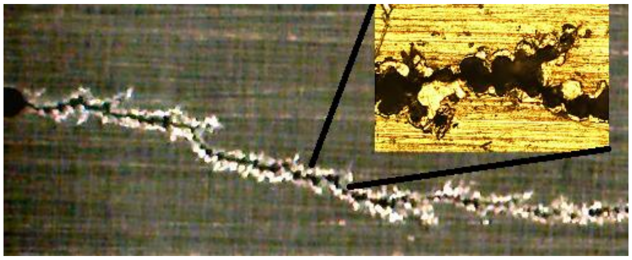

Figure 5.16. Magnetic saw sample with periodic short bifurcations. The inset picture was taken under 10× magnification.

When a cut bifurcates, the additional cut has little effect on the total induced current, but it has the effect of blunting the sharp bend in the current around the primary cut. The drive-coil current must be increased to compensate. Bifurcations also cause the direction of the cut to shift. If the secondary path of the bifurcation does not extend, then the cut proceeds at the original rate, but it has a wavy characteristic that is unacceptable for a commercial cutting technology, as seen in Figure 5.16. Table 4.2 shows that there is a band between the onset of cutting and bifurcation where controlled, reproducible cutting is possible. Bifurcations have the effect of limiting the high end of this operating band.

A working hypothesis for bifurcations is that there are several imperfections at the cut tip competing to be the point of onset. The usual case is that onset occurs first at some flaw (generally in the center of the starter feature, since the current density is highest there). As this cut extends it decreases current density in neighboring flaws, thereby preventing them from extending. Bifurcations occur when imperfections in a feature are far enough apart that the drive current can support the extension of two cuts. This will be referred to as the bifurcation competition theory. The competition theory suggests that bifurcations become more likely for larger starter features with rough surfaces and when higher excitations produce higher current densities at the cut tip.

In the PCB experiments, no bifurcations were observed on the initial cut from the PCB’s starter notch, even at double the excitation level that produced onset. However, when the starting feature was a blowhole from a previous pulse, bifurcations were observed in the usual manner, as shown in section 4.5.5. This can be explained by bifurcation competition theory, as the PCB starter features had a much smoother surface than the blowholes did. Visual inspection of the blowhole’s surface indicates that there are features on the surface with radii between 5 μm and 15 μm. These sub-features may allow for multiple hot spots to develop, as implicated in the competition theory.

In order to widen the operating band, future efforts should consider trying to reduce the size of the blowholes to the scale of surface roughness. If the kerf could be reduced to 10–30 μm, any sub-features would be so close together that multiple cutting onset points would be unlikely.

5.6.2 CONTROLLING EJECTA FOR CUT STRAIGHTNESS

This section describes what is known about the influence of solidified ejecta on subsequent cuts and the process by which material is removed.

There appears to be an inverse relationship between the straightness of a cut and the amount of solidified ejecta at the sides. That is, the straightest cuts are those with the least amount of ejecta. A few simulations and experiments have provided insight into how the presence of asymmetrical ejecta can affect subsequent cuts as well as insight into the process by which material is ejected.

Figure 5.17 shows a transient electromagnetic simulation of an approximation of the geometry of the solidified ejecta as well as an example of solidified ejecta that was observed in an experiment. The simulation results seen in Figure 5.17 show the square section (that is, the ejecta) causing an asymmetry in the current density at the cut tip: the peak current density is directed toward the ejecta. It is reasonable that a slight bias in current density can influence the local cut direction.

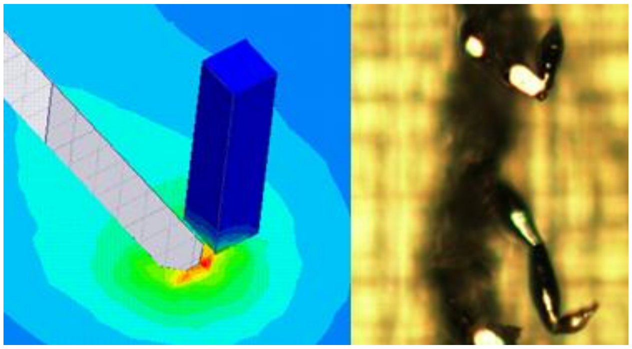

Figure 5.17. On the left is an electromagnetic simulation in which a square section of conductor was extruded to represent residual ejecta. The kerf of the cut is 0.076 mm. The photograph on the right shows solidified ejecta from a series of cuts. The ejecta was probably bent in handling before being photographed.

The right side of Figure 5.17 is a close-up from the 1200 V experiment shown in Figure 4.12. In that experiment, the double-sided tape interfered with the ejecta on the far side of the cut, causing the cut to follow the edge of the tape rather than continuing toward the edge of the sample. This supports the idea that solidified ejecta biases the direction of subsequent cuts toward the side of the ejecta.

The mechanism for ejection appears to be that the molten metal is pushed by the Lorentz force and escapes through any available opening in the solid material. The material shown being ejected in Figure 2.1 appears to be traveling between 200 m/s and 300 m/s. This is about an order of magnitude faster than the magnetic saw cut speed. Calculations from FEA simulation results suggest a pressure of about 120 MPa acting on the cut tip.

A small experiment provided insight into the process by which ejecta is formed. In this experiment, a coil was built that had epoxy filling the window (the center part without conductors). The epoxy in the window of the coil extended slightly beyond the rest of the coil’s surface. When a sample was clamped to this coil, the epoxy was forced into the surface of the aluminum sample, which effectively sealed off one of the paths for ejecta to escape, as illustrated in Figure 5.18.

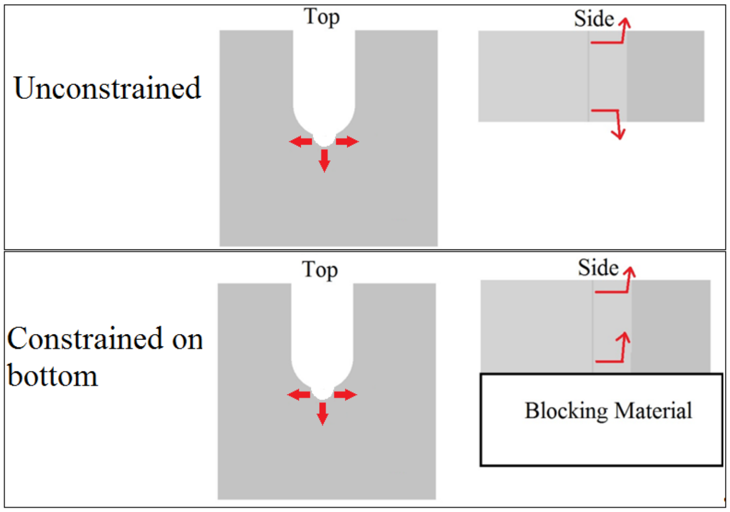

Figure 5.18. An illustration showing the path of ejected material in the unconstrained case and with a blocking material on the bottom.

Several 1.5 mm 6061 T6 samples were tested under a variety of conditions. All had an increased amount of solidified ejecta on the open side but little to no ejecta on the occluded side, as shown in Figure 5.19.

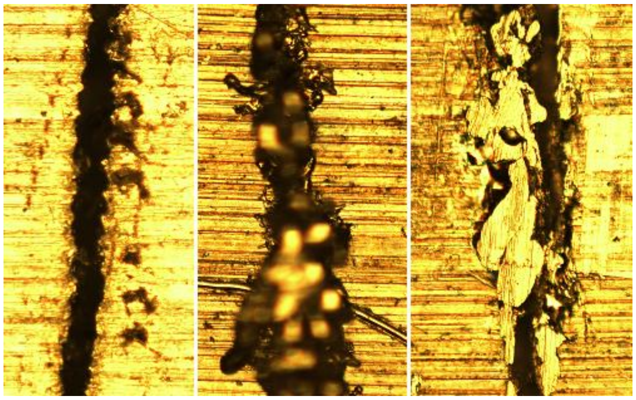

Figure 5.19. Each of the three photographs was taken from the same sample in approximately the same displacement from the edge, at 10× magnification. The leftmost image was the side that was pressed against plastic so that ejecta could not escape. The center image is of the opposite side, where the ejecta was able to escape; the focal plane is on the sample's surface, which causes the ejecta to blur since it is above the surface. The rightmost image shows the same surface as the center one, but after the ejecta has been scraped away.

Note that the cut path appears to have less variation. In the rightmost image of Figure 5.19, one can see that even with the ejecta removed, the resulting cut is less straight than on the side that was constrained. This suggests that if the ejecta could be removed more completely the overall cut would be straighter. This effect is likely due to resolidified aluminum altering the current distribution near the cut tip.

One possible approach to reducing the effect of ejecta may be to constrain the ejecta on both the top and bottom surface. This results in much less material being removed and reduces the effective size of the kerf.

5.6.3 ENHANCING CUT STEERING

This section outlines the process for steering cuts and suggests some ways for future systems to be able to produce tighter turns than what is currently possible. This research has focused on cuts where the starter notch is positioned on the centerline of the coil.

However, it is possible to bias the peak current density to the right or left side of the cut by positioning the starter cut away from the center of the coil and thereby steer the cut. A simulation result that shows how cut-coil position can bias the current density is shown in Figure 5.20. The technique of steering a cut by changing the position of the drive coil was tested experimentally, and the results are shown in Figure 5.21.

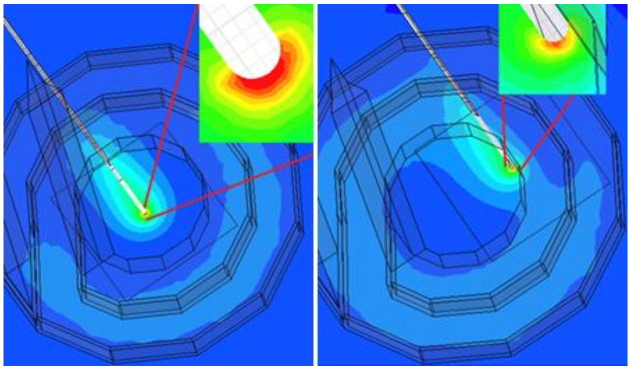

Figure 5.20. Current density induced in aluminum plate by the application of a pulsed magnetic field.

Note that the current density appears to be symmetrical across the centerline in the image on the left of Figure 5.20, where the cut is centered in the coil. When the cut is positioned such that it is nearly under the edge of the coil, as shown on the right, the current density is biased to the inside direction of the coil, thereby steering the cut toward the interior of the coil. The scale is the same for both cases and the peak current density shown is 5.8×10^{10} A/m^2. Figure 5.21 shows experimental results of using the coil-cut position to steer subsequent cuts.

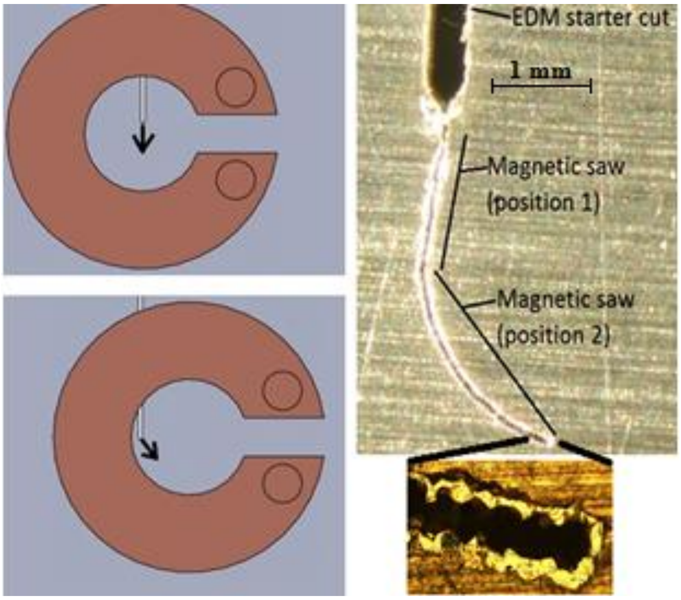

Figure 5.21. On the left, the two coil positions are illustrated. On the right, the resulting magnetic saw cut is shown.

Figure 5.21 shows that positioning the cut toward the edge of the coil can cause subsequent cuts to change direction. This process can be used to cut out arbitrary shapes from metal sheet, as long as the cuts are not so close to one another that multiple cuts are under the footprint of the coil.

NCMC is a novel approach to making fine cuts in metal plate. Its principal advantage is that there is no physical contact between a cutting tool and the workpiece. This is also the case in techniques such as laser or waterjet cutting; however, NCMC has the unusual property of using the material being cut as a focusing element. Ordinarily, a cutting device interacts with the workpiece on approximately the volume of material that will be removed. For example, a laser cutter is focused externally on the section of material that will be removed—or, on a mill, the bit and the workpiece meet where material will be removed. In the case of waterjet cutting the focusing element is a high-pressure nozzle. In NCMC, however, a relatively diffuse and weak magnetic field is applied over a large area, and a feature in the workpiece itself enhances the effect of this field. Because of this reliance on the workpiece, conditions of the workpiece within approximately the diameter of the coil can affect the cut direction and magnitude. Due to this dependence on the workpiece, it is probably desirable to have smaller coils, despite the fact that smaller coils are more subject to heating issues. The use of smaller coils, flux concentrators, or non-circular coils may help with steering and mitigate the workpiece-dependence issue.

5.7 Discussion of NCMC's Viability as a Commercial Process

The NCMC approach has produced some promising results that show the controlled extension and steering of a cut; however, significant challenges remain before NCMC can become a viable manufacturing process. If significant progress is made on the three issues described in section 5.6, NCMC could be a viable process for cutting metals.

The development of NCMC would be greatly enhanced if a specialty application were found where the NCMC process has a particular advantage over alternative technologies and where its limitations pose no hindrance. As described in section 5.5.2, NCMC's main advantages are that it does not require physical contact with the workpiece and that there are no consumable parts because no high forces or temperatures exist in the apparatus. Also detailed in section 5.5.2, NCMC's primary disadvantage is that since the workpiece is used as a kind of lens for enhancing current density, the process requires that the workpiece have a starter notch and be unobstructed for an area at least as large as the coil.

CHAPTER 6. SUMMARY AND CONCLUSIONS

6.1 New Approach and Apparatus for Making Fine Cuts in Metal Plate

This dissertation is a systematic investigation of a novel metal-cutting technology that uses pulsed magnetic fields to advance and steer fine cuts in metal plate and foil. Over the course of three years, two apparatuses were designed, constructed, and used to conduct several experimental series.

Previously, several researchers had observed fine cuts develop when pulsed currents were forced to make sharp bends; this phenomenon is called the magnetic saw effect. The research effort culminating with this dissertation is the first to use induced currents to produce and steer magnetic saw cuts for use as a potential manufacturing process. This process is called non-contact magnetic cutting (NCMC). Though early in its development, this technology may one day be used in commercial metal-cutting hardware, similar to laser or waterjet cutters.

The first NCMC system proved the feasibility of this approach to cutting metal plate. This system was used to conduct early experiments to evaluate the conditions that produced good cuts.

A second NCMC system was constructed based on results from the early experiments. This system was over twentyfold more efficient than the first and better suited for carrying out highly controlled experiments. This system could be quickly configured for three different pulse shapes and allowed researchers to view the cutting operation in real time, using a microscope.

6.2 Simulations and Experiments Cutting Metal Plate and Foil

One major simulation series and four main experimental series were performed. The simulation series involved running 63 simulations to map out how the material thickness, pulse duration, and location of the cut along the coil's centerline affect conditions at the cut tip. This set of simulations did not pertain to any particular experiment, though it was used to interpret the results from subsequent experiments.

The first series of experiments provided a detailed look at the onset of cutting and steady-state cutting for a single set of operating conditions, using 0.79 mm thick 6061 T6 aluminum. Many parameters of interest could not be measured directly in these experiments, so simulations with measured experimental results as inputs were used to calculate these quantities.

A second set of experiments took a higher-level view to investigate how cutting was affected by different material thicknesses and pulse durations. These experiments were used to identify a band between no cutting and bifurcating cuts, where acceptable cuts were produced in 6061 T6 aluminum.

A third set of experiments provided higher-fidelity results in 6061 T6 aluminum and extended the dataset to Al-25 copper. These experiments were used to provide convincing support to the idea that the dominant mechanism for the magnetic saw effect in this regime is melting rather than fracture.

The final set of experiments used PCB technology to make samples with starter notches of three different kerf thicknesses. The high accuracy of PCB technology allowed for the controlled study of the effect of fine feature sizes on cutting. The results of these experiments showed that the energy required for the onset of cutting scaled proportionally to the starter feature size. This suggests that future work in this area should try to find ways to reduce the cut size further.

6.3 Model for the Onset of Cutting

The results of the experiments were used to formulate a model for understanding the onset of cutting. Two primary mechanisms for cutting had been proposed in previous research: melting and fracture. The most developed work used a critical current density to determine the onset of cutting. While the critical current density showed good agreement for some waveforms, it did not agree with the much shorter pulse-width excitations used in this research.

An onset model was formulated that used both energy and power criteria to predict the onset of cutting. This two-part model predicts onset for both the short-duration pulses used in these experiments and the longer-duration pulses that were used in some of the earlier work. The two-part model suggests that there are two regimes of cutting that depend on the duration of the excitation: an energy regime and a power regime. Short-duration pulses can be thought of as operating in the energy regime. In the energy regime, Joule heating occurs significantly more rapidly than heat can be conducted away from the hot spot; this rapid heating makes the total energy delivered to the hot spot the primary criterion for cutting. Long-duration pulses can be understood as operating in the power regime. For these longer-duration pulses, the rate of Joule heating is relatively low for much of the pulse, which makes thermal conduction more significant. For these slow pulses, the power criterion is more important than the energy criterion. The two-part onset model provides future researchers with a useful framework to understand the magnetic saw effect.

6.4 Path Forward

This investigation shows the plausibility of using pulsed magnetic fields to direct and steer fine cuts in metal plate and foil. It also found several areas that warrant further study, from the basic physics at the cut tip to the design and integration of compact pulsed-power supplies. The use of induced currents to advance and direct fine cuts is a new area of research, and there are many unexplored aspects.

This research identifies three primary issues that need significant progress before NCMC can become a viable manufacturing process. The first is the elimination of bifurcations. This research did not study bifurcations directly, but it proposes a theory for the cause of bifurcations and provides supporting evidence from the experiments and simulations. This work could serve as the starting point for future experiments that directly investigate the nature of bifurcations and show how they can be eliminated.

The second major issue is the control of ejecta. Solidified ejecta has been shown to affect cut direction, which limits the ability to control the cut. An investigation into the process by which material is removed might be able to find ways to reduce or eliminate this problem. High-speed video microcroscopy equipment would be especially useful for this study.

The third major issue is enhancing the ability to steer the cuts. This study focused on straight cutting, and little work was done on cut steering beyond showing that it could be done. The size of the coil limits the ability to make sharp turns, somewhat analogous to using a bandsaw with a thick blade. Smaller coils could be used, but they will have higher losses and will be more challenging to cool. Removable flux-compressing inserts could also be used, in theory. A study focused on cut steering could investigate the process and try these and other concepts to improve the ability to change the direction of the cuts.

There appear to be advantages to using even shorter pulse-width excitations for manufacturing applications. Such excitations might be able to reduce the size of the cuts, thereby improving the efficiency of the operation and reducing the requirements for the power supply.

Relatively few researchers have studied the magnetic saw effect, although it has been observed since the 1950s and frequently appears in pulsed-power systems. This dissertation provides a new way of understanding the magnetic saw effect, at least in the regime studied.

APPENDICES

APPENDIX A. DERIVATION OF PROGRESSIVE MELTING MODEL

The derivation below expands on the progressive melting model described in Figure 2.4. The objective is to arrive at a simple analytical expression that captures the moving melt front that appears to be the dominant mechanism for the cuts shown in Figure 2.1 and other NCMC cases described in this paper. Though simple, this analytical expression appears to describe the melt speed observed in the images of Figure 2.1. Figure A.1 illustrates the progressive melting model, and Figure A.2 shows the quantities used to derive an analytical expression.

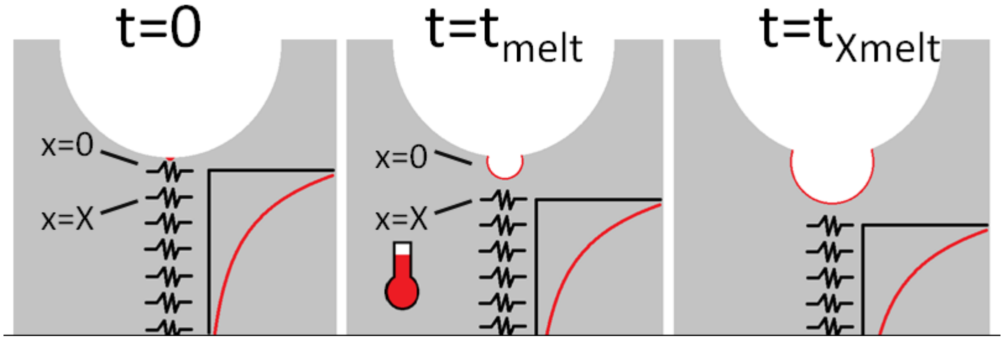

Figure A.1. The steps used to formulate the progressive melt model.

$$\rho_e = resistivity(\Omega * m) \qquad E_{melt} = melt\,energy(J/m^2)$$

Current density approximated by : $j(x) = j_0 e^{-\alpha x}$

Figure A.2. The quantities used to formulate an analytical expression for the progressive melting model.

A.1 Finding the Time to Melt $x = 0$

Let us refer to the time to melt the first element ($x = 0$) as t_{melt}. The first element $x = 0$ will melt when energy E_{melt} has been added through resistive heating. Energy E_{melt} has been experimentally determined for some metals [18], and one can infer an approximate value for 6061 aluminum. We will assume that resistivity remains at a constant value for this derivation. The equation for the rate that energy from resistive heating is added is

$$\frac{d}{dt}Energy = \rho_e * j(x)^2 .$$

The expression for the energy added over a period of time $t_2 - t_1$ is

$$Energy = \int_{t_1}^{t_2} \rho_e * j(x)^2 dt .$$

At $x = 0$, the current density is j_0, and we are interested in the time from $t = 0$ to $t = t_{\text{melt}}$, so the expression for the energy needed to melt $x = 0$ becomes

$$E_{melt} = \int_0^{t_{melt}} \rho_e * j_0^2 dt .$$

After performing the integration, this equation becomes

$$E_{melt} = \rho_e * j_0^2 * t_{melt}.$$

Solving for t_{melt}:

$$\boxed{t_{melt} = \frac{E_{melt}}{j_0^2 * \rho_e}}.$$

This is the time to melt the material at $x = 0$. Once the material at $x = 0$ has melted, the current is assumed to keep the same shape but shifts over so that the peak current j_0 is now flowing through $x = X$, which is a point infinitesimally close to $x = 0$.

A.2 Finding the Melt Speed

To find the melt speed, we will write an equation for the energy that needs to be added to bring the point $x = X$ up to melt. This expression will be rewritten in terms of X and then differentiated with respect to t to arrive at an analytical expression for melt velocity.

Let's define $E(x, t_{\text{melt}})$ to be the energy at point x at time t_{melt}. Now, we can write an energy balance equation to determine the amount of energy needed to melt X, given that X has already had $E(X, t_{\text{melt}})$ added since $t = 0$. We will call this additional energy $E\Delta$:

$$\boxed{E_{melt} = E_{X,t_{melt}} + E_{\Delta}}.$$

Expressions for $E\Delta$ and $E(X, t_{\text{melt}})$ will be developed below and then substituted back into this energy balance equation.

Now we will find an expression for E∆.

The rate at which energy is added to the point $x = X$ is the same as the point $x = 0$, before it melted:

$$\frac{d}{dt} * Energy = \rho_e * j_0^2.$$

Integrating this equation from the time t_{melt} to a later time, tX_{melt}, when $x = X$ melts, give us an expression for E∆:

$$E_\Delta = \int_{t_{melt}}^{t_{Xmelt}} \rho_e * j_0^2 dt,$$

which becomes

$$\boxed{E_\Delta = \rho_e * j_0^2 * t_{Xmelt}}.$$

Now we will find an expression for E(X, t_{melt}).

At time $t = t_{\text{melt}}$, the energy at point $x = X$ can be found with the same expression used with $x = 0$:

$$Energy = \int_{t_1}^{t_2} \rho_e * j(x)^2 dt.$$

But this time, let $t_1 = 0$, $t_2 = t_{\text{melt}}$, and $x = X$:

$$E_{X,t_{melt}} = \int_0^{t_{melt}} \rho_e * j_0^2 * e^{-2\alpha X} dt,$$

which becomes

$$\boxed{E_{X,t_{melt}} = \rho_e * j_0^2 * t_{melt} * e^{-2\alpha X}},$$

or, in terms of E_{melt}:

$$\boxed{E_{X,t_{melt}} = E_{melt} * e^{-2\alpha X}}.$$

A.3 Velocity Expression

Now that we have developed expressions for $E\Delta$ and $E(X, t_{\text{melt}})$, we can substitute them back into the energy balance equation, which becomes

$$E_{melt} = E_{melt} * e^{-2\alpha X} + \rho_e * j_0^2 * t_{Xmelt}$$

Aiming to isolate *X*, this can be rewritten as

$$e^{-2\alpha X} = \frac{E_{melt} - \rho_e * j_0^2 * t_{Xmelt}}{E_{melt}},$$

and then taking the natural log of both sides results in

$$-2\alpha X = ln\left(\frac{E_{melt} - \rho_e * j_0^2 * t_{Xmelt}}{E_{melt}}\right).$$

Now we can isolate X:

$$X = \frac{-1}{2\alpha} * ln\left(\frac{E_{melt} - \rho_e * j_0^2 * t_{Xmelt}}{E_{melt}}\right),$$

and then differentiate the equation with respect to *t* to get

$$\frac{\mathrm{d}}{\mathrm{d}t}X = \frac{\mathrm{d}}{\mathrm{d}t}\left[\frac{-1}{2\alpha} \ * \ ln\left(\frac{E_{melt} - \rho_e * j_0^2 * t_{Xmelt}}{E_{melt}}\right)\right].$$

One can apply the chain rule to a natural logarithm as follows:

$$\boxed{\frac{d}{dx}(\ln g(x)) = \frac{g'(x)}{g(x)}.}$$ [22].

Using this rule, we see that

$$\frac{\mathrm{d}X}{\mathrm{d}t} = \frac{\rho_e * j_0^2}{2\alpha * E_{melt} - 2\alpha * \rho_e * j_0^2 * t_{Xmelt}}.$$

We will let $t_{X\mathrm{melt}}$ approach zero, as we have assumed that *X* is infinitesimally close to zero. The final equation for melt velocity, in m/s, is

$$\boxed{Melt\ velocity = \frac{\mathrm{d}X}{\mathrm{d}t} = \frac{\rho_e * j_0^2}{2\alpha * E_{melt}}}.$$

The following values were selected to approximate the experiment seen in Figure 2.1:

α: 1500 (1/m)

j_0: 4.5x1010 (A/m^2)

ρ_e: 5 × 10^{-8} (Ω*m)

E_{melt}: 1.7x109 (J/m^3)

Using the melt velocity equation derived above, the predicted velocity is about 20 m/s.

APPENDIX B. DERIVATION OF THE RESISTIVE-ONLY MODEL OF CURRENT DISTRIBUTION

The objective is to derive an expression for the current density at any radius r, for $r_1 < r < r_2$, where r_1 and r_2 are the inner and outer radii. Assume there is a two-dimensional disk with inner radius r_1 and outer radius r_2, as in Figure B.1. There is a constant current flowing through this disk whereby there is a current density of J_{peak} along the innermost surface.

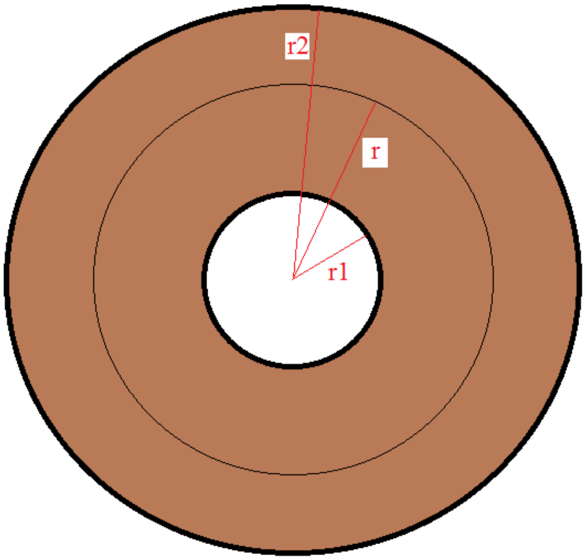

Figure B.1. Two-dimensional disk with inner radius r_1 and outer radius r_2.

By symmetry, the current flows through circular paths about the origin. Since the paths are circular, there is no current in the radial direction; hence, the voltage potential between any two points along a line extending from the origin and between r_1 and r_2 is zero. Since the voltage potential between any two circular paths is zero, the voltage drop around any two paths must be equal. The resistance per unit cross section of the innermost path and the path at any radius r is shown below:

$$R_{r1} = \rho * 2 * \pi * r1$$

$$R_r = \rho * 2 * \pi * r.$$

And setting the voltage drops equal to each other results in

$$J_{\text{peak}} * 2 * \pi * r1 = J(r) * 2 * \pi * r.$$

Rearranging this equation produces

$$J(r) = \frac{J_{\text{peak}} * r1}{r}.$$

Figure B.2 shows this result graphically.

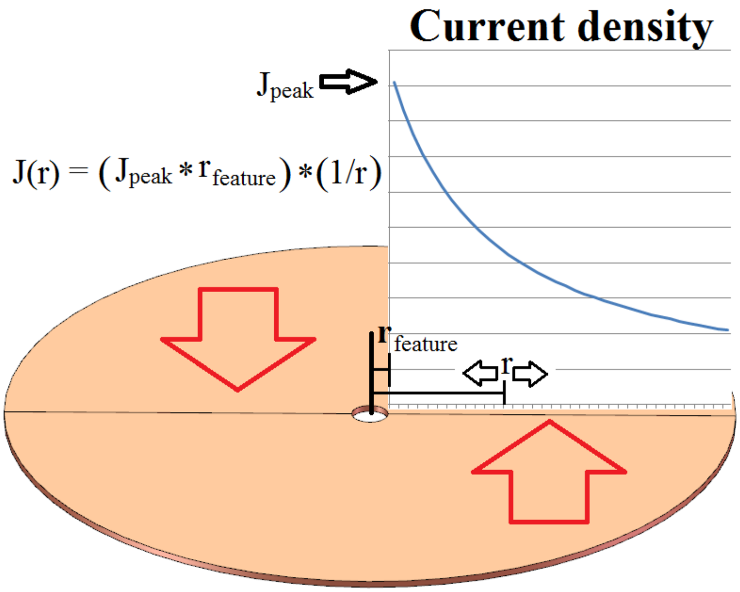

Figure B.2. Graphic representation of current density.

It should be noted that in the case of NCMC, the current's path around the feature is not circular as in this model, but rather only makes approximately half a circle. Because of this, the resistive-only model of current distribution is most accurate along the centerline extending from the feature's radius.

APPENDIX C. ENERGY AND CRITICAL CURRENT DENSITIES RESULTS

Table C.1. The energy and critical current densities calculated for the 6061 T6 aluminum plate experiments.

Thickness	**0.41 mm**	**0.41 mm**	**0.41 mm**	**0.79 mm**	**0.79 mm**	**0.79 mm**	**1.55 mm**	**1.55 mm**	**1.55 mm**
Pulse width (μs)	**17 μs**	**25 μs**	**30 μs**	**17 μs**	**25 μs**	**30 μs**	**17 μs**	**25 μs**	**30 μs**
Energy to melt (J/mm^3)	2.94	3.42	3.445	3.16	3.53	3.56	N/A	3.035	3.82
Critical current density (1 × 10^{10} A/m^2)	4.86	4.79	4.54	5.15	4.93	4.71	N/A	4.93	4.71

Table C.2. The energy and critical current densities calculated for the Al-25 copper plate experiments.

Thickness	**0.36 mm**	**0.36 mm**	**0.36 mm**	**0.83 mm**	**0.83 mm**	**0.83 mm**
Pulse width (μs)	**17 μs**	**25 μs**	**30 μs**	**17 μs**	**25 μs**	**30 μs**
Energy to melt (J/mm^3)	4.95	5.04	4.64	N/A	7.37	7.01
Critical current density (1 × 10^{10} A/m^2)	9.71	8.93	8.09	N/A	12.1	11.0

Table C.3. The energy and critical current densities calculated for the PCB experiments.

Thickness	**0.036 mm**	**0.036 mm**	**0.036 mm**
Pulse width (μs)	**17 μs**	**17 μs**	**17 μs**
Kerf (mm)	**0.20**	**0.28**	**0.44**
Energy to melt (J/mm^3)	6.76	6.59	6.28
Critical current density (1 × 10^{10} A/m^2)	10.1	8.80	7.24

APPENDIX D. CUTTING FROM THE PERSPECTIVE OF THE COIL

Because NCMC uses induction to develop current in the sample rather than direct conduction, the current in the sample is influenced by factors beyond excitation. Section 4.1 provides a detailed description of a systematic series of simulations that examine this effect. This section summarizes the primary points of that series and provides additional insight.

D.1 Transformer Model

The change in magnetic field produced by the coil results in a proportional voltage in the sample. This voltage causes current to flow along well-defined paths (wires) in typical applications. However, in the case of NCMC, the current in the workpiece is not constrained and displays more complex behavior.

The general shape of the heating at the cut tip can be approximated as a transformer with a diffusion network in the secondary. More sophisticated formulations are possible; however, this model shows the main effect. Figure D.1 shows a simple circuit schematic of this approximation, current outputs, and this model's calculated heating of a resistor compared to heating in the non-coil-side 10 μm cube calculated by Maxwell 3D. Note that experimental data is being used to drive the transformer rather than modeling the power supply.

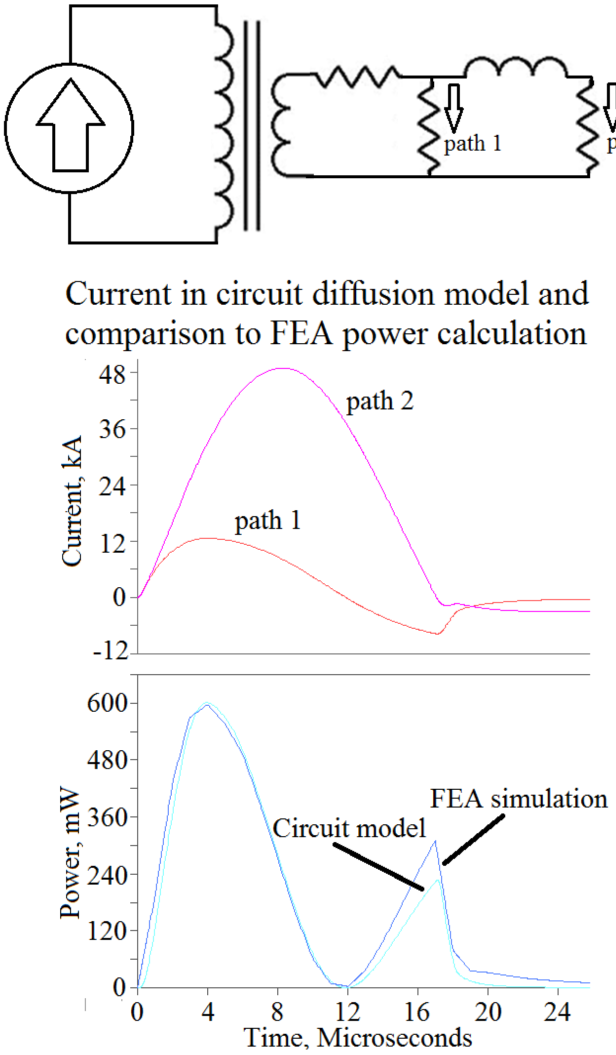

Figure D.1. A circuit model for induced heating at the cut tip is shown above the current outputs and a comparison of the scaled power dissipated in the path 1 resistor compared to the heating calculated in a 10 µm cube by the FEA simulation. Only the primary coupling is shown, but the path 2 inductor is weakly coupled to both the path 1 inductor and the primary. The case shown is the 0.36 mm thick Al-25 copper with a 17 µs pulse width and 1450 V charge voltage, which are the threshold conditions for cutting.

The operation of this transformer with diffusion model is as follows: as the current in the primary increases, current in the secondary's circuit initially flows through the higher-resistance, lower-inductance path, but as time progresses, the current shifts increasingly to the higher-inductance, lower-resistance path. This is physically equivalent to the current's being pulled tightly against the intrusion of the starter cut but gradually diffusing out into the bulk of the workpiece. As time continues, the current in the low-inductance path reverses direction; this diffusion and current reversal is seen in the FEA simulations.

With no diffusion into the bulk workpiece material, the current at the cut tip would be proportional to the excitation current. For very thin workpieces such as the copper foil on PCBs, the workpiece has a much higher resistance resulting in a more pronounced current reversal in path 1. Figure D.2 compares the heating at the cut tip for similar conditions on Al-25 copper plate and PCB experiments.

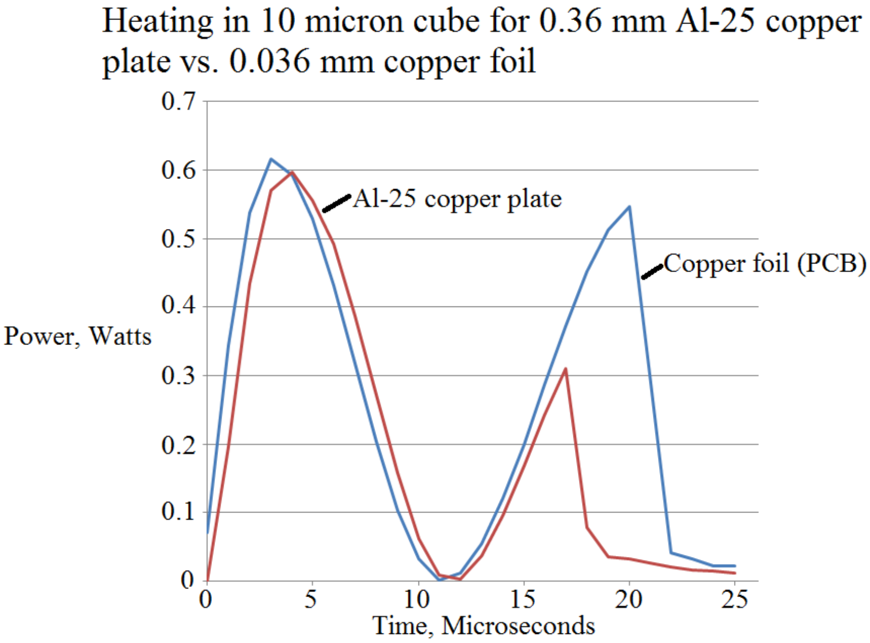

Figure D.2. The heating in the 10 µm cubes is compared for the onset condition of 0.36 mm thick Al-25 copper plate and 0.036 mm thick copper foil. The capacitor bank was configured the same in both cases, though the resulting current pulse was longer in the PCB case due to an overall increase in inductance for the thinner workpiece.

D.2 Excitation Frequency’s Effect on Cutting

For efficient operation, the excitation frequency should generally be high enough to make the skin depth less than the workpiece thickness. Comparing the results of the experiments provides some support for this concept, but the effect is not large. Table D.1 shows the stored energy for each of the experiments described in section 4.4.

Table D.1. The energy stored in the capacitors for the onset-of-cutting condition of the experimental results described in Section 4.4.

	6061 T6 Aluminum			**Al-25 Copper**	
	0.41 mm	0.79 mm	1.55 mm	0.36 mm	0.83 mm
Stored Energy (J) 17 µs pulse	16.5	36.0	N/A	31.5	N/A
Stored Energy (J) 25 µs pulse	19.2	39.7	74.4	31.5	138
Stored Energy (J) 30 µs pulse	20.5	40.6	94.6	30.6	132

Table D.1 shows a trend of onset requiring less energy for the shorter pulses for the aluminum results. However, the copper results show essentially no change or a slight advantage to the longer pulses. The system resistance is higher for the shorter pulses because there are fewer capacitors in parallel, so the power supply is less efficient than when it is configured for the longer pulses.

In the PCB experiments, the skin depth of the current pulse was about 0.45 mm when the thickness of the copper foil was about 0.036 mm, but in the copper plate experiments, the Al-25 was ten times thicker—0.36 mm. The efficiency of cutting the plate for the T40 cases was on average about 20% greater than for the foil case. It may be that the higher resistance of copper foil results in less diffusion away from the cut tip, which partially offsets the decrease in efficiency due to the magnetic field's completely diffusing through the workpiece.

The first- and second-generation systems differed in excitation frequency by nearly an order of magnitude. However, other differences between the two systems make direct comparisons difficult. The first-generation system required about 735 J of stored energy to advance a cut in 0.79 mm thick 6061 T6 aluminum; the second-generation system would only need about 43 J for the same cut. However, most of the increased efficiency is due to lower transmission losses because the second generation used a fourteen-turn coil instead of the two-turn coil used by the first-generation system.

D.3 Influence of the Workpiece on Transformer Operation

In this dissertation, the second-generation system is considered to produce 17 µs, 25 µs, and 30 µs pulse widths. However, these are only nominal values; the workpiece affects the actual pulse width. This is because the more conductive the workpiece is, the lower the system inductance will be—the current developed in the workpiece cancels the coil's flux. Figure D.3 compares the excitation currents for the threshold cases using a PCB workpiece, a 0.41 mm thick aluminum workpiece, and a 0.83 mm thick Al-25 copper workpiece.

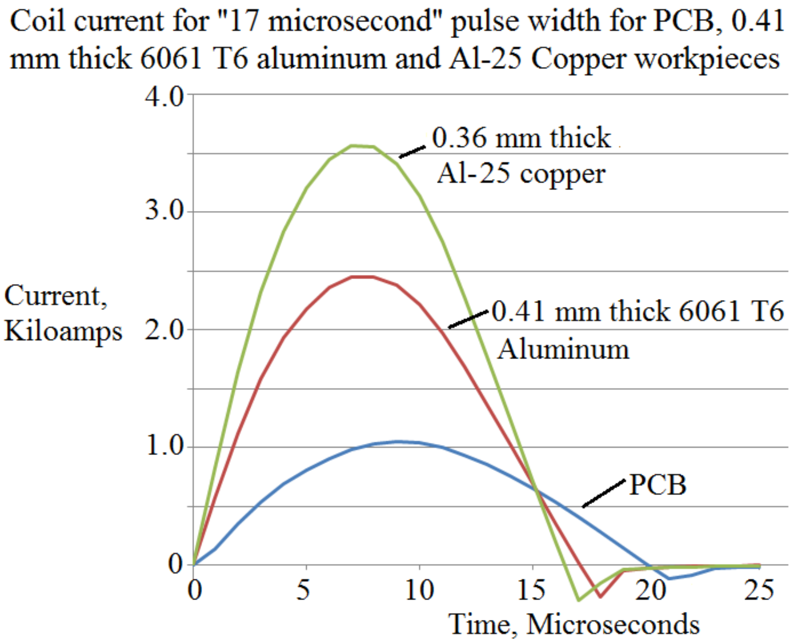

Figure D.3. The measured coil current when the power supply was configured for a “17 µs” pulse for 0.036 mm thick PCB, 0.41 mm thick 6061 T6 aluminum, and 0.36 Al-25 copper workpieces.

The 0.36 copper alloy workpiece has the shortest pulse width because of its low resistance. The PCB has higher-conductivity copper, but it is thin enough for the magnetic field to diffuse through and its total loop resistance is much higher than for either of the other two samples compared in Figure D.3.

APPENDIX E. ENERGY-EFFICIENCY RESULTS

Table E.1. The energy efficiency for the 0.41 mm and 0.79 mm thick 6061 T6 aluminum samples. The efficiency is the energy required to melt the material removed divided by the energy stored in the capacitors. The 1.55 mm thick results are omitted because no significant removal of material was observed in those cases.

Thickness	0.41 mm	0.41 mm	0.41 mm	0.79 mm	0.79 mm	0.79 mm
Pulse width (μs)	**17 μs**	**25 μs**	**30 μs**	**17 μs**	**25 μs**	**30 μs**
T20 % efficiency	0.011	0.029	0.031	0.010	0.011	0.025
T40 % efficiency	0.045	0.078	0.061	N/A	0.047	0.038
T60 % efficiency	0.085	0.102	0.110	N/A	0.087	0.091

Table E.2. The energy efficiency for the 0.36 mm thick 6061 T6 aluminum samples. The efficiency is the energy required to melt the material removed divided by the energy stored in the capacitors. The 0.83 mm thick results are omitted because no significant removal of material was observed in those cases.

Thickness	0.36 mm	0.36 mm	0.36 mm
Pulse width (μs)	**17 μs**	**25 μs**	**30 μs**
T20 % efficiency	0.0028	0.003	0.0001
T40 % efficiency	N/A	0.051	0.013
T60 % efficiency	N/A	0.111	0.048

Table E.3. The energy efficiency for the PCB experiments. The efficiency is the energy required to melt the material removed divided by the energy stored in the capacitors.

Thickness	0.036 mm	0.036 mm	0.036 mm
Pulse width (μs)	**17 μs**	**17 μs**	**17 μs**
Kerf (mm)	**0.20**	**0.28**	**0.44**
T20 % efficiency	0.001	0.005	0.003
T30 % efficiency	0.031	0.025	0.010
T40 % efficiency	0.019	0.028	0.033
T50 % efficiency	0.030	0.054	0.071

NOTES

1. H. P. Furth, M. A. Levine, and R. W. Waniek, “Production and Use of High Transient Magnetic Fields. II.” *Rev. Sci. Instrum.*, vol. 28, no. 11, pp. 949–958, 1957.
2. P. Kumar, A. Mishra, T. Watt, I. Dutta, D. L. Bourell, and U. Sahaym, “Electromagnetic Jigsaw: Metal-Cutting by Combining Electromagnetic and Mechanical Forces,” *Procedia CIRP*, vol. 6, pp. 601–605, 2013.
3. Alex J. Sitzman, Francis Stefani, David L. Bourell, and Eliseo Treviño, “Use of the Magnetic Saw Effect for Manufacturing,” in press: *IEEE Trans. Plasma Sci*. 2014.
4. David H. Sharp, “An Overview of Rayleigh-Taylor Instability.” *Physica D: Nonlinear Phenomena* 12.1: 3–18, 1984.
5. A. Yeoh, G. Prabhu, and C. Persad, “Liquation Cracking and Its Effects in Aluminum Alloy Armatures,” *IEEE Trans. Magn.*, vol. 33, no. 1, pp. 419–425, January 1997.
6. T. Watt and F. Stefani, “Experimental and Computational Investigation of Root-Radius Melting in C-Shaped Solid Armatures,” *IEEE Trans. Magn.*, vol. 41, no. 1, pp. 442–447, January 2005.
7. T. J. Watt and M. D. Bryant, “Microstructures in the Throat Region of Recovered Aluminum-Alloy Armatures,” *IEEE Trans. Magn.*, vol. 43, no. 1, pp. 422–425, January 2007.
8. V. K. Sarin and J. Gurland, “Enhancement of Fracture Toughness using High Intensity Electric Currents,” U.S. Army Research Office Final Report, ARO 28821.1-MS, April 1992.
9. Y.-M. Fu, X.-Z. Bai, G.-Y. Qiao, Y.-D. Hu, J.-Y. Luan, “Technique for Producing Crack Arrest by Electromagnetic Heating,” *Materials Science and Technology*, vol. 17, pp. 1653–1656, 2001.
10. Y. Zhou, J. Guo, M. Gao, G. He, “Crack Healing in a Steel by using Electropulsing Technique,” *Materials Letters*, vol. 58, pp. 1732–1736, 2004.
11. T. J. C. Liu, “Thermo-electro-structural Coupled Analyses of Crack Arrest by Joule Heating,” *Theoretical and Applied Fracture Mechanics*, vol. 49, pp. 171–184, 2008.
12. R. Merrill and F. Stefani, “Electrodynamics of the Current Melt-Wave Erosion Boundary in a Conducting Half-Space,” *IEEE Trans. Magn.*, vol. 39, no. 1, pp. 66–71, January 2003.

13. F. P. Bowden, J. H. Brunton, J. E. Field, and A. D. Heyes, “Controlled Fracture of Brittle Solids and Interruption of Electrical Current,” *Nature*, vol. 216, pp. 38–42, October 1967.
14. S. Satapathy, F. Stefani, and A. Saenz, “Crack Tip Behavior Under Pulsed Electromagnetic Loading,” *IEEE Trans. Magn.*, vol. 41, no. 1, pp. 226–230, January 2005.
15. D. Melton, T. Watt, and M. Crawford, “A Study of Magnetic Sawing in an Aluminum Bar,” *IEEE Trans. Magn.*, vol. 43, no. 1, pp. 170–172, January 2007.
16. F. Gallo, S. Satapathy, and K. Ravi-Chandar, “Melting and Crack Growth in Electrical Conductors Subjected to Short-Duration Current Pulses,” *Int. J. Fract.*, vol. 167, pp. 183–193, 2011.
17. Ernesto Gutierrez-Miravete, “Heat Conduction in Cylindrical and Spherical Coordinates,” *Conduction Heat Transfer*, Nov. 2006. http://www.ewp.rpi.edu/hartford/~ernesto/S2006/CHT/Notes/ch03.pdf.
18. T. J. Tucker and R. P. Toth, “EBW1: A Computer Code for the Prediction of the Behavior of Electrical Circuits Containing Exploding Wire Elements,” Sandia National Laboratories. SAND-75-0041, 1975.
19. C. A. Griffis, C. I. Chang, and F. R. Stonesifer, “Mechanical Response of Tension Panels under Intense Rapid Heating,” *Theoretical and Applied Fracture Mechanics*, vol. 3, pp. 41–48, 1985.
20. A. Challita and G. A. Hanlin, “Strength of Aluminum under Pulsed Heating Conditions,” *IEEE Trans. Magn.*, vol. 31, no. 1, pp. 684–688, Jan. 1995.
21. R. W. Powell, Cho Yen Ho, and Peter Edward Liley, “Thermal Conductivity of Selected Materials,” No. NSRDS-NBS-8. National Standard Reference Data System, 1966.
22. J. Hass, “Differentiating the Natural Log.” Digital n.p., 26 May 1999. Web. 26 Nov. 2013, http://www.howtoace.com/HTACFiles/node33.html.

WORKS CITED

Bowden, F. P., J. H. Brunton, J. E. Field, and A. D. Heyes, “Controlled Fracture of Brittle Solids and Interruption of Electrical Current,” Nature, vol. 216, pp. 38–42, October 1967.

Challita, A., and G. A. Hanlin, “Strength of Aluminum under Pulsed Heating Conditions,” IEEE Trans. Magn., vol. 31, no. 1, pp. 684–688, Jan. 1995.

Fu, Y.-M., X.-Z. Bai, G.-Y. Qiao, Y.-D. Hu, J.-Y. Luan, “Technique for Producing Crack Arrest by Electromagnetic Heating,” Materials Science and Technology, vol. 17, pp. 1653–1656, 2001.

Furth, H. P., M. A. Levine, and R. W. Waniek, “Production and Use of High Transient Magnetic Fields. II.” Rev. Sci. Instrum., vol. 28, no. 11, pp. 949–958, 1957.

Gallo, F., S. Satapathy, and K. Ravi-Chandar, “Melting and Crack Growth in Electrical Conductors Subjected to Short-Duration Current Pulses,” Int. J. Fract., vol. 167, pp. 183–193, 2011.

Griffis, C. A., C. I. Chang, and F. R. Stonesifer, “Mechanical Response of Tension Panels under Intense Rapid Heating,” Theoretical and Applied Fracture Mechanics, vol. 3, pp. 41–48, 1985.

Gutierrez-Miravete, Ernesto, “Heat Conduction in Cylindrical and Spherical Coordinates,” *Conduction Heat Transfer,* Nov. 2006. http://www.ewp.rpi.edu/hartford/~ernesto/S2006/CHT/Notes/ch03.pdf.

Hass, J., “Differentiating the Natural Log.” n.p., 26 May 1999, http://www.howtoace.com/HTACFiles/node33.html.

Kumar, P., A. Mishra, T. Watt, I. Dutta, D. L. Bourell, and U. Sahaym, “Electromagnetic Jigsaw: Metal-Cutting by Combining Electromagnetic and Mechanical Forces,” Procedia CIRP, vol. 6, pp. 601–605, 2013.

Liu, T. J. C., “Thermo-electro-structural Coupled Analyses of Crack Arrest by Joule Heating,” Theoretical and Applied Fracture Mechanics, vol. 49, pp. 171–184, 2008.

Melton, D., T. Watt, and M. Crawford, “A Study of Magnetic Sawing in an Aluminum Bar,” IEEE Trans. Magn., vol. 43, no. 1, pp. 170–172, January 2007.

Merrill, R., and F. Stefani, “Electrodynamics of the Current Melt-Wave Erosion Boundary in a Conducting Half-Space,” IEEE Trans. Magn., vol. 39, no. 1, pp. 66–71, January 2003.

Powell, R. W., Cho Yen Ho, and Peter Edward Liley, “Thermal Conductivity of Selected Materials,” No. NSRDS-NBS-8. National Standard Reference Data System, 1966.

Sarin, V. K., and J. Gurland, “Enhancement of Fracture Toughness using High Intensity Electric Currents,” U.S. Army Research Office Final Report, ARO 28821.1-MS, April 1992.

Satapathy, S., F. Stefani, and A. Saenz, “Crack Tip Behavior under Pulsed Electromagnetic Loading,” IEEE Trans. Magn., vol. 41, no. 1, pp. 226–230, January 2005.

Sharp, David H., “An Overview of Rayleigh-Taylor Instability.” *Physica D: Nonlinear Phenomena* 12.1: 3–18, 1984.

Sitzman, Alex J., Francis Stefani, David L. Bourell, and Eliseo Treviño, “Use of the Magnetic Saw Effect for Manufacturing,” in press: IEEE Trans. Plasma Sci. 2014.

Tucker, T. J., and R. P. Toth, “EBW1: A Computer Code for the Prediction of the Behavior of Electrical Circuits Containing Exploding Wire Elements,” Sandia National Laboratories. SAND-75-0041, 1975.

Watt, T., and F. Stefani, “Experimental and Computational Investigation of Root-Radius Melting in C-Shaped Solid Armatures,” IEEE Trans. Magn., vol. 41, no. 1, pp. 442–447, January 2005.

Yeoh, A., G. Prabhu, and C. Persad, “Liquation Cracking and Its Effects in Aluminum Alloy Armatures,” IEEE Trans. Magn., vol. 33, no. 1, pp. 419–425, January 1997.

Zhou, Y., J. Guo, M. Gao, G. He, “Crack Healing in a Steel by using Electropulsing Technique,” Materials Letters, vol. 58, pp. 1732–1736, 2004.